The Aqueous Corrosion Response of Ti(C,N), TiC and WC Based Ceramic-Metal Composites

by

Zhila Memarrashidi

Submitted in partial fulfillment of the requirements
for the degree of Master of Applied Science

at

Dalhousie University
Halifax, Nova Scotia
May 2015

Table of Contents

List of Tables v
List of Figures vi
Abstract viii
List of Abbreviations and Symbols Used ix
Acknowledgments x
Chapter 1. Introduction 1
Chapter 2. Literature Review 6
2.1. Introduction to Corrosion Response of Cermets 6
2.2. Electrochemical Nature of Corrosion 9
2.2.1. Electrochemical Reactions 9
2.2.2. Polarization 12
2.2.3. Passivation 13
2.2.4. Electrochemical Thermodynamics and Electrode Potential 15
2.2.5. Electrochemical Kinetics of Corrosion 17
2.3. Forms of Corrosion 19
2.3.1. Localized Corrosion 19
2.3.2. Crevice Corrosion 20
2.3.3. Pitting Corrosion 21
2.3.4. High Temperature Corrosion 22
2.3.5. Erosion Corrosion 24
2.4. Common Techniques in Corrosion Measurement 26
2.4.1. Electrochemical Methods 29
2.4.2. Potentiodynamic Polarization 30
2.4.3. Potentiostatic Polarization 31
2.4.4. Cyclic Polarization 32
2.4.5. Polarization Resistance 35
2.4.6. Electrochemical Impedance Spectroscopy 36
2.4.7. Tafel Plots 38
2.4.8. Erosion Corrosion Test 40
2.4.9. Non Electrochemical Methods (Cumulative Mass Loss) 40

2.5. Analysing the Results 41
2.5.1. Microstructural Analyses 42
2.5.2. Chemical Analyses 43
2.6. Summary 45
Chapter 3. Manufacturing of TiC and Ti(C,N) Based Cermets 46
3.1. Materials 47
3.1.1. Metallic Phase (Ni_3Al) 47
3.1.2. Ceramic Phase (TiC and Ti(C,N)) 49
3.1.3. WC-Co 50
3.2. Methods 51
3.2.1. Sample Preparation and Basic Characterization 51
3.2.2. Microstructural and Chemical Analysis 53
3.2.3. Electrochemical Analysis 53
3.3. Results and Discussion 55
Chapter 4. The Effects of C:N Ratio on the Aqueous Corrosion Response of TiC and Ti(C,N) Cermets with an Ni_3Al-based Binder 61
Abstract 61
4.1. Introduction 62
4.2. Experimental Procedures 64
4.2.1. Raw Materials and Processing 64
4.2.2. Electrochemical Characterization 66
4.2.3. Post-Corrosion Evaluation 68
4.3. Results and Discussion 69
4.3.1. Cermet Characterization 69
4.3.2. Electrochemical Analysis 72
4.3.3. Post Corrosion Analysis 87
4.4. Conclusions 92
Chapter 5. The Effect of Binder Content on the Aqueous Corrosion Response of WC-Co Cermets 94
Abstract 94
5.1. Introduction 95

5.2. Materials and methods 97
5.3. Results and discussion 99
5.3.1. Cermet Characterization 99
5.3.2. Electrochemical Analysis 100
5.3.3. Post Corrosion Analysis 106
5.4. Conclusions 110
Chapter 6. Conclusions and Suggestions for Future Work 112
References 115

List of Tables

Table 1. Nominal composition of elements for Ni_3Al, IC50 and IC221 metallic binders. 49

Table 2. Average corrosion parameters for the single phase TiC and Ti(C,N) ceramics, and the Ni_3Al intermetallic binder. 74

Table 3. Calculated corrosion parameters related to ceramic and metallic galvanic couples. 76

Table 4. Mean corrosion parameters of the TiC and Ti(C,N)-Ni_3Al cermets. All experiments were performed in an aqueous electrolyte with 3.5 wt.% NaCl. 80

Table 5. Average corrosion parameters for WC-Co 30 vol.% Co binder. All experiments were performed in an aqueous electrolyte with 3.5 wt.% NaCl. 83

Table 6. ICP-OES analysis on post corrosion electrolyte solution for the TiC and Ti(C,N) cermets with 30 vol.% Ni_3Al. All experiments were performed in an aqueous electrolyte with 3.5 wt.% NaCl. 91

Table 7. ICP-OES analysis on the particulates filtered from the post-corrosion electrolyte for the TiC and Ti(C,N) cermets with 30 vol.% Ni_3Al. The particulate material was acid dissolved prior to analysis. All experiments were performed in an aqueous electrolyte with 3.5 wt.% NaCl. 91

Table 8. Measured pH values for the post-corrosion electrolyte solutions after potentiodynamic polarization testing of the single phase TiC and Ti(C,N) ceramics and the Ni_3Al intermetallic. 92

Table 9. Average corrosion parameters for the WC-Co cermets with 10 vol.% Co binder. 104

Table 10. Average corrosion parameters for the WC-Co cermets with 30 vol.% Co binder. 104

List of Figures

Figure 1. Passivity at potentials above polarization potential. 14

Figure 2. Cross-sections of WC–17Co after cyclic polarization to 2000 mV (white arrow: a likely electrolyte path, black arrows: crevice corrosion). 21

Figure 3. Cross-sections and formation of pits on surface of WC–Co after polarization at 500 mV. 22

Figure 4. Wear tested surface of (a) $TiC_{0.5}N_{0.5}$-20vol% SS316 and (b) $TiC_{0.5}N_{0.}$5-30vol% SS316. 24

Figure 5. Passivation slope on a typical potentiostatic polarization plot. 32

Figure 6. Representative cyclic polarization plot. 34

Figure 7. Electrochemical impedance spectrometer. 38

Figure 8. Theoretical Tafel plot and best fit straight lines in anodic and cathodic direction[56]. 39

Figure 9. SEM images for a WC-CrNi cermet, (a) after and (b) before anodic polarization at 50°C in artificial seawater. 43

Figure 10. ICP-OES analyses of the post-test potentiodynamic polarization solutions of TiC-316L cermets[74]. 44

Figure 11. The observed decrease in grain sizes in Ti(C,N)-IC50 and Ti(C,N)-IC221 cermets through the addition of N to the ceramic phase. 56

Figure 12. An SEM image of the core rim structure formed in the TiC-Ni_3Al (30 vol.%) cermets. 57

Figure 13. EDS analysis, presence of Zr and W, in composition of rim 57

Figure 14. SEM images of the sintered cermets with 30 vol.% binder: (a) TiC-IC50, (b) TiC-IC221, (c) $TiC_{0.7}N_{0.3}$-IC50, and (d) $TiC_{0.7}N_{0.3}$-IC221. 58

Figure 15. SEM and EDS analysis on single phase TiC sample, 1. W rich zones 2.TiC grain 59

Figure 16. Typical SEM example of the microstructure of a polished surface of $TiC_{0.5}N_{0.5}$ single-phase ceramic, sintered using the SPS method. 60

Figure 17. Representative SEM images of: (a) the core-rim structure in the TiC-Ni_3Al cermets, and (b) the absence of a core-rim structure in $TiC_{0.7}N_{0.3}$-Ni_3Al 70

Figure 18. Representative SEM image of a single phase TiC sample: 1. W rich zones, and 2. TiC grain. 71

Figure 19. Average OCP values, measured after 2 hours stabilization, for the TiC and Ti(C,N) cermets and single phase ceramics. 72

Figure 20. Potentiodynamic polarization curves for the single-phase ceramic and intermetallic phases. 75

Figure 21. Typical polarization curves observed for the TiC-Ni_3Al cermet, single-phase TiC, and single phase Ni_3Al, in a 3.5 wt.% NaCl aqueous solution. 78

Figure 22. Representative potentiodynamic polarization curves for (a), Ti(C,N)-Ni_3Al cermet compositions with, in a 3.5% NaCl aqueous solution and (b), A representative potentiodynamic polarization curve for the commercial WC-Co hardmetal in an identical electrolyte. 79

Figure 23. Average rates of corrosion, calculated from the Tafel slopes, relating to the potentiodynamic polarization curves the TiC and Ti(C,N) cermets with 30 vol.% Ni_3Al. All experiments were performed in an aqueous electrolyte with 3.5 wt.% NaCl. 81

Figure 24. Cyclic polarization analysis on the single-phase TiC and Ti(C,N) ceramics and the Ni_3Al intermetallic. All experiments were performed in an aqueous electrolyte with 3.5 wt.% NaCl. 84

Figure 25. Typical cyclic polarization curves obtained for (a), TiC- and Ti(C,N)-based cermet compositions and (b) Typical cyclic polarization curve obtained for the commercial WC-Co composition. All experiments were performed in an aqueous electrolyte with 3.5 wt.% NaCl. 86

Figure 26. SEM images obtained from the post polarization surfaces of the single-phase ceramics: (a)TiC, (b)$TiC_{0.7}N_{0.3}$, (c)$TiC_{0.5}N_{0.5}$, and (d)$TiC_{0.3}N_{0.7}$. Samples were polarized from -1 to +1 V (vs. SCE) in an aqueous electrolyte containing 3.5 wt.% NaCl. 88

Figure 27. SEM images obtained from post polarization surfaces of selected cermet compositions: (a) $TiC_{0.3}N_{0.7}$, and (b) TiC. Samples were polarized from -0.5 to +0.5 V (vs. SCE) in an aqueous electrolyte containing 3.5 wt.% NaCl. 89

Figure 28. Post polarization surface of the $TiC_{0.7}N_{0.3}$-Ni_3Al cermet. The sample was polarized from -1 to +1 V (vs. SCE) in an aqueous electrolyte containing 3.5 wt.% NaCl. 90

Figure 29. SEM micrographs obtained from the polished surfaces of the as-received cermets: (a) WC-Co 10vol.% and (b) WC-Co 30 vol.%. 100

Figure 30. The evolution of OCP values for WC-Co, prepared with 10 and 30 vol.% binder content: (a) through 2 hours of immersion, and (b) immediately after immersion. 101

Figure 31. Potentiodynamic polarization curves for WC-Co with 10 and 30 vol.% Co binder. 102

Figure 32. Cyclic polarization electrochemical analysis of WC-Co with 10 and 30 vol.% Co binder. 105

Figure 33. SEM images obtained from post polarization testing surfaces of WC-Co, with (a) 10 vol% Co and (b) 30vol% Co binder. 107

Figure 34. Post-corrosion EDS analysis of the WC-Co cermets. 108

Figure 35. ICP-OES analysis on the recovered post-corrosion electrolyte for the WC-Co cermets: (a) filtered particulate residue and (b) filtered solution. 109

Abstract

TiC and Ti(C,N) based ceramic-metal composites, or cermets, have drawn attention in recent years due to their low mass and high corrosion resistance, when compared to conventional WC-based 'hardmetals'. The aqueous corrosion behavior of TiC and Ti(C,N) based cermet materials has been investigated in the current work, using a variety of Ni_3Al-based intermetallic alloys as the binder phase. Cermets were prepared using a reaction-sintering route, with either 20 or 30 vol. % of the intermetallic binder, achieving densities in excess of 98% of theoretical. Furthermore, the individual TiC and Ti(C,N) ceramic phases, and the stoichiometric Ni_3Al intermetallic phase have been prepared using spark plasma sintering (SPS), in order to analyze the electrochemical characteristics of the parent compositions. In addition, two WC-Co materials were examined as a baseline composition. Measurement of the open circuit potential was used to determine the equilibrium electrochemical potential. The potentiodynamic and cyclic polarization responses of the cermets and single-phase constituent materials have been examined, with Tafel extrapolation used to determine the rate of corrosion for each composition. Inductively coupled plasma optical emission spectrometry was then applied to analyze the post-test corrosion solutions, in order to determine the elemental species that were liberated from the sample surfaces during corrosion testing. The microstructural effects of the corrosive environments were also assessed using scanning electron microscopy. It was demonstrated that selective attack of the binder occurs, and the extent of corrosion and primary mechanism depends on the amount of nitrogen in alloy composition, and the intermetallic binder composition and volume fraction. It is also shown that the present cermets exhibit corrosion rates as much as three orders of magnitude lower than WC-Co with identical binder contents.

List of Abbreviations and Symbols Used

CIP Cold Isostatic Press

EDS Energy-dispersive X-ray Spectroscopy

SEM Scanning Electron Microscope

XRD X-ray Diffraction

SPS Spark Plasma Sintering

ICP-OES Inductively Coupled Plasma Optical Emission Spectroscopy

Acknowledgments

I would like to thank those that guided me throughout this project, especially my supervisor Dr. Kevin Plucknett and my colleagues in the research team. I would also like to thank Dean Grijm for his assistance on manufacturing and maintenance of lab equipment, Patricia Scallion on SEM and Gerarld Fraser on ICP-OES. Furthermore, great appreciation is directed towards Boeing for the support and funding for the project.

Finally, I would like to thank my son, Suat for his help and support during years of my education.

Chapter 1. Introduction

In this study the primary aim is to thoroughly investigate the corrosion properties of a family of novel ceramic-metal composites, or cermets. Conventional cermets are composed of hard ceramic components held in a metal matrix binder phase, and are invariably produced using a liquid phase sintering process[1]. Cermets may be used in either bulk form or as a coating to improve the durability of the substrate material. The performance characteristics of cermet coatings have improved greatly in the past 15 years in many aspects, such as lowered cost, increased bond strength, reduced friction, as well as improved corrosion and erosion resistance. Carbide-based cermet coatings have shown excellent mechanical properties compared to their hard oxide counterparts[2].

Generally, cermets are materials with superior mechanical properties, with the advantage of having good toughness due to the presence of the ductile metal binder phase. This binder can be a pure elemental metal or an alloy consisting of metals such as Ni, Cr and Co. In addition to the ductility and toughness from the binder phase, the cermet hardness is also increased by the presence of the ceramic phase, such as tungsten carbide (WC), titanium carbide or carbonitride (TiC or Ti(C,N), respectively) or chromium carbide (Cr_3C_2). Ceramics are widely used in industry for their exceptional wear, corrosion, erosion and high temperature oxidation resistance, combined with a low coefficient of thermal expansion. Such properties make them an excellent option in the protection of more vulnerable metallic components. In order to maximize the advantage of using such materials in surface engineering we can add metal binders to the ceramics to achieve a certain amount of ductility. These cermets are particularly of interest for demanding

applications that require extended component lifetimes, such as coatings, cutting tools, linings, valves, saw blades, etc[3,4].

Currently, thermal spray coatings are being used in a wide variety of surface engineering applications, particularly where there is a need to minimize the wear degradation. In order to increase the quality of the cermet coating process, thermal spray technologies have been subjected to numerous studies, such as investigation of the bond strength between the metal and the ceramic matrix, minimizing residual stress, and developing low porosity deposits. Furthermore, cermet materials have been subjected to dry erosion, abrasion and corrosion resistance (for aggressive environments) tests, in order to evaluate their performance characteristics, and they have attracted much attention in the coating industry[5].

Conventional WC 'hard metals' (WC cermets with Co- or Ni-based matrices and high carbide contents) are composed of hard WC particles embedded in a tough metallic matrix. This family of materials have shown outstanding erosion resistance in dry conditions, and have been developed and refined over many decades. However, when applied in a corrosive environment these materials suffer from serious limitations[6]. The Co metal binder is particularly susceptible to corrosion and degradation, which influences the overall performance of the cermet structure[4].

Typically, corrosion events in cermets begins with formation of pits, followed by galvanic corrosion at the ceramic/metallic interphase, dissolution of the binder phase and, finally, removal of the carbide grains[7,8]. When dissimilar metals and alloys, with different electrode potentials, come into contact in an electrolytic solution, one metal acts as an anode while the other is the related cathode. The potential difference between the metals

is the driving force for dissolution of the anodic member of the galvanic couple in the electrolyte, with the possible associated formation of a deposit on the cathodic metal[9].

In case of conventional hard metals such as WC-Co, Co binder with lower corrosion potential becomes the anode and oxidizes while WC stays largely unaffected. This phenomenon leaves a skeleton of WC behind, which can fail under the weakest mechanical action[10]. Galvanic coupling between the Co binder and WC results in synergistic effects, which accelerate the dissolution of Co and destruction of the composite WC structure in the 'hard metals' when compared to the pure compounds[10].

Microstructural parameters such as the composition of the binder phase, the related size and morphology of both the metallic and ceramic phase, pH, the potential of the system and the amount of the binder phase in the ceramic-metal composite are the most important factors in defining the properties of cemented carbides, including the corrosion resistance. The heterogeneous microstructure and the composition of the binder phase results in a very complex corrosion mechanism in WC-Co, and other cermets[11]. As a consequence, there is still much to be understood about this process[11].

It is preferable that the single-phase ceramic and metallic components are also investigated individually, under similar electrochemical conditions, in order to obtain a clear understanding of the degradation mechanism(s) in the cermet material and to provide potential solutions to unwanted behavior. For example, it has been found that in WC-Co hard metals, Co is responsible for the overall corrosion response of the composite[7,11]. Similar studies have suggested that the corrosion response of the binder phase (Co) in the cermet composition can be altered through the alloying of this phase with secondary elements[12]. A number of research studies have been carried out on alternative binders to Co, such as Ni, Ni-Cr, Ni-Cr-Mo, and Fe[3,4,14]. Recently, it has also

been shown that the addition of Ru as a binder has had a stabilizing property[15]. However, limitations such as high density, in addition to the poor oxidation and corrosion resistance of the binder in conventional hard metals have drawn attention towards titanium carbide (TiC) and titanium carbonitride (Ti(C,N)) based cermets. Typical metallic binders for these type of cermets are nickel and cobalt[16], ductile nickel aluminides and stainless steel binders [17–19].

The effects of chemical composition on the mechanical properties of Ti(C/N) based cermet material have been widely studied. However, the number of investigations performed on the corrosion mechanism(s) of these cermets is limited. Data that is available relating to electrochemical measurements on WC based cermets can be used as a general guideline for alternate cermet systems. For example, using binders such as Co, Cr or Ni can have significant effects on improving the corrosion properties in coating materials by eliminating micro-cracks, which are the major infiltration paths for corrosive solutions[20,21]. Micro-galvanic corrosion at the metal/ceramic interface (which is a typical form of corrosion for multiphase materials with different oxidation characteristics) can potentially be minimized or eliminated by modifications applied to both phases[22,23].

In the current study, TiC and Ti(C,N) based cermet samples and single-phase components compositions have been prepared with a stoichiometric Ni_3Al metallic binder phase (at a content of 30 vol.%). The cermet samples manufactured were processed by using a mixture of powdered ceramics TiC, $TiC_{0.7}N_{0.3}$, $TiC_{0.5}N_{0.5}$, and $TiC_{0.3}N_{0.7}$ and a blend of metallic Ni and Ni/Al. Cermet compositions were sintered using a simple *in-situ* reaction sintering approach[24], while the single-phase ceramic and metallic constituents were prepared using spark plasma sintering (SPS) to analyze the electrochemical characteristics of the parent components. The characteristics of the intermetallic phase, such as

oxidation/corrosion resistance, yield stress, etc., was altered by addition of Cr, B and/or Zr. The chemical and physical characteristics of each phase have been reviewed. The influence of composition on the electrochemical behavior of each material was then assessed, using a variety of methods, including open circuit potential, potentiodynamic polarization, and cyclic polarization.

Additionally, the corrosion responses of WC-Co cermets were studied to perform a baseline comparison between the materials manufactured for the current study and commercially produced 'hard metals' used for similar applications.

Post-test corrosion solutions were analyzed using inductively coupled plasma optical emission spectrometry to determine elemental species liberated from the samples, while microstructural changes were assessed using scanning electron microscopy. It is concluded that selective attack of the binder occurs for all of the tested cermets, while the extent of corrosion and primary operative mechanism depends on the nature and amount of binder content.

Chapter 2. Literature Review

The background information relating to the objectives of the present study is provided in this chapter. A brief overview of the general electrochemical nature of corrosion and in cermet compositions, in particular, is presented. In addition, the associated electrochemical test methods and forms of corrosion are also reviewed. The methods that are subsequently used to characterize the corrosion response of specific compositions and approaches to performing proper corrosion measurements are discussed in detail.

2.1. Introduction to Corrosion Response of Cermets

Cemented carbides are widely used in applications where wear and corrosion resistance are important. The combination of ceramic and metallic phases provides high strength and stiffness to the overall composition. 'Hardmetals' based on WC and TiC have undergone constant development during the past seventy years. TiC and Ti(C,N) have been demonstrated to exhibit high electrical conductivity and a stable chemical response in acidic media[17]. The combination of physical characteristics of cermets has resulted in a large number of applications, including use in the aerospace industry. The wear and corrosion resistance of these materials are critical characteristics for such industries, along with minimising the mass. For components that are constantly exposed to highly corrosive environments (such as landing gear), the characteristic mechanisms and rates of corrosion need thorough investigation in order to maximize the operating lifetime of the part.

Corrosion is the destructive result of chemical reactions occurring between metals and their environment, which degrades the useful properties of materials and structures, including their strength, appearance and permeability to liquids and gases. During the

corrosion of a metal an amount of energy is emitted that has been used to initially extract the metal from its mineral compound form, thus corrosion has been called extractive metallurgy in reverse[25]. The most familiar definition of corrosion is the electrochemical oxidation of metals in reaction with an oxidant, such as oxygen.

Metallic materials require exposure to moisture and oxygen in order to corrode, but certain substances can strongly affect the rate of reaction. Corrosion can spread across a wide area, uniformly corroding the surface, or just be focused locally and create a pit or crack. It is essential to know that corrosion is a controlled diffusion process, and only occurs on the exposed surface. This explains the main focus of many corrosion control applications, which is targeted at a reduction in the activity of the exposed surface, such as passivation and chromate conversion, thereby increasing the corrosion resistance of the treated surfaces. However, not all of the corrosion mechanisms are easily visible and/or predictable[26].

The mechanism of corrosion reaction in cermet coatings is particularly complex, encompassing not only the interface(s) between the coating, the environment and the substrate material, but also potential galvanic coupling that may be occurring within the coating itself between the ceramic and metallic components. In order to achieve a better understanding of these mechanisms, the kinetics, thermodynamics and electrochemical properties of the corrosion process in these materials needs to be fully understood. Moreover, study of the corrosion behaviors in cermet coatings (and many other materials) requires suitable tools and measurement techniques, such as a variety of electrochemical polarization methods, Tafel plots, and electrochemical impedence spectroscopy (EIS). Equally important, the subsequent microstructural and chemical analyses on post-corrosion samples and electrolyte are then used to identify the type of corrosion attack

(pitting, galvanic, crevice and/or high temperature), and the quantity of dissolved material in the recovered corrosion solution. Based on the metallic characteristics of the binder, cermet coatings can undergo corrosion attack without contribution from the substrate material. It has been shown that localized corrosion occurs at the metal-ceramic interfaces within the coating, and often leads to selective dissolution of the metallic binder phase. Once the binder is lost, the hard phase skeleton is extremely susceptible to further mechanical or corrosive degradation.

The level of interconnected porosity or damage (e.g. cracks) within the deposited coating is one of the most important factors for the component's structural integrity. The presence of such pores or damage in the structure of the coating can result in penetration of the electrolyte into the coating, which can even reach the substrate material, leading to increase the corrosion of the coating. However, coating materials with low levels of porosity/damage have still also shown high degrees of corrosion, due to selective attack of the metallic binder[27–29].

The number of studies that has been performed on corrosion mechanisms of TiC and Ti(C,N) based cermet materials is very limited. However there is considerable information available on electrochemical measurements and data interpretation for related WC-based cermets. Such information can be used as a general guideline to achieve a better understanding of the corrosion behavior of broadly related cermet materials.

Most studies on WC coatings have suggested that incorporation of metallic binders, such as Co, Cr or Ni, have significant effects on improving the corrosion properties in coating materials by eliminating porosity and micro-cracks, which are the major infiltration paths for corrosive solutions[20,21]. The superior corrosion erosion resistance in WC-Co-Cr compared to WC-Co coatings is an example of where compositional modification can

have significant beneficial effects. Microstructural and chemical analyses on post-corrosion surfaces have shown a considerable amount of micro-galvanic corrosion in WC-Co coatings, while Cr addition helped to suppress the dissolution of the binder material into the solution by formation of a more protective passive oxide film on the surface. One study has suggested a three-stage mechanism for the localized corrosion attack to proceed on the surface of the WC based cermet materials. Initially, pits form on the surface of the coating, then galvanic corrosion occurs between phases with different chemistries and corrosion potentials, and in the last stage, galvanic and crevice corrosion take place, which results in failure and removal of the coating with small forces from the environment[7,8].

2.2. Electrochemical Nature of Corrosion

The process of corrosion almost always comes with transfer of electronic charges between materials within an aqueous solution. In order to achieve a better understanding of the various types of corrosion and their nature, it is necessary to discuss the electrochemical aspects of the oxidation reaction(s).

2.2.1. Electrochemical Reactions

Electrochemical reactions in the process of corrosion consist of two half-cell reactions; the oxidation reaction, which takes place at the **anode** (Equation 1)**,** and the reduction reaction, which occurs at the **cathode (**Equation 2**)**. If a metal, M, for example with a valence number of +2, undergoes a corrosion process in an aqueous environment with a neutral pH, the half-cell reactions can be written as:

Anodic Reaction: $\mathrm{M} \rightarrow 2\mathrm{M}^{+} + 2e^{-}$ **Equation 1**

Cathodic Reaction: $2\mathrm{H}^{+} + 2e^{-} \rightarrow \mathrm{H}_2$ **Equation 2**

The fundamental components in an electrochemical corrosion cell include an anode, a cathode, a conductive environment for ionic movement, which is called the electrolyte, and an electrical connection between the anode and cathode for the flow of electron current [20]. The metal reacts with the (acidic) solution, and becomes soluble in the electrolyte. The anodic reaction is an oxidation reaction, which brings the valence number of the metal from zero to +2, thus releasing electrons. On the other hand, reduction takes place at the cathodic reaction, which consists of decreasing the oxidation state of hydrogen from +1 to zero by consuming the electrons released from the anodic reaction. The summation of these two reactions involving the transfer of electrons from the metal and reaction with H^{+} to form H_2, is given in Equation 3:

$$2\mathrm{M} + 4\mathrm{H}^{+} \rightarrow \mathrm{M}_2 + 2\mathrm{H}_2 \quad \textbf{Equation 3}$$

By increasing the hydrogen evolution, a reduction in the rate of reaction on the anodic side takes place. Most corrosion reactions involve water in liquid or condensed form except for dry corrosion, which uses a solid-state electrolyte for the charge transfer.

The corrosion reaction is considered to be an electrochemical reaction, and negative potential can be created by adding excess electrons, which is the basis for many corrosion protection processes.

There are a few important cathodic reduction reactions in the concept of corrosion, for which the reduction of hydrogen ions in an acidic solution represents the simplest form of such reactions. There are less frequent forms of cathodic reactions, such as the reduction of dissolved oxygen in acidic and natural solutions, which are exposed to ambient air (Equation 4):

$$O_2 + 2H_2O + 4e^- \rightarrow 4OH^- \qquad \textbf{Equation 4}$$

$$O_2 + 4H^+ + 4e^- \rightarrow 2H_2O \qquad \textbf{Equation 5}$$

As is shown in Equation 6, water can be used for a reduction reaction in the absence of all of the other possible cathodic reactions:

$$2H_2O + 2e^- \rightarrow H_2 + 2OH^- \qquad \textbf{Equation 6}$$

Depending on the type of metal or alloy in a corrosion process, in a specific environment, different anodic and cathodic reactions can be written in different ways. According to some studies on WC-Co cermets, produced as landing gear coatings for aerospace applications, the relatively poor corrosion response of the manufactured material has been explained by means of a galvanic corrosion reaction occurring at the ceramic/metallic interphase. It has been shown that cathodic and anodic reactions have taken place, with the ceramic as the cathode and the metallic binder as the anode, which resulted in dissolution of the binder during corrosion[20,30,31]. It has been verified that the elemental composition of the phases in the cermet structure affects the rate of oxidation resistance

significantly. For example, the addition of N to the ceramic phase in TiC based cermets has resulted in a reduction of the ceramic grain size, which promotes a higher corrosion resistance by providing space for a higher area of the corrosion resistant oxide layer[32,33]. However the effects of the electrochemical characteristics of each element within the cermet composition, along with the individual ceramic and metallic phases is yet to be widely studied. The effects of the ceramic composition on the corrosion behavior of TiC and Ti(C,N) based cermets, with various Ni_3Al-based binder alloys, is the main focus of the current study. Consequently, the results of corrosion tests have been used to verify the nature of the electrochemical reactions in the manufactured samples.

2.2.2. Polarization

Once cathodic and anodic reactions are at equilibrium, a driving force is needed for the flow of electrons between the anode and the cathode. This driving force is the difference in potential between the anode and cathode. The reason for the existence of such potential differences is the difference in the tendency of the anode and cathode towards continuing the reaction. The potential of the electrochemical cell is then simply determined by measuring the tendency for the reaction that takes place spontaneously.

Once electrons leave the metal, the potential of the surface becomes more negative. This negative charge is created by the electrons that are waiting to be consumed at the metal electrolyte interface. On the other hand, the reaction is not fast enough to accommodate these electrons, which results in a negative change in potential, also known as ‘cathodic polarization’. Similarly a deficiency of electrons in the metal, freed at the interface, produces a positive potential charge known as ‘anodic polarization’. The anodic polarization represents the tendency of the metal to dissolve from the exposed surface.

Therefore, the anodic polarization can be called the driving force for corrosion by anodic reactions. In the steady state, electrons can be exchanged via the available cathodic and anodic reactions. The anodic polarization, which is the difference between the potential of exposed surface (E), and corrosion potential, (E_{corr}), is defined in Equation 7:

$$\varepsilon_a = E - E_{corr} \qquad \textbf{Equation 7}$$

2.2.3. Passivation

The rate of corrosion decreases in many metals above a critical potential, known as the passivation potential E_{pass}. Metal corrodes at relatively a high rate at lower (more negative) values for E_{pass}, while passive corrosion rates are very low (Figure 1)[25]. The cause of the decrease in corrosion rate at E_{pass} is the formation of thin, hydrated oxide films on the corroding surface that result in inhibitation of the dissolution process. In many alloys chromium is used as the 'key' alloying element, because of formation of a passive oxide film in a corroding environment. Moreover, passivation behavior of a metal is also highly dependent upon the potential or oxidizing power of the solution. For example, a metal can be passive in aerated water and active in de-aerated salt water.

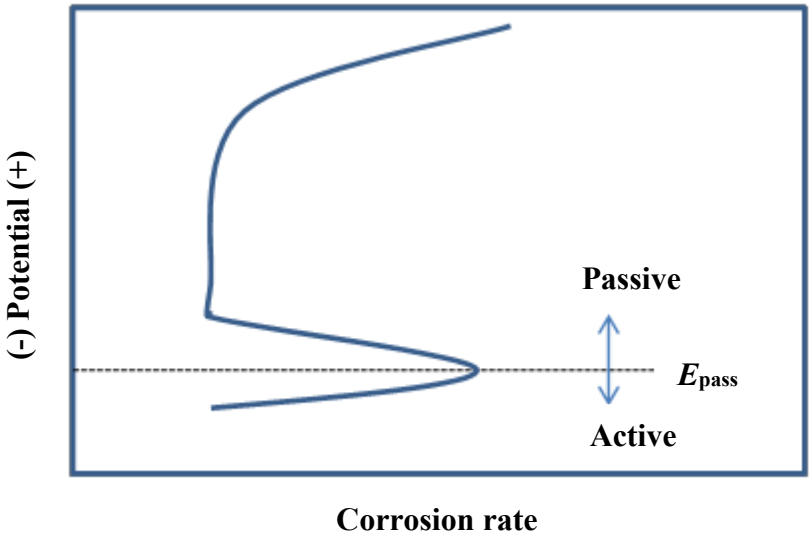

Figure 1. Passivity at potentials above polarization potential.

Identifying the passivation condition is useful in modifying corrosion damage, however it is important to know that even a high quality alloy can corrode if its ability to form a passive oxide film is hindered. Proper material selection of the material for specific environments is consequently the key factor in the production of long lasting parts. A fragile passive film can break down due to chemical or mechanical factors, and result in major localized modes of corrosion such as pitting corrosion, crevice corrosion and stress corrosion cracking.

In metal ceramic composites, the binder and its composition need to be selected carefully, by taking the aggressiveness of the environment into account. Investigating the passivity of the metal binder then becomes an essential factor in designing cermets, and modification of their binder alloys, since dissolution of the binder during corrosive attack can result in the destruction of the overall composition. For example, in a study by Wentzel *et al.*, on the erosion-corrosion resistance of WC-based 'hardmetals', it has been

concluded that the addition of high Ni grades of binder results in better passivation behavior compared to the grades with lower amounts of Ni in their composition[5]. It has also been noted that the passivation behavior of the Ni binder causing its superior corrosion resistance may not be of much value under conditions when the formed passive film is continuously being removed, for example due to erosion or mechanical forces. In such conditions the hardness, deformation characteristics and possible phase transformations of the binder may be more important in determining the quality of the final composite.

2.2.4. Electrochemical Thermodynamics and Electrode Potential

A change in the electrochemical potential or the activity of the electrons, or even their availability at the surface of the metal, can have significant effects on the rate of the corrosion of the binder in cermet materials. The electrochemical changes, directly change the energy level during the corrosion reaction, which is the driving force for the direction of the reaction. The thermodynamic properties in the reaction can therefore be manipulated to make it impossible for the reaction to proceed in the direction of corrosion. The change of energy associated with a chemical reaction, ΔG, can be involved with an electrochemical potential at equilibrium through the fundamental relationship presented in Equation 8:

$$\Delta G = -nFE, \qquad \textbf{Equation 8}$$

where E is the involved electrochemical potential, n is the number of electrons that are being exchanged, and F is Faraday's constant (equal to 96,500 coulombs per mole of electrons). The (-) sign in Equation 8, is included to confirm that a positive potential of E will result in a negative free energy for the reaction to be spontaneous. The listing of the

values of *E*, for standard half-cell electrode potentials is known as the electromotive force (EMF) series. All of the half-cell potentials in the EMF series are written as reduction reactions. The standard hydrogen electrode (SHE) is invariably assumed as the reference electrode, and all other electrode potentials in this listing is measured with respect to SHE[34] .

Another thermodynamic factor, which has a significant effect on corrosion reactions, is the factor of concentration. The equilibrium conditions require the same level of chemical activity for the products and reactants. The change in energy activity due to a change in concentration of reactants and products can be then calculated using Equation 9, which is also known as the Nernst equation[34]:

$$\Delta G - \Delta G^{\circ} = RT\ln \frac{(B)^b * (H_2O)^d}{(A)^a * (H^+)^m} \qquad \textbf{Equation 9}$$

where, ΔG is the Gibbs energy, ΔG° is the Gibbs energy at standard condition, *R* is the gas constant, *T* is absolute temperature, *A* is the oxidized specimen and *B* is the product. The upper case letters account for the concentration. Now by simplifying Equation 8 andEquation 9 the cell potential can be calculated (Equation 10):

$$E = E^{\circ} + \frac{RT}{nF}\log \frac{(A)^a * (H^+)^m}{(B)^b * (H_2O)^d} \qquad \textbf{Equation 10}$$

Where E is the cell potential, E° is the cell potential at standard condition A is reducing agent and B is the oxidizing agent. The direction of the reaction can be determined by the conventional assumption that the more negative cell potential always precedes through oxidation and the more positive half-cell will go through reduction[35].

2.2.5. Electrochemical Kinetics of Corrosion

Thermodynamically, corrosion is possible in most environments but what is important is the rate at which the reaction takes place. Since the corrosion is an electrochemical reaction, and all of the electrochemical reactions involve the flow of electrons from one site to another, it can be concluded that the rate of electron flow between reacting surfaces correlates with the rate of corrosion. The value of the mass, *m*, involved in the corrosion reaction and liberated from the surface of the specimen can be calculated using Equation 11, also known as Faraday's law[36]:

$$m = \frac{ita}{nF} \qquad \textbf{Equation 11}$$

where, *n* is the valence number of the ions of substance, *i* is the electric charge passed through the substance for time t, *a* is the molar mass of the substance and *F* is faradays constant (96,485 C/mol). Equation 11 can be derived into a simpler form by dividing by the unit area, *A*, and time, *t*, to directly calculate the rate of the corrosion, *r*, which is the mass loss per unit area with, *I*, being the current density:

$$r = \frac{Ia}{nF} = \frac{m}{ta} \qquad \textbf{Equation 12}$$

The exchange current density *I*, can be measured for values as small as 10^{-9} A/cm^2 in the laboratory environment, once the system reaches the equilibrium *r*, and it has an equal value for both sides of the cathodic and the anodic reactions.

The rate of penetration per unit time can be also calculated by dividing Equation 12 by the density of the material being evaluated. It should be emphasized that the corresponding calculation for alloys is more complex, due to the inclusion of 'equivalent weight' (EW) calculations. In the case of more complex compositions, such as alloys and

cermets, half-cell reactions occur simultaneously at a common surface, each with their specific rate of reaction and current density.

In this instance, EW is referred to as the mass of metal (in grams) that needs to be oxidized in a given redox reaction, by the passage of one Faraday (96,485 C/mol) of electric charge, and produce exactly 1 mole of electrons. For a pure element this number is calculated by dividing the atomic weight of that element by its number of valence electron(s) (i.e. the number of electrons that are oxidized during the corrosion reaction). However, this calculation is only convenient if the oxidation process is uniform for all of the surface area. The calculation of the EW for alloys is rather complex, due to the distinct behavior of each element present in the composition, towards the oxidation reaction. For the electron equivalent, Q, of unit mass of oxidizing composition (1 gram), EW can be calculated following:

$$\mathrm{EW} = \frac{1}{Q} \qquad \textbf{Equation 13}$$

Q can be mathematically found by accounting for the mass fractions, atomic weights and number of valence electrons for each active element during the electrochemical reactions[37]:

$$Q = \sum \frac{n_i f_i}{W_i} \qquad \textbf{Equation 14}$$

where f_i is the mass fraction of the ith element in the alloy, W_i is the atomic weight of the ith element in the alloy, and n_i is the valence of the ith element of the alloy.

2.3. Forms of Corrosion

Although, cermet coatings are a good option to prevent the corrosion and wear of the substrate material, many studies have shown that each possible component, and their electrochemical effects with each other, must be closely investigated for specific applications. As noted earlier, there are different types of corrosion, such as uniform corrosion, crevice corrosion, pitting corrosion, galvanic corrosion, environmentally induced cracking, dealloying, hydrogen damage, intergranular corrosion fretting, and high temperature corrosion. In studies related to the corrosion response of cermet coatings, a complex mechanism is generally suggested. It has been shown that during the corrosion reactions, not only are interactions taking place between the cermet coating, the corrosive environment and its substrate, but also galvanic processes may be occurring between components within the coating itself. Once the binder matrix has been compromised, the structure will be very vulnerable to be destructed by corrosive and erosive systems[27,29].

2.3.1. Localized Corrosion

On the surface of the passive metal, localized corrosion can occur as an accelerated attack in localized sites. This can result in the removal of the protective passive film in contact with the corrosive environment and dissolution of the material[38,39]. This type of corrosion usually occurs in the form of pitting of the surface(s) in contact with the corrosive environment, and intergranular corrosion in materials with vulnerable grain structure. The earliest stages of localized corrosion are not well understood, due to the rapid chemical reactions occurring on micron/sub-micron lengthscales. However it is known that localized corrosion takes place in 2 stages. The first of these occurs immediately after initiation of the reaction; metastable pits grow at high rates at the surface of the passive

layer defect. In the second stage, once stable growth of the localized corrosion is reached (in suitable conditions), re-passivation takes place. Localized corrosion initiates above the corrosion potential, E_{corr}, and re-passivates at another lower potential, E_{rp}. Localized attack can be prevented by maintaining the re-passivation potential by suitable safety margin above the corrosion potential (e.g. 100 mV or more)[38,40].

2.3.2. Crevice Corrosion

Crevice corrosion is a form of localized corrosion, which is a result of failure of the passive film. To study this type of corrosion the test environment has to be a strong oxidizer, in order to favour passivity. Then chloride is used to break the passive layer and initiate the localized corrosion. Depending on the aggressiveness of the environment and the type of coating, crevice corrosion can take place in different forms[41]. The general form of crevice corrosion is corrosion occurring in confined spaces (crevices). Such spaces provide an environment to form cells with different aeration, and corrode the material from the inside. Composite materials such as cermets, are very susceptible to this type of corrosion due to the probable existence of suitable sites within the compositional interface regions, relating to the quality and characteristics of the composite. To rank the resistance of the different materials to this type of corrosion the tests are typically conducted at a critical crevice corrosion temperature. It has been found that smaller cervices can generate more damage than larger crevices, since smaller volumes require enrichment mechanisms. This can also illustrate the fact that metal-non-metal composite materials are more vulnerable because they form smaller crevices[42].

Figure 2 illustrates the degradation of WC/17Co after electrochemical polarization at 2000mV[21]. According to the literature, corrosion has degraded the top surface to a

maximum depth of ~10 μm, and signs of crevice corrosion along the boundaries of the top deposition layer are observed (denoted by the black arrows).

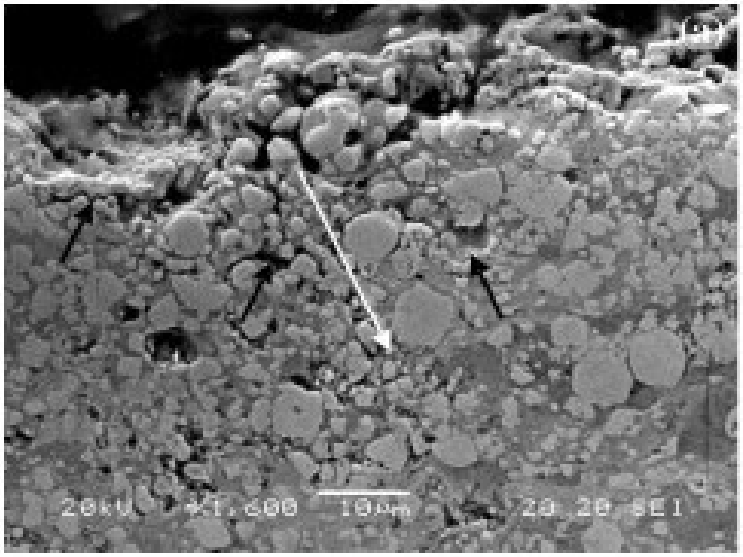

Figure 2. Cross-sections of WC–17Co after cyclic polarization to 2000 mV (white arrow: a likely electrolyte path, black arrows: crevice corrosion).

2.3.3. Pitting Corrosion

Passivation takes place in certain environments, such as high concentrations of elements like chloride that can disable the surface of coated material to regenerate its passive film. In fact, even if the entire surface remains protected, small local instabilities will result in degradation of the oxide film in these regions. Corrosion at these points will be greatly intensified, creating pits, which can continue to grow even after removal from the corrosive environments due to an autocatalytic process. This process is the direct result of low levels of oxygen and pH in their interior surface. Long and narrow pits can cause stress concentration and failure before being detected. Pitting corrosion is often prevented by controlling the environment that the alloy is being exposed to[42].

Pitting remains amongst the most common and damaging forms of corrosion that occurs in coating materials. Pitting corrosion reactions are often initiated at the substrate–coating interface and small structural defects, such as pinholes, pores and micro-cracks. Thus, the proper chemistry of the substrate–coating interface must be chosen[43]. Formation of pits within the passive film on the surface of WC-Co is shown in Figure 3. The results of chemical analysis has determined a composition of W, Co and O in the oxide layer[21].

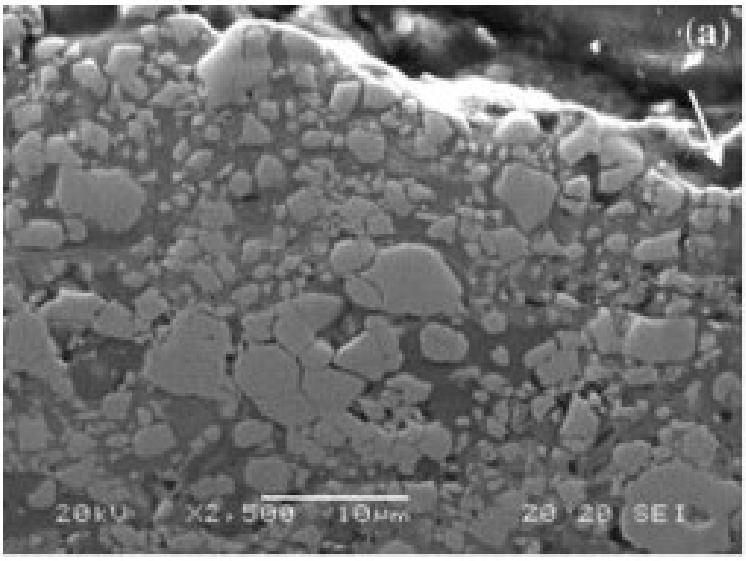

Figure 3. Cross-sections and formation of pits on surface of WC–Co after polarization at 500 mV.

2.3.4. High Temperature Corrosion

High temperature corrosion is a chemical deterioration of a material as a result of being exposed to a high temperature corrosive environment. This type of corrosion occurs when a metal is subjected to mechanical interactions with high friction rates or hot atmospheres containing oxygen or other elements that can result in oxidation of the material. As explained in previous sections, corrosion is a chemical reaction and all chemical reactions take place more rapidly at elevated temperatures. As a rough rule of thumb, the rate of

reaction may double with every 108°C[44]. High temperature corrosion has been an important issue in metallic and ceramic materials for energy conversion and chemical industrial processes[44]. Materials that are exposed to extremely harsh conditions in processes such as aerospace, power generation and even car engines have to resist for long periods at high temperature in order to achieve high efficiency. In some cases the products of high temperature corrosion can produce positive results by the formation of an oxide layer on the surface of the specimen and protect the material from further atmospheric attacks and even reduce wear during high temperature sliding contact of surfaces[45].

Due to the significant influence of the nature of the binder phase on the performance of a cermet, new binder systems with good high temperature properties need to be developed to extend the use of such composites[45]. TiC-based cermets with Ni and Fe alloys are currently used in applications that acquire high wear and corrosion resistance. Figure 4 is an example of the effect of the amount of binder on the wear resistance of the oxide layer formed under high temperature wear conditions. The results of this study have shown that an increase in 10 vol.% for the binder phase of the cermet composition results in removal of the protective oxide layer under wear conditions.

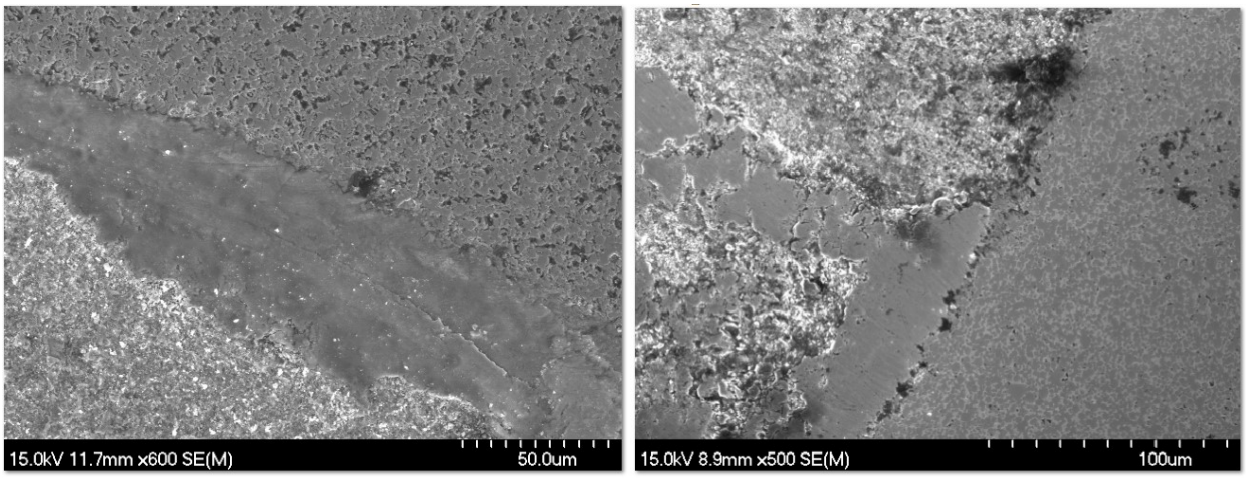

Figure 4. Wear tested surface of (a) $TiC_{0.5}N_{0.5}$-20vol% SS316 and (b) $TiC_{0.5}N_{0.5}$-30vol% SS316.

2.3.5. Erosion Corrosion

Most non-metallic materials, such as ceramics, consist of metal atoms that have satisfied their reactivity by forming a bond with other active atomic species (e.g. forming oxides, nitrides, etc.). This explains the fact that most ceramic materials are highly resistant to corrosion and have very little free chemical energy in their structure. However, these unreactive materials can degrade by physical means such as erosion or mechanical wear, which simply results in loss of the material in specific environments.

By definition, erosion-corrosion is "the acceleration in the rate of deterioration of metal caused by the combined action of mechanical erosion and electrochemical attack" [2]. This synergistic effect can cause a much greater level of damage and material loss rate than would have occurred by erosion or corrosion alone, and consequently severely shorten the component life[28]. In addition, protection against erosion in the system does not only guarantee the coating itself, but also can prevent the damage to the substrate by

decreasing the likelihood of corrosion. Erosion-corrosion attack is simply the material loss under the combination of these two phenomena and is presented in Equation 15:

$$T = E + C + S \qquad \textbf{Equation 15}$$

where, E is the loss of material by only mechanical erosion processes, C is the loss of the material by electrochemical corrosion processes, and S is the synergy, which accounts for the combination of interactions between the two processes[46,47]. Thus, synergy can be referred to as the difference between erosion-corrosion and the summation of its two parts and can be expressed by Equation 16 and Equation 17[46]:

$$S = T - (E + C) \qquad \textbf{Equation 16}$$

The effects of erosion and corrosion in the definition of synergy can be identified by introducing two new variables as ΔE and ΔC. Here ΔE is the enhanced loss of material during the erosion, due to the existence of corrosion, and ΔC is the enhanced loss of materials during corrosion, due to the existence of erosion. Equation 17 can then be written in order to calculate the effect of synergy[47,48]:

$$S = \Delta E + \Delta C \qquad \textbf{Equation 17}$$

The protective corrosion film can be removed due to mechanical forces that are created by erosion and create fresh reactive corrosion sites. In a study on mechanisms of enhanced erosion-corrosion, and aspects that can result in positive synergy effects, the following observations have been made[49]:

(i) Increased mass transport arises due to high turbulence levels,

(ii) There is a lowering of fatigue strength by corrosion,

(iii) Surface roughening of the specimen occurs during particle impact, causing enhanced mass transfer effects and increased corrosion rates.

In addition, corrosion-enhanced erosion mechanisms (ΔE) are also possible, including[46]:

(i) The removal of work hardened surfaces by corrosion processes, which exposes the underlying base metal to erosion mechanisms,

(ii) Preferential corrosive attack at grain boundaries resulting in grain loosening and eventual removal.

2.4. Common Techniques in Corrosion Measurement

The field of corrosion measurement, control, and prevention covers a very broad spectrum of technical activities. Corrosion control employs variety of techniques such as materials selection, cathodic and anodic protection, chemical treatment and etc. corrosion measurement techniques are also used to determine the corrosive nature of environment and its interaction with specific material to construct a complete data set to enable corrosion control and prevention methods to be optimized.

The most common techniques used in measurement of the electrochemical behavior of materials include the following aspects:

- Simulated environments (usually simulated 'sea water' with a known concentration of NaCl)
- Polished test specimen as the working electrode surface

- Saturated calomel electrode (SCE) as a reference electrode (or alternatively Ag/Ag, Cl/KCl)
- Platinum mesh as a counter electrode
- Potentiostat
- Cell (flat cell, …)

The specimen that is to be tested, is placed into the electrolyte opposite to the platinum mesh and reference electrode. The potentiostat is used for controlling the potential difference between the specimen and the reference electrode, and the responses such as current flow between the specimen and the counter electrode are then recorded. A frequency response analyzer is connected to the power source and a computer, which runs the corrosion evaluation software.

In most cases the samples will be immersed into the electrolyte solution for a period of time prior to commencing the electrochemical test, typically between 30 minutes to 4 hours (this depends on the behavior of the surface towards reaching what is termed the open circuit potential (OCP)), in order to reach steady state. The OCP is then typically used as the starting point for the actual measurements. Hereafter, the behavior of the specimen is analyzed using a number of corrosion measurement techniques.

There are several techniques for corrosion rate determination, these range from methods that measure the cumulative results of corrosion over some period of time, to those that measure the rate of corrosion instantaneously for environmental effects analysis. According to a number of studies on corrosion testing of ceramics and ceramic-metal compositions, the screening corrosion tests applied are a direct adaptation of the methods and equipment that have been developed for corrosion testing on metals[50].

The corrosion testing methods can be electrochemical or non-electrochemical. However, the basics of these tests are always designed with two components in mind, namely the environment medium and the specimen. The medium can be either static or dynamic, for erosion-corrosion effect testing. During and/or after the test (for specific time intervals), the sample can be analyzed for weight and/or dimensional changes, chemical composition variation, or X-ray analysis and metallographic examination. Depending upon the potential application(s) of the tested materials, some or all of the examinations can be done for each sample.

Furthermore, the test media is analysed for the existence of preferential corrosion. The standard process indicates that two tested and untested specimen have to be analysed in order to determine the extent and nature to which corrosion is occurring in a specific material. There are specific guidelines and standards for surface preparation of the test materials. In most cases samples are polished prior to electrochemical and metallographic analysis.

The characteristics of the electrochemical reaction can be determined by studying the current response, and its relation to the potential at the surface in the test environment. Potential-pH (*E*-pH) diagrams are commonly used classify the domain of stability for chemical species in a given metal-solution system. These diagrams can also be designed for applications when the electrolyte is at higher temperatures. In this section a number of experimental measurements that are suitable for characterization of cermet materials are briefly explained.

2.4.1. Electrochemical Methods

Electrochemical instruments are valuable tools to identify the corrosion behavior of many materials. Since corrosion consists of electrochemical oxidation and reduction reactions, electrochemical measurements can provide information relating to the most important factors that are needed to characterize the nature and extent of corrosion. The reactions that occur during a corrosion process create the corrosion potential. This potential cannot be measured directly and should be measured by the potential difference between the corrosion test specimen and a reference material, such as a saturated calomel electrode (SCE). The value of the corrosion potential (E_{corr}) and current density (i_{corr}) can be specified by performing a potentiodynamic polarization test, and simultaneously measuring the current flow across the electrolyte solution. Corrosion-realted mechanisms, such as passivation and pitting, are slow processes and can be studied by applying 'accelerating' external potentials to the system. Then curves of the applied potential versus the specific current denties can be plotted for further quantitative interpretation and calculations. It should be noted at this point that is important to account for resistance errors during measurements of corrosion to avoid experimental errors.

The basis of the electrochemical measurements that should be undertaken depends on the factors that are to be obtained from the results of the experiments. The measurements can be undertaken for a variety of operational 'modes', including potentiodynamic, potentiostatic, galvanodynamic and galvanostatic. Most electrochemical measurement techniques scan the potential of the working electrode and its resultant current. Since the applied potential is constantly changing, this method is referred to as potentiodynamic measurement. In the case of potentiostatic tests, plots obtained for the flowing current density versus time, at a constant potential (i.e. potentiostatic), are very beneficial in the

study of the resistivity of the oxide layer evolved at a specific potential over a finite period of time[51,52].

Galvanodynamic measurement is a technique in which the current of the cell is controlled to obtain a series of potentials. Similarly, galvanostatic testing is another method that plots the changes in potential versus time by maintaining a constant current value[53].

Commonly used electrochemical techniques in corrosion testing that can aid in identifying the corrosion processes of cermet materials are potentiodynamic polarization, potentiostatic polarization, cyclic polarization, and polarization resistance responses.

2.4.2. Potentiodynamic Polarization

The potentiodynamic polarization test is commonly used to describe the corrosion behavior of an electrochemically active material in corrosive environment in the form of a current-potential relationship, by continuously scanning its anodic potential as the potential increases from negative to positive. A complete current–potential profile can be plotted in a matter of a few minutes to a few hours, depending on the voltage scan rate.

Once the sample is immersed in the corrosive medium, oxidation and reduction reactions take place and create corrosion potential relative to the reference electrode. In this stage the current in both oxidation and reduction is equal in magnitude and cannot be measured as a net current flow. In the potentiodynamic polarization method, a series of different potentials are applied to the system and the resultant net current is measured. As the electrochemical potential increases from negative to positive, and eventually becomes higher than the corrosion potential, the anodic current becomes predominant and the cathodic current becomes negligible. If the specimen is polarized in the negative direction the cathodic current predominates, in which case the process would be referred to as

cathodic potentiodynamic polarization. Important information, such as the ability of the material towards immediate passivation in a particular medium, and the specific potential at which this occurs, can be obtained from the potentiodynamic polarization curve. Such plots are also extensively used to predict the rate of corrosion in the passive region[54,55].

2.4.3. Potentiostatic Polarization

Potentiostatic techniques consist of maintaining a constant potential at the interface of the test material and the electrolyte, and the associated measurement of the resultant current as a function of time. The passivation and re-passivation potentials, along with the cathodic and anodic protection of the metal based composites, can then be calculated using the diffusion coefficient of the surface, which is measured through performing a potentiostatic polarization test[56].

In order to perform a potentiostatic electrochemical measurement, first an initial potential is introduced to the system. Once the system is stabilised at the initial potential, the final programmed potential is applied and maintained unchanged for a specific period of time. The interpretation of the potentiostatic plots is a somewhat subjective subject, and can be done in a variety of ways depending on the physical and chemical characteristics of the composite material at the initial and final potentials. The rate of passivation can be directly related to the time that is taken in order to maintain a low and steady current flow (Figure 5) [57,58].

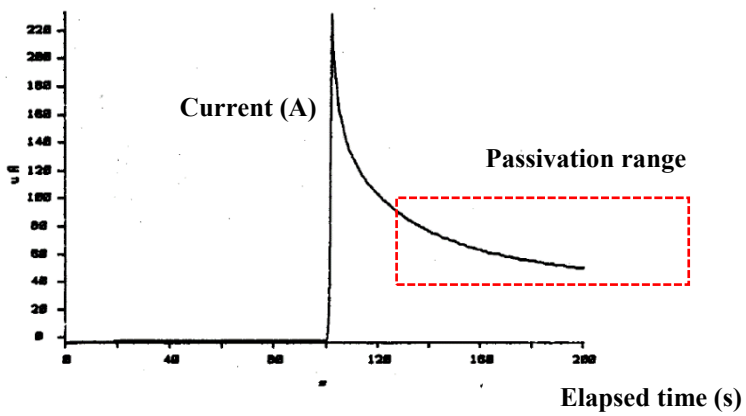

Figure 5. Passivation slope on a typical potentiostatic polarization plot.

In the corrosion assessment of cermet materials, pits are formed at an initial potential, and are able to re-passivate within a specific potential range. Performing a series of experiments at different potentials, can therefore be used to determine the re-passivation potential ranges for a specific material[59].

2.4.4. Cyclic Polarization

Cyclic polarization is a variant of the potentiodynamic polarization technique, and it is widely used to determine the tendency of specific materials towards pitting corrosion. Since pitting corrosion is one of the most common types of corrosion in cermet materials, performing cyclic polarization can therefore be used to assess the pitting tendencies of the manufactured composition.

In the cyclic polarization method, the OCP is scanned, starting at the corrosion potential, which is a result of pit initiation at the surface of the material. The potential is increased in positive direction (anodic) up to the point a specific current density is reached (set by the user). Once the maximum current density is reached, the experiment is programmed to change the current in the opposite direction, at which point the scanning procedure

continues in negative (cathodic) direction. The data obtained from this method can be plotted as applied potential versus the logarithm of measured current.

While pitting occurs at pitting potential/critical potential (E_{pit}/E_{crit}), (where current experiences a sharp increase due to the formation of pits), in a scan in the positive direction, the reverse scan traces a hysteresis loop, which closes at the protection or passivation potential (E_{pass}). The net current at this point is zero and, in the case of difficulty at finding the closing point, the passivation potential can be calculated by performing extrapolation to zero current in the reverse scan. If the passivation and the corrosion potential have the same value, or the protection potential is more negative, the likelihood of pit formation becomes higher[38,60]. On the other hand, a more positive protection potential decreases the tendency of the material towards the formation of pits. It is important to know that this method can also be used for predicting the occurrence crevice corrosion. At potentials between the pitting and protection potential, crevice corrosion will propagate further but new corrosion sites will not form. A hypothetical plot of cyclic polarization is shown in Figure 6.

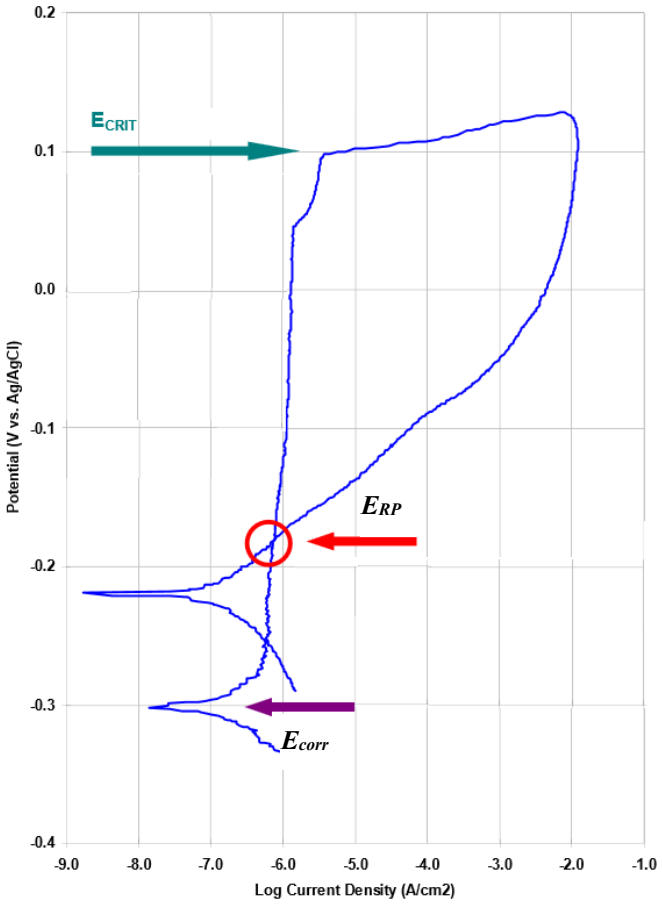

Figure 6. Representative cyclic polarization plot.

Moreover, the size and shape of the cyclic polarization loop can be used to interpret the resultant data. For example, if the reverse current has a higher value than the current in forward direction, the formation of a bigger hysteresis loop will lead to a higher tendency of the material to form pits[61].

Although the cyclic polarization method is strongly suited for the characterization of pitting corrosion, there are some drawbacks to this approach. The most common problem with this type of test arises when a long period of time is allowed for the propagation of the pit before reversing the scan direction. This can alter the re-passivation response of

the surface by changing the chemistry and depth of the pit, due to the change in protection potential in the opposite direction. To avoid this problem the protection potential can be measured after minimal pit growth[62].

2.4.5. Polarization Resistance

Polarization resistance (sometimes referred to as linear polarization resistance (LPR)), is an electrochemical test method that measures the resistance of the specimen to oxidation in a corrosive environment while an external potential is applied to the system. Polarization resistance (R), can then be monitored, and directly related to the rate of corrosion[55].

In order to perform an experiment for monitoring the polarization resistance, an electrode needs to be polarized within the range 10 to 30 mV, relative to the corrosion potential at steady state, to ensure that active corrosion is occurring during the measurements[63]. Then the polarization resistance can be specified by determining the slope of the linear region of the resulting curve at the corrosion potential. The relationship between change in potential and resulting polarization current R_P, is given by Equation 18[64,37]:

$$\frac{\Delta E}{\Delta i} = R_P = \left(\frac{\beta_a \beta_c}{2.3(i_{corr})(\beta_a + \beta_c)}\right), \qquad \textbf{Equation 18}$$

where, i is the current density, i_{corr} is the corrosion current density, E is the applied voltage, and β_a and β_c are the anodic and cathodic Tafel slopes, respectively. It should be noted that Equation 18 can be derived to calculate the i_{corr}. Once the corrosion current is known, the rate of corrosion can be determined from Equation 19:

$$corrosion\ rate\ (MPY) = \left(\frac{0.13\ i_{corr}\ (EW)}{A.d}\right), \qquad \textbf{Equation 19}$$

Where, EW is the equivalent weight in g, A is the exposed area in cm^2, d is the density of the specific test subject, and 0.13 is the metric time conversion factor. The rate of corrosion is measured in units of millimetre per year. In order to undertake these tests, a suitable potentiostat instrument is used to make the necessary scans and measurements for the polarization resistance, because of its ability to ramp the applied potential during the test while simultaneously measuring the resulting current.

2.4.6. Electrochemical Impedance Spectroscopy

One of the most popular electrochemical testing methods, which is widely used to monitor the corrosion behavior in various materials, is electrochemical impedance spectroscopy (EIS); this technique is also sometimes known as the alternating current method. This method uses an alternating current (AC) source to polarise the working electrode. Based on Faraday's law, the change in mass per unit area can be related to the current flow within the system. This can be performed through provision of an external power source to the system, which can either be an AC or direct current (DC) source. Sometimes an external signal can significantly affect the accuracy of the results, due to their ability of changing the properties of the system.

The DC-based techniques have been widely used for corrosion rate measurements, but the method generally requires a relatively large perturbation (or polarization) signal, which can negatively affect the test if the conductivity of the medium is very low. However, AC methods are more successful in performing such measurements, and are used extensively in various electrochemical research fields. In the AC-based methods, the amount of perturbation is very small and does not result in a change of the properties of the working

electrode. Therefore, it is relatively easy to perform the test in electrolyte mediums with low conductivity, similar to real life corrosive media such as sea water[65,66].

In this technique, a sinusoidal potential with a small amplitude is applied to the working electrode at a number of discrete frequencies, f (with units of Hz). Then the angular velocity, ω, can be found that arises from a certain frequency, following:

$$\omega = 2\pi f \qquad \textbf{Equation 20}$$

The resulting current waveform will exhibit a sinusoidal response that is out of phase with the applied potential signal by an angle of (Φ), and has a current amplitude that is inversely proportional to the impedance of the interface. The proportionality factor, $Z(\omega)$, is a transfer function that relates the excitation voltage, V, at various times across the circuit, and the current response of the system, i, as shown in Equation 21[57,65,67]:

$$Z(\omega) = V(\omega)/i(\omega) \qquad \textbf{Equation 21}$$

The system calculates the value of the V and i at each certain point of time by applying a set of complex mathematical relationships to their initial values. These relationships are beyond the scope of this thesis, and can be found in a selection of mathematics and electrochemical literature.

In the standard method of measurement for EIS tests, an AC signal of 1 to 10 mV is applied to the electrochemical cell. It is important to know that the EIS spectrum measurement takes a long time, and the system has to be kept under steady state conditions throughout the whole practice to avoid or minimise any associated errors. Other factors that can adversely affect the results of the test can include absorption of solution impurities, growth of an oxide layer, build-up of reaction products in the electrolyte solution, coating degradation, and unpredicted temperature changes[68]. Figure 7

illustrates an example of a simple electrochemical spectrometer connected to analysing software, made by Novo Control Technology[69].

Figure 7. Electrochemical impedance spectrometer.

2.4.7. Tafel Plots

Constructing Tafel plots is one of the most common methods in identifying the rate of corrosion in various materials. Tafel plots are used for measuring the corrosion current, i_{corr}, so the corrosion rate can be calculated. These types of plots can also help to calculate the rate of corrosion by relating the cathodic and anodic Tafel constants with the polarization resistance, R_p (Equation 18 and Equation 19).

To generate a Tafel plot, typically a scan starting at E_{corr} is performed, while moving toward either a more negative or positive potential, for a cathodic or an anodic scan, respectively. Both of these scans can also be done on the same plot by starting at

potentials more negative to E_{corr}, and then scanning up to more positive values. The rate of scan can be chosen according to available standards for specific materials, and the resulting plot creates a curve of applied potential versus the logarithm of the measured current density. The point of intersection at the corrosion potential can give the corrosion current of the specific material. Figure 8, illustrates a theoretical Tafel plot in both anodic and cathodic directions[70].

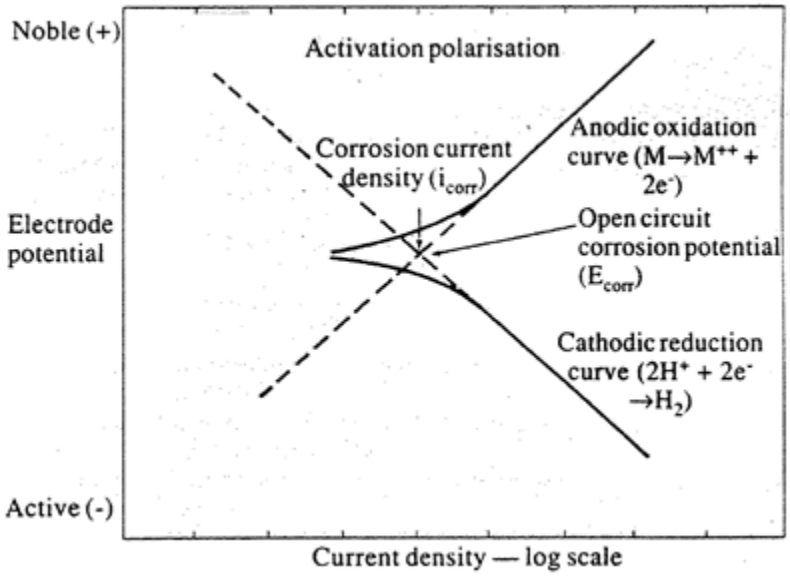

Figure 8. Theoretical Tafel plot and best fit straight lines in anodic and cathodic direction[56].

For the single scans of the cathodic and anodic Tafel regions, the two straight, tangential line extrapolations intersect at the corrosion potential (shown as dashed lines in Figure 8). In the case of more complex corrosion mechanisms, in which cathodic and anodic reactions are not consistent with a simple model, the corrosion current can be obtained by using the most linear region of the Tafel plot for extrapolation.

2.4.8. Erosion Corrosion Test

In order to conduct an electrochemical analysis experiment in parallel with the effects of erosion, during the corrosive reaction cylindrical samples are used, which are fixated into a rotating disk. The disk then rotates at a specific speed, with a known concentration and average grain size of inclusions (i.e. the erodent particles) in an aqueous environment, such as salt water. Each sample is required to be electrically isolated from the disk and the samples are connected to a potentiostat for electrochemical measurements through a Hg cup. The total material loss due to the erosion and corrosion of the specimens is then calculated by weighing the samples before and after the tests. Furthermore, the electrochemical measurements are conducted both during and after rotation[71].

In a study performed on the corrosion response of nano-particle-reinforced Ni-Cr-Mo-Cu alloying layers, in aqueous solutions of different flow rate environments, the effects of flow velocity and the type of eroding particles has been found to be extremely significant. The results of polarization curve measurements obtained under slurry flow conditions has shown an increase in corrosion current density and a decrease in corrosion potential compared to the tests performed under static state conditions[72].

2.4.9. Non Electrochemical Methods (Cumulative Mass Loss)

Gravimetric determination of mass loss is one of the more traditional ways to determine the rate of corrosion over a specific period of time. This method simply measures the mass of a specific material before and after the natural or accelerated corrosion process. The test subject can be exposed to a corrosive environment by different methods such as salt spray, Q-fog, etc., to introduce several weathering phases[25,35]. One of the advantages of the mass loss determination of the corrosion rate, when compared to the

electrochemical methods, is in weathering. In the field many of materials are constantly subjected to cycled wet and dry environments over time, and typical electrochemical methods are not suitable for measuring the corrosion rate in these types of applications. In order to minimize experimental errors there are many standards and procedural factors, such as post exposure cleaning and surface finish that need to be considered when conducting these types of evaluation. The average corrosion rate can be calculated using the standard relationship between mass loss and the exposed surface area, over a specific period of time, following:

$$\text{Average rate of corrosion} = \frac{KW}{AT\rho}, \qquad \textbf{Equation 22}$$

where K is a constant, and various values of K (mass-loss rate in different units) can be produced, T is the time of exposure (in hours), A is the area (in cm^2), ρ is the density of test subject (in g/cm^3), and W is the measured mass loss (in grams)[25].The rate of corrosion is invariably not constant during the entire time of exposure, and measurements at unit time periods can be used to access the relative rate of corrosion at different times, such as at the beginning or end of the assessment period[35].

2.5. Analysing the Results

Analysis of the microstructure of the specimens before and after performing corrosion tests, along with associated chemical analyses, have a significant benefit in terms of characterising the corrosion behavior of different materials. In this section the methods of chemical and microstructural analysis are briefly explained.

2.5.1. Microstructural Analyses

Microstructural analysis is widely conducted to evaluate the surface of the corroded samples. Methods such as scanning electron microscopy (SEM), energy dispersive X-ray spectroscopy (EDS) and X-ray diffraction (XRD) are used to determine the size and nature of the grains in the material, and the effect of the corrosive environment on the material. Investigating the microstructure of the test specimens before and after the corrosion testing confirms important information such as the initial grain size, distribution of chemical elements within the structure, and the formation of possible phases due to the chemical corrosion reactions.

Figure 9 shows micrographs obtained from the surface of a WC-CrNi cermet coating composition both prior to and after anodic polarization at 50°C in artificial seawater. According to the results of this microstructural analysis, localised corrosion attack has targeted elongated 'stringers' (an artefact of the coating deposition process) and has resulted in the formation of deep crevices between phases[59].

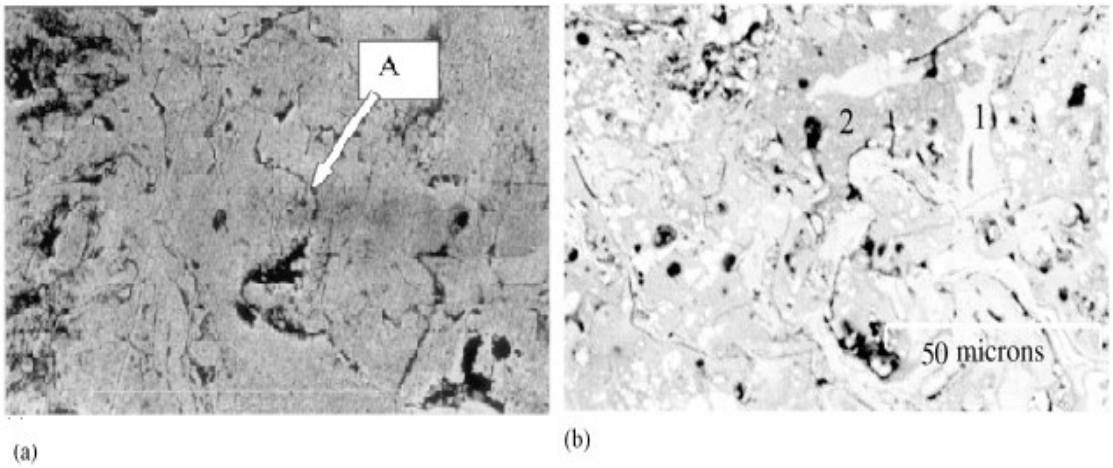

Figure 9. SEM images for a WC-CrNi cermet, (a) after and (b) before anodic polarization at 50°C in artificial seawater.

While SEM is known as one of the more useful techniques to study the effects of corrosion on microstructures of many materials, XRD is widely used for crystalline phase analyses of the starting powders, densified cermets and coatings, and potentially any corrosion induced oxides formed on the surface.

2.5.2. Chemical Analyses

The remaining solution of the electrolyte can be chemically analysed to confirm the composition and, nominally, the amount of the material loss from the tested samples. This test can ideally be performed using inductively coupled plasma optical emission spectroscopy (ICP-OES). In this method, it is preferable that the remaining electrolyte is first filtered to remove the fine particles. These fine particles are dried in the presence of raised temperatures and then weighed. Filtrated materials then are dissolved in acids such as HNO_3 and dried for the second time. The resultant material is then made into a solution of specific volume and used for ICP-OES analysis[73]. The filtered solutions, (after particulate material removal) can also be analysed using this approach. An inductively

coupled plasma is used to excite the atoms, which are able to emit electromagnetic radiation at specific wavelengths for a particular elemental species. The intensity of the resulted emission is related to the concentration of the corroded material within the remaining particles for a specific volume of recovered electrolyte.

The results of ICP-OES analysis can be used to gain an understanding of the relationship between the physical material variables such as the composition and the amount of material that has been lost to electrolyte during the controlled electrochemical reactions. For example some studies have reported an increase in the metallic phase lost with the amount of binder material in the composition, for example in cermets such as TiC with varying amounts of stainless steel (316L) binder. It was also shown that the amount of Ti that has been found from the results of ICP-OES analysis decreased with increasing binder content in the system (Figure 10)[74] .

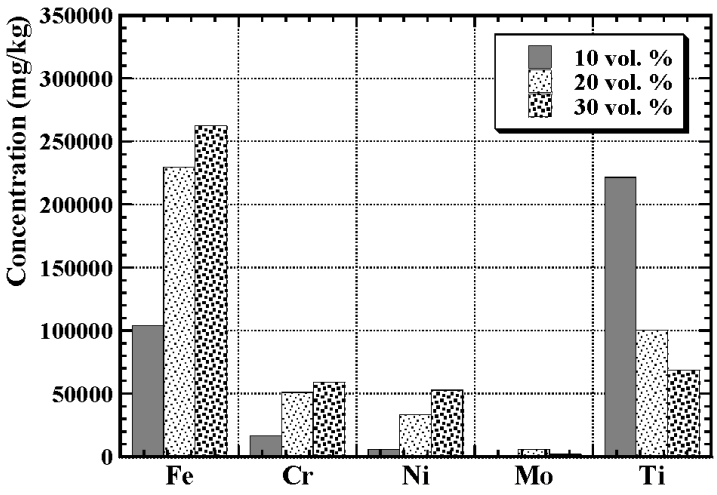

Figure 10. ICP-OES analyses of the post-test potentiodynamic polarization solutions of TiC-316L cermets[74].

2.6. Summary

This chapter has provided an introduction to electrochemical analysis methods that are widely used in evaluation of the corrosion of advanced materials. According to the reviewed literature, standard electrochemical test methods can be used to access the corrosion behavior of cermets, often with a few basic modifications. In order to obtain a better understanding of the complex corrosion mechanisms of composite materials, the nature of electrochemical reactions was discussed in detail. A number of different forms of corrosion was reviewed and appropriate calculations for each method was conferred. Characteristic analysis was reviewed in terms of approaches for microstructural and chemical examination of the compositions, both prior to and after corrosion tests.

Chapter 3. Manufacturing of TiC and Ti(C,N) Based Cermets

In the present study, the aqueous corrosion behavior of TiC and Ti(C,N) based cermet materials has been investigated, using a range of Ni_3Al-based intermetallic binders and various micron-sized carbonitride powders (TiC, $TiC_{0.7}N_{0.3}$, $TiC_{0.5}N_{0.5}$, and $TiC_{0.3}N_{0.7}$). Cermets were prepared using a reaction-sintering route, with 30 vol. % binder, achieving densities in excess of 99% of theoretical. Measurement of the open circuit potential was used to determine the equilibrium electrochemical potential. The potentiodynamic and cyclic polarization responses of the cermet materials have been determined, with Tafel extrapolation used to determine the rate of corrosion for each composition. Inductively coupled plasma optical emission spectrometry was then applied to analyse the post-test corrosion solutions, in order to determine elemental species liberated from the samples during corrosion testing. The effects of the corrosive environments were also assessed using scanning electron microscopy. It was demonstrated that selective attack of the binder occurs, and the extent of corrosion and primary mechanism depends on the Ni_3Al alloy composition.

WC-Co 'hard metals' which are widely used in a variety of industrial applications (some similar to those for TiC and TiCN based cermets), due to their resistance to abrasive wear, in addition to their high hardness and toughness. However, in contrast to their mechanical properties, the corrosion response of these materials is relatively poor. In the current work the corrosion mechanisms in two WC-Co cermets are analysed, with 10 and 30 vol. % of the Co metal binder, in a 3.5 wt.% NaCl aqueous solution as a baseline composition. The corrosion behavior of WC-Co was also assessed using a variety of electrochemical measurements. It was demonstrated that selective attack of the binder occurs, and the extent of corrosion and primary mechanism depends on the amount of

nitrogen in alloy composition, and the intermetallic binder composition and volume fraction. It is also shown that the present cermets exhibit corrosion rates as much as three orders of magnitude lower than WC-Co with identical binder contents. Details relating to the materials and methods that has been used for current study are provided in this chapter.

3.1. Materials

The materials that were employed in this study are discussed in detail through the following section. The cermet samples were processed by using a mixture of powdered ceramics TiC, $TiC_{0.7}N_{0.3}$, $TiC_{0.5}N_{0.5}$, and $TiC_{0.3}N_{0.}7$ and a blend of metallic Ni and Ni/Al. The characteristics of the intermetallic phase, such as oxidation/corrosion resistance, yield stress, etc., was altered by addition of Cr, B and/or Zr. The chemical and physical characteristics of each phase have been reviewed. Additionally, WC-Co cermets were used to perform a baseline comparison between the materials manufactured for the current study and commercially produced 'hardmetals' used for similar applications.

3.1.1. Metallic Phase (Ni_3Al)

Ni and Ni-based alloys have become more attractive to contemporary manufacturing due to their high capacity to tolerate a wide range of harsh operating conditions, such as corrosive environments. Pure Ni has a high toughness and ductility, in addition to its good corrosion resistance in normal atmosphere, aqueous solutions, a range of acids (de-aerated, non-oxidizing), and caustic alkalis. Ni is able to accommodate large amount of elements in solid solution such as Mo, Cr and W, and can be used in more severe environments when compared to more conventional alloys, such as stainless steels. The most common types of corrosion on Ni-based alloys are uniform corrosion, pitting and crevice corrosion, inter-granular corrosion, and galvanic corrosion[75].

Nickel aluminide (Ni_3Al) is an intermetallic alloy, comprised primarily of Ni and Al, with characteristics of both ceramics and metals. Ni_3Al can be an ordered alloy, which is formed between two metallic components, and is defined as an intermetallic compound. Such an atomic structure with two (or more) sub-lattices has the ability to reduce the diffusion and movement of dislocations which results in excellent elevated temperature properties in the final compound [76].

Due to its high thermal conductivity, use of Ni_3Al is the basic strengthening mechanism in high temperature nickel based super alloys. In addition, the relatively low density of this alloy, combined with its high temperature properties, makes it ideal for its use in special applications such as coating blades in gas turbines and jet engines[77].

For the current study, the stoichiometric Ni_3Al binder powder was obtained by mixing appropriate amounts of Ni powder (lot no. L10W013; 2.2-3.0 μm) and Ni/Al powder (lot no. D28X029; D_{50} = 38 μm), which were provided by Alfa Aesar (Ward Hill, MA, USA); the Ni/Al powder was a 50:50 wt.% mixture. IC221 and IC50 are newer variants of Ni_3Al based alloys that were developed to increase the ductility, strength and oxidation resistance of the alloy. Production of such alloys can be performed by controlled addition of boron, zirconium and chromium to base Ni_3Al metallic powder (both IC50 and IC221 are sub-stoichiometric in terms of Al content). The nominal composition of alloys that are used for presented study is given in Table 1.

Table 1. Nominal composition of elements for Ni_3Al, IC50 and IC221 metallic binders.

Binder ID	Elemental Composition (wt.%)				
	Ni	Al	B	Zr	Cr
Ni_3Al	86.72	13.28	-	-	-
IC50	88.08	11.3	0.02	0.6	-
IC221	81.98	8.5	0.02	1.7	7.8

IC50 was obtained by mixing B_4C powder (lot no. BC060F05 D_{50}=11.4 μm) which were provided by UK Abrasives Inc (Northbrook, IL, US) and Zr powder (lot no. Z005551P; D_{50}=0.04 μm) which were provided by Tosoh (Kaisei, Japan) with Ni powder (lot no. L10W013; 2.2-3.0 μm) and Ni/Al powder (lot no. D28X029; D_{50}=38 μm), which were provided by Alfa Aesar (Ward Hill, MA, USA). IC221 was obtained by mixing B_4C powder (lot no. BC060F05 D_{50}=11.4 μm) which were provided by UK Abrasives Inc (Northbrook, IL, US) and Zr powder (lot no. Z005551P; D_{50}=0.04 μm) which were provided by Tosoh (Kaisei, Japan) and Cr powder (lot no. I15U008; D50≤10 μm) which were provided by Alfa Aesar with Ni powder (lot no. L10W013; 2.2-3.0 μm) and Ni/Al powder (lot no. D28X029; D_{50}=38 μm), which were provided by Alfa Aesar (Ward Hill, MA, USA)

3.1.2. Ceramic Phase (TiC and Ti(C,N))

Titanium carbide (TiC) is a hard refractory ceramic with characteristics comparable to tungsten carbide (WC). TiC has a face centered cubic (FCC) crystal structure and the density of 4.93g/cm^3. TiC is frequently used in the production of cermet materials, which

are used for high speed cutting and machining steel. Furthermore, TiC based coatings are suitable in industrial applications that require advanced abrasion-resistant surfaces and heat shields [78]. For the present study the TiC powder (lot no. PL20125339; D_{50}=1.25 μm) was obtained from Pacific Particulate Materials (Vancouver, BC, Canada). The related $TiC_{0.7}C_{0.3}$ (lot no. L25809; D_{50} = 2.10 μm), $TiC_{0.5}N_{0.5}$ (lot no. L29865; D_{50} = 1.74 μm), and $TiC_{0.3}N_{0.7}$ (lot no. L25747; D_{50} = 1.72 μm) powders were obtained from Treibacher Industrie AG (Althofen, Austria).

3.1.3. WC-Co

The most common compositions of WC based 'hardmetals' are formed via liquid sintering with Co as the binder phase. High corrosion and erosion resistance of 'hardmetals' based on WC and Co, has extended the use of this type of cermet in many areas such as thermal spray coatings. The increased demand has been followed by many studies on methods of manufacturing and improvement of WC-Co cermets. As the name implies, WC-Co 'hardmetals' are composed of hard WC grains imbedded in a Co metal matrix[79]. The crystalline structure of WC is known to be hexagonal (α-WC) or cubic (β-WC), with the latter preferred for higher temperatures[80]. In the hexagonal lattice, metal atoms are layered over one another, with carbon atoms filling the gaps between the layers and providing both tungsten and carbon a regular trigonal prismatic arrangement[81].WC has an approximate Young's modulus of 550 GPa[70] and a Vickers hardness value in range of 1700-2400HV[82,83]. The metallic phase (Co) has crystalline structure of HCP at room temperature and FCC at elevated temperature, with transition at 450°C[84,85]. Co has a Young's modulus of 209 GPa and a Vickers hardness value of 106.04 HV[86].

The mechanical and electrochemical properties of WC-Co cermets are affected by the amount and composition of the binder, carbide grain size, method of manufacture and in case of thermal spray coatings, the method of application. For the purpose of the current study, WC-Co (6 wt.%) (part no. ZM6; mean grain size ~3.5-5μm) and WC-Co (18 wt.%) (part no. ZM18; mean grain size ~3.5-5μm) samples were provided by Ultra-met (Urbana, OH, US). Square section cutting insert blanks, with an area of 2.65 cm^2 and height of 0.7 mm, were manufactured through hot isotactic pressing and achieved full density. Newer grades of WC-Co can contain additional alloying elements for various purposes. For example, extremely fine grains can be produced by addition of Cr to the binder, which is a significant factor in controlling the mechanical and electrochemical behavior of the work piece[27,87].

3.2. Methods

The experimental procedure that has been followed to prepare and examine the cermet samples for the present study are outlined in detail in this section.

3.2.1. Sample Preparation and Basic Characterization

Cermet samples were prepared by mixing the powdered ceramic, with composition of $TiC_{1-x}N_x$ (where $0<x<1$), and the associated metallic binder constituents (for Ni_3Al, IC50 and IC221 compositions). A polymeric binder (0.5 wt.% polyvinyl butyral (PVB) resin) was added to all of the compositions in order to increase the green strength of the pressed samples. Each compositional was then ball-milled with yttria stabilized zirconia media in acetone for 24 hours, followed by a 24 hour drying period to remove the solvent through evaporation. The dried powder mixtures then were sieved through a 75 μm mesh, and

pressed uniaxially (45 MPa) into pucks of 32 mm in diameter and 6 mm in thickness. The pellets were then vacuum bagged and cold isostatically pressed (CIPed) at 207 MPa for further compaction of the samples before sintering. Cermet samples were then placed in alumina crucibles, on top of bubble alumina and sintered under dynamic vacuum of approximately 20 mTorr at 1550˚C for 1 hour. The heating rate of 10C°/min and cooling rate of 25°C/min (down to the room temperature) was programmed for furnace conditions.

Single-phase ceramic and metallic powders were also sintered individually into disks of 40 mm in diameter and ~8 mm in thickness, using spark plasma sintering (SPS), at a pressure of 50 MPa under vacuum. Powdered ceramic with composition of $TiC_{1-x}N_x$ was sintered at 1800˚C and 50 MPa for 10 minutes, with the exception of TiC powder which was sintered at 1650˚C for 5 minutes. The Ni_3Al binder powder was sintered at 1200˚C for 5 minutes. Surface preparation was performed by subsequent sequential diamond grinding and polishing, starting with 160 μm diamond impregnated resin pads and finishing with 0.25 μm diamond paste. The density of each sample was calculated using Archimedes' principle and compared to theoretical density of the mixture.

Equivalent weight (EW) for the alloys, and penetration rates from electrochemical measurements, have been used to obtain corrosion rates for all of the compositions[88]. In the present study, calculations of EW values were performed by careful observation of each constituent element’s behavior (number of valence electron, possible galvanic relationships between elements, passivity, etc.), during the electrochemical reactions.

3.2.2. Microstructural and Chemical Analysis

The microstructures of the materials were evaluated using scanning electron microscopy (SEM) (Model S-4700, Hitachi High Technologies, Tokyo, Japan), with associated compositional analysis performed in the SEM using energy dispersive X-ray spectroscopy (EDS; Inca X-maxN, Oxford Instruments, Concord, MA, USA). The results of microstructural analyses were used to observe the sintering response of the prepared samples. The lineal incept method was conducted to determine the average grain size for a minimum of 300 grains[89]. SEM and EDS analysis were performed on both pre- and post-electrochemical tested surfaces, to study the corrosion response of the various materials.

3.2.3. Electrochemical Analysis

Electrochemical measurements were performed at room temperature (21 ± 2ºC), with a relative humidity of 40-55%, using a potentiostat/galvanostat (EG&G Model 273A, Princeton Applied Research, TN, USA) and frequency response analyzer (Model 1250, Solartron Schlumberger, TX, USA). The corrosion tests were performed in a three-electrode flat cell (Model K0235, Princeton Applied Research, Mississauga, ON, Canada), with the test samples acting as the working electrode, platinum mesh (Pt) as a counter electrode, and a saturated calomel electrode (SCE = SHE – 241 mV) as the reference electrode. All the potentials are subsequently reported as SCE. The electrolyte was prepared using 3.5 wt. % NaCl in distilled, de-aerated water at room temperature (21 ± 2ºC). The test surface area at the working electrode was 1.0 cm^2. In case of the cermet structures the volume fraction of the metallic binder (active corroding material), was used as the area for corrosion calculations.

Samples were stabilised in the electrolyte for a period of 2 hours and then the open circuit potential (OCP) was recorded. Potentiodynamic tests were performed to polarise the surface of the specimen, with the potential varied from -1.0 V to +1.0 V, with respect to the reference electrode. A potential scan rate of 0.1667 mV/s was used for all tests. Tafel extrapolation has been used to determine the corrosion potential, E_{corr}, and the corrosion current, i_{corr}. The ASTM standard method for potentiodynamic polarization resistance measurements, and the subsequent calculation of corrosion rates (Equation 23), was followed[55,37]:

$$CR = K\frac{i_{\text{corr}}}{\rho}EW \qquad \textbf{Equation 23}$$

where CR is the rate of corrosion (given in mm/year), i_{corr} is the current density at the corrosion potential (in A/cm^2), K is a constant (equal to 3.27×10^{-3} mm g/μA cm yr), ρ is the density (in g/cm^3) and EW is the equivalent weight for the specific composition. Each composition was tested for an average of 3 or 4 different samples, for each of the compositions, to ensure the reproducibility of the results. Cyclic electrochemical analysis was also performed for each composition, polarising the surfaces with initial voltage of -1.0 V to +1.0 V, and then cycling back to -1.0 V as the final potential, with respect to the SCE reference. Post corrosion surfaces were examined for microstructural and compositional changes using SEM and EDS. The post corrosion electrolyte was collected for inductively coupled plasma atomic emission spectroscopy (ICP-OES; Model Varian Vista Pro, CA, USA) with internal calibration standard (Scandium) on the third peristaltic pump channel. pH was measured using a portable pH meter (Metrohm Herisau portable pH meter Model E488, Metrohm A GIonenstrasse Herisau, Switzerland). The pH meter

was initially calibrated using Fisher Buffer Solutions, for pH values of 4, 7 and 10. Then samples were filtered using a Millipore Apparatus on a proweigh filter (pore size 1.5μm) and solids were separated.

The solids on the filters were then dried using a Fisher Isotemp oven at a temperature of 105°C. After the solids were dried and cool they were then weighed in order to obtain the amount of solids in each samples. The obtained solids were then digested by a Near Total Acid Leach Digest procedure, which consisted of 4 different acids (HF, HNO_3, $HClO_4$, and HCl). The resulting solution from the solids and filtrate were then analysed by inductively coupled plasma optical emission spectroscopy (ICP-OES; Model Varian Vista Pro, CA, USA) to obtain the chemical composition.

3.3. Results and Discussion

The sintered cermet compositions all achieved a minimum of 98% of their theoretical density, regardless of the ceramic composition (C:N ratio). According to microstructural analyses on the polished surfaces, the size and morphology of carbide grains were significantly changed once nitrogen was introduced into the ceramic phase composition. The results of grain size analysis have shown that the most significant values for the grain size reduction has been achieved by cermet with a C:N ratio of 0.5:0.5 in the ceramic composition. An average grain size of ~5.5 μm was determined for the TiC-Ni_3Al (30 vol.%) composition, while the average grain size for $TiC_{0.5}N_{0.5}$-Ni_3Al (30 vol.%) was found to be ~2.65 μm^{90}. Broadly similar results were obtained when the Ni_3Al alloy composition was altered to either IC221 or IC50 (again for 30 vol.% metallic binder), with relatively close values for the two types of compositions (Figure 11). The average grain size for the IC221 and IC50 binders, with TiC ceramic phase, was found to be ~7.2

to ~7.4 μm, respectively, while the $TiC_{0.7}N_{0.3}$-based cermets achieved average grain size of ~2.8 to ~2.9μm. This result was largely anticipated, based on the knowledge that the presence of N in a TiC-based system results in refinement of the overall microstructure by decreasing the relative associated surface energy[91].

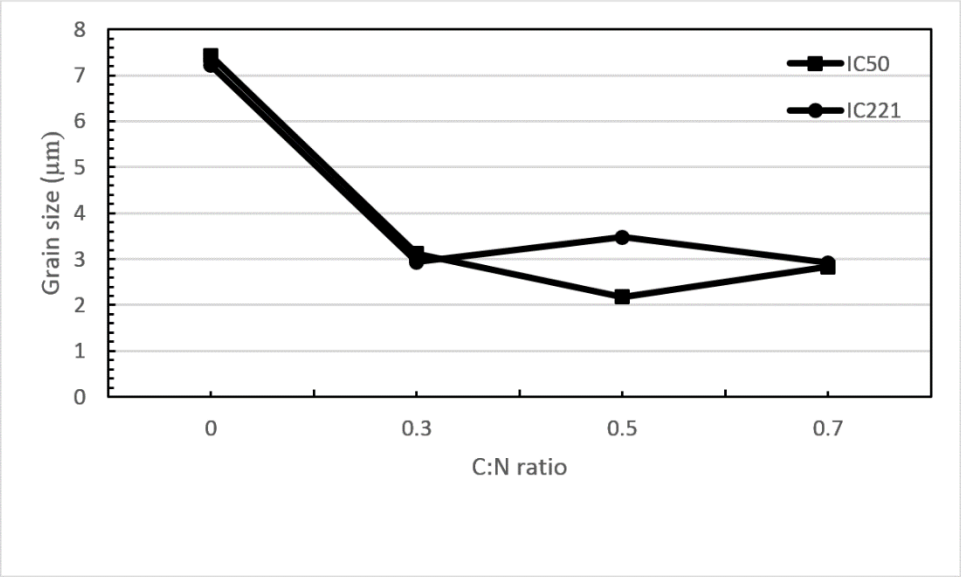

Figure 11. The observed decrease in grain sizes in Ti(C,N)-IC50 and Ti(C,N)-IC221 cermets through the addition of N to the ceramic phase.

On the other hand, the changes in grain size relative to the volume fraction of the Ni_3Al binder has been found to be negligible[92]. However, the oxidation properties of Ni_3Al-based alloys can be improved by decreasing the grain size, which allows continuous formation of α-Al_2O_3-based protective scales on Ni_3Al[93–95]. Some studies have also suggested that the amount of N in the carbonitride phase also effects the size and formation of the core rim structure in the reverse order[91]. In the current study core rim structure was observed in the TiC-Ni_3Al cermet composition (Figure 12), while homogenous carbonitride grains were seen in the Ti(C,N)-Ni_3Al compositions.

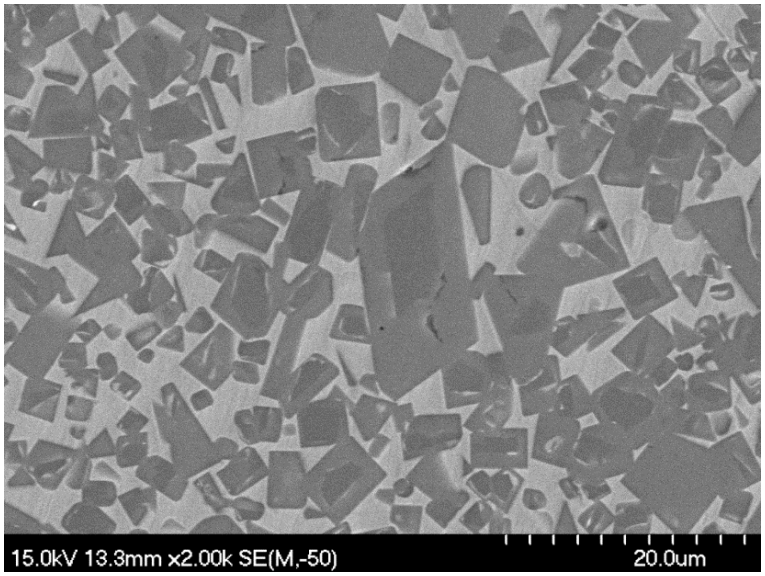

Figure 12. An SEM image of the core rim structure formed in the TiC-Ni_3Al (30 vol.%) cermets.

From the results of EDS analysis, and close comparison of ceramic phases with 0.3, 0.5 and 0.7 C:N ratio, it is concluded that the formation of core rim is related to presence of impurities, in particular W, in the TiC powder (Figure 13).

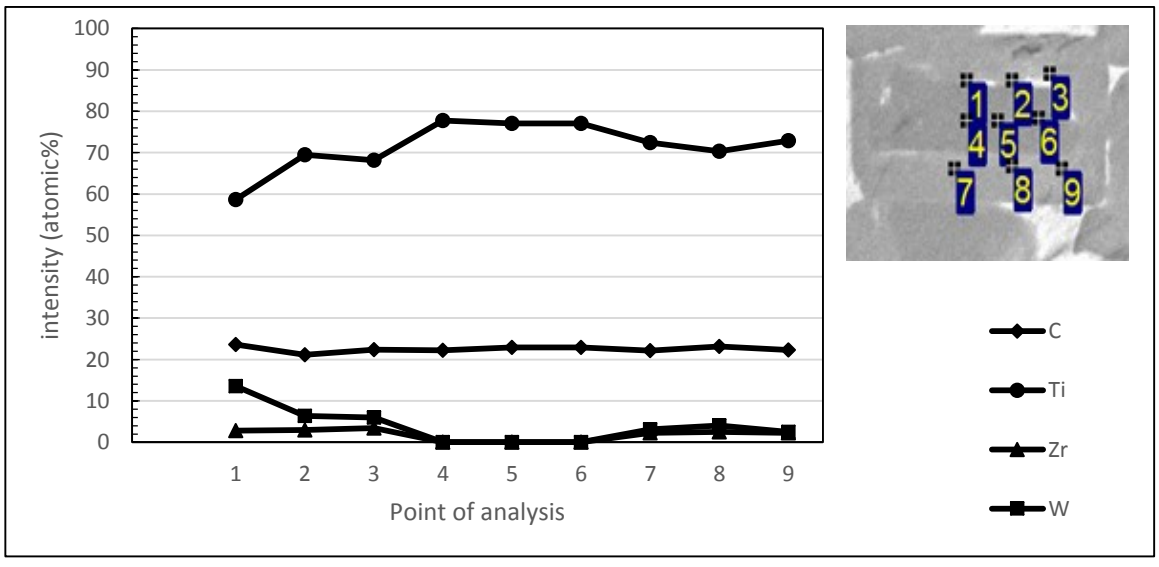

Figure 13. EDS analysis, presence of Zr and W, in composition of rim

Micrographs from the cermet compositions with IC50 and IC221 as the metallic binder both have confirmed the formation of core rim within the carbonitride grains, for all of

the Ti(C,N) ceramic phases. It was observed that addition of a small amount of N to the ceramic phase has resulted in a significant reduction in the generation of surface defects during grinding/polishing, through refinement of the carbonitride grain size. Slight changes in the structure of core rim were also observed. Contrary to the case with stoichiometric Ni_3Al, it was observed that IC50 and IC221 based cermets, with N in their ceramic phase, have formed core rim with significantly lower compositional changes at the core and rim interphase when compared to the TiC based cermets, with W rich zones (Figure 14).

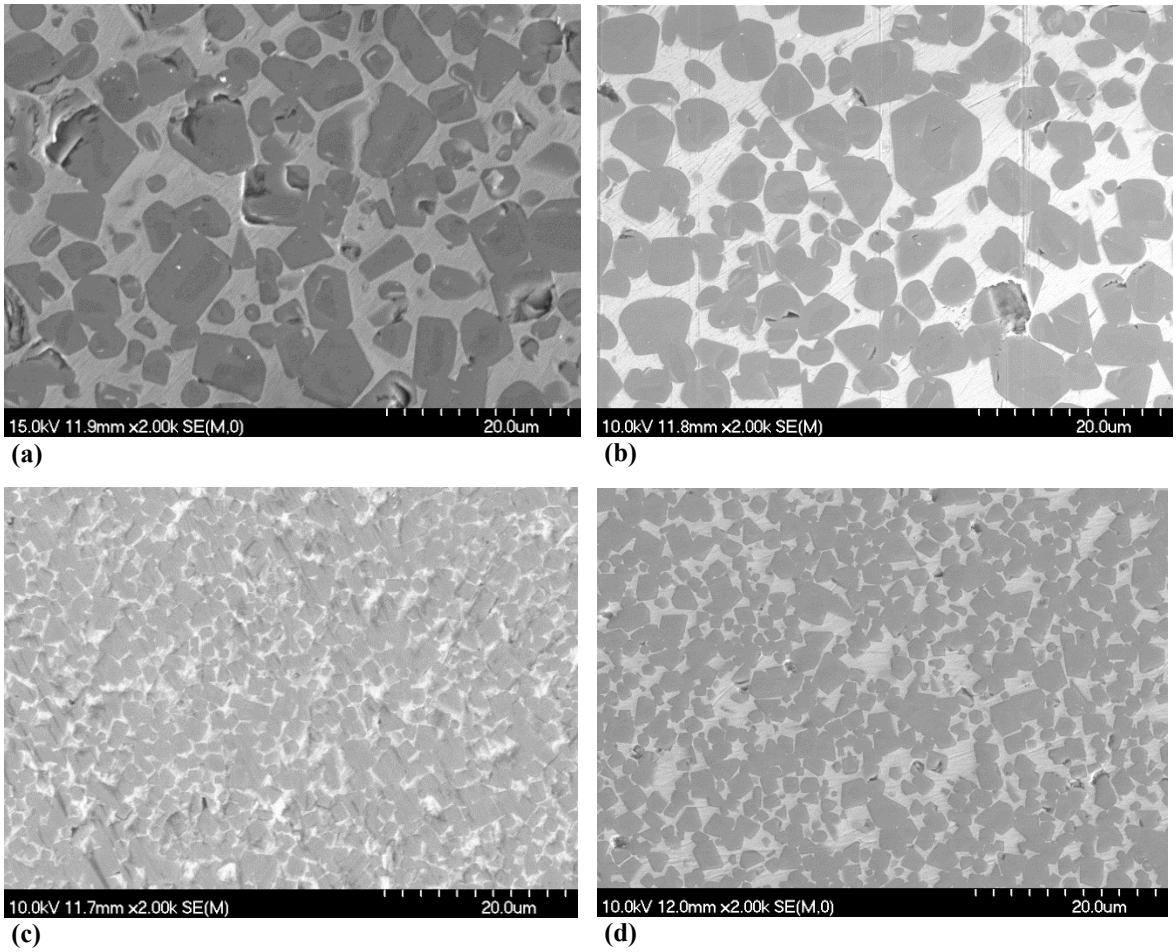

Figure 14. SEM images of the sintered cermets with 30 vol.% binder: (a) TiC-IC50, (b) TiC-IC221, (c) $TiC_{0.7}N_{0.3}$-IC50, and (d) $TiC_{0.7}N_{0.3}$-IC221.

In terms of the SPS-processed materials, single phase Ti(C,N) samples, typically exhibited densities in excess of 98% of theoretical, with the exception of $TiC_{0.7}N_{0.3}$, which only reached ~94% of its theoretical density. SEM and EDS analysis have shown that the TiC 'single-phase' samples have formed W rich zones, effectively at the grain boundaries of the TiC grain structure during SPS (Figure 15).

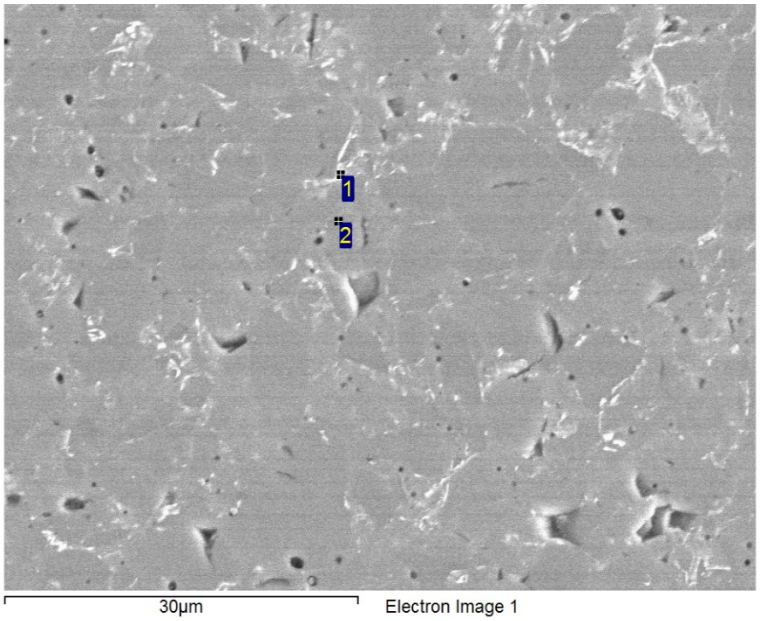

ID	Element (wt%)		
	C	Ti	W
1	9.55	6.94	3.51
2	1.60	8.40	-

Figure 15. SEM and EDS analysis on single phase TiC sample, 1. W rich zones 2.TiC grain

The Ti(C,N) samples, processed in the absence of a Ni_3Al-based binder, have shown a uniform surface composition, with the existence of residual pores that were not fully removed during the SPS sintering cycle (Figure 16).

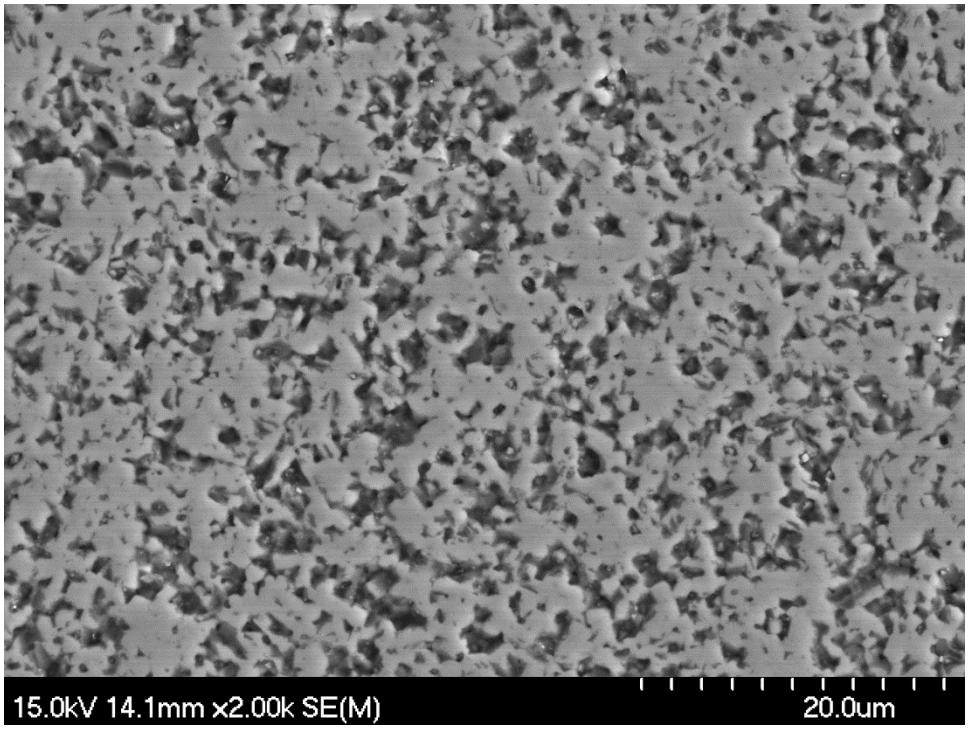

Figure 16. Typical SEM example of the microstructure of a polished surface of $TiC_{0.5}N_{0.5}$ single-phase ceramic, sintered using the SPS method.

In contrast to the ceramic phases, the single-phase stoichiometric Ni_3Al intermetallic binder has only achieved ~78% of theoretical density after SPS processing. This is likely related to the coarse particle size and high yield stress of the Ni_3Al alloy. Higher densities for SPS-processed intermetallic Ni_3Al phase has been achieved by increasing the sintering time to 10 minutes, at 950˚C, and applying a higher pressure of 65MPa for nanocrystalline Ni_3Al [93].

Chapter 4. The Effects of C:N Ratio on the Aqueous Corrosion Response of TiC and Ti(C,N) Cermets with an Ni_3Al-based Binder

Zhila Memarrashidi and Kevin P. Plucknett

Materials Engineering Program, Department of Process Engineering and Applied Science, Dalhousie University, 1360 Barrington Street, Halifax, Nova Scotia, CANADA

Abstract

The aqueous corrosion behavior of TiC and Ti(C,N) based cermet materials has been investigated, using stoichiometric Ni_3Al intermetallic as the binder phase. Cermets were prepared using a reaction-sintering route, with 30 vol.% binder, achieving densities in excess of 98 % of theoretical. Single-phase TiC, Ti(C,N), and Ni_3Al have also been prepared using spark plasma sintering (SPS), to analyze the electrochemical characteristics of the parent components. The potentiodynamic and cyclic polarization responses of the cermet and single-phase materials have been determined, with Tafel extrapolation used to estimate the rate of corrosion. Post-test corrosion solutions were analyzed using inductively coupled plasma optical emission spectrometry, to determine elemental species liberated from the samples, scanning electron microscopy and associated energy dispersive X-ray analysis. Selective attack of the binder occurs, while the extent of corrosion and primary operative mechanism depends on the C:N ratio in the Ti(C,N). Commercially obtained WC-Co cermets, with ~30 vol% binder, have also been tested for comparative purposes.

Keywords: Galvanic corrosion, open circuit potential, potentiodynamic polarization, cyclic polarization, scanning electron microscopy, ICP-OES, spark plasma sintering

4.1. Introduction

Cermets combine the desirable properties of both the ceramic and metal phases on a micro scale. The resulting product is relatively lightweight, with densities typically ranging from 6 to 7.5 g/cm^3, compared to conventional 'hardmetals' (12 to 15 g/cm^3). Cermets also invariably exhibit high mechanical strength, fracture toughness and thermal conductivity[96,32]. Tungsten carbide 'hardmetals' with Co- or Ni-based metal matrices (WC-Co and WC-Ni, respectively) have traditionally been used for application in a wide range of harsh environments[32]. However, limitations such as high density, and poor oxidation and corrosion resistance have drawn attention towards titanium carbide (TiC) and titanium carbonitride (Ti(C,N)) based cermets. As with WC, typical metallic binders for these type of cermets are Ni and, to a lesser extent, Co[16]. More recently, ductile nickel aluminides, particularly alloys based on Ni_3Al, and stainless steel binders have also been investigated[17–19].

Factors such as the volume fraction of metallic binder, microstructural parameters (i.e. grain size, contiguity and binder mean free path), and the chemical compositions of the ceramic and metallic phases all effect the properties of the composite, including strength, hardness, oxidation/corrosion resistance and wear behavior. The effects of chemical composition on the mechanical properties of Ti(C/N) based cermets have been widely studied[17,32,45,97]. However, the number of investigations performed on the corrosion mechanism(s) of these materials is comparatively limited.

Information available on electrochemical measurements and data interpretation for WC-based hardmetals can be used as an initial baseline for corrosion analysis of alternate cermet systems. Moderately extensive analyses of WC-Co materials have been undertaken, for example investigating the effects of electrolyte composition [10,97–99], and

the actual hardmetal composition[12,99–101], on the corrosion response. In addition, the corrosion response of WC-based coatings has also been undertaken[102,103]. Hochstrasser-Kurz and colleagues have employed a variety of analytical techniques to assess the aqueous corrosion response of WC-Co hardmetals[11,13]. It is generally noted that selective attack of the Co-based binder occurs in this materials, particularly at low pH values. However, at more alkaline pH, attack on the WC becomes more apparent[11]. The incorporation of W and C into the Co-based binder was also noted to improve the corrosion resistance[11].

In particular, the presence of binders such as Co, Cr or Ni can have significant effects on improving the corrosion properties of these materials, which are often applied as coatings, by eliminating micro-cracks, which are the major infiltration paths for corrosive solutions[20,21]. Micro galvanic corrosion at the metallic/ceramic interphase (which is a typical form of corrosion for multiphase materials with different oxidation characteristics) can potentially be minimized or eliminated by modifications applied to both phases. For example, Cr has been suggested in many cases due to its ability to form a stable oxide layer and suppress the dissolution of the binder[22,23]. Typically, corrosion events in cermets begin with the formation of pits, followed by galvanic corrosion at the ceramic/metallic interphase, in the instance of different chemistries and corrosion potentials. Dissolution of the binder during galvanic attack then leads to formation of crevices and, finally removal of the carbide grains[7,8].

In the current study, TiC and Ti(C,N) based cermet samples have been prepared with a stoichiometric Ni_3Al metallic phase (at a fixed content of 30 vol.%), and sintered using a simple *in-situ* reaction sintering approach[24]. The single-phase ceramic and metallic cermet constituents were also prepared individually using spark plasma sintering (SPS).

Various C:N ratios were examined, from 100:0 through to 30:70; high N contents in the Ti(C,N) retard densification, limiting the compositions that can be processed using this approach[104]. The influence of composition on the electrochemical behavior of each material was then assessed, using a variety of methods, including potentiodynamic and cyclic polarization. Furthermore, the corrosion response and mechanisms operating in a WC-Co hardmetal (with a nominal 30 vol% binder) were analysed in an equivalent manner in order to provide a baseline comparison.

4.2. Experimental Procedures

4.2.1. Raw Materials and Processing

The TiC powder (lot no. PL20125339; D_{50} = 1.25 μm) was obtained from Pacific Particulate Materials (Vancouver, BC, Canada). The $TiC_{0.7}C_{0.3}$ (lot no. L25809; D_{50} = 2.10 μm), $TiC_{0.5}N_{0.5}$ (lot no. L29865; D_{50} = 1.74 μm), and $TiC_{0.3}N_{0.7}$ (lot no. L25747; D50=1.72 μm) powders were obtained from Treibacher Industrie AG (Althofen, Austria). The Ni_3Al binder powder was generated in-situ in the cermets through reaction sintering a mixture of Ni powder (lot no. L10W013; 2.2 - 3.0 μm) and NiAl powder (lot no. D28X029; D_{50} = 38 μm), which were both provided by Alfa Aesar (Ward Hill, MA, USA); the NiAl exhibited a composition with a 1:1 elemental weight ratio.

Cermet samples were prepared by mixing appropriate amounts of the desired ceramic powder with the corresponding Ni and NiAl powders. In order to generate sufficient green strength in the pressed samples, 0.5 wt% polyvinyl butyral resin was also added to all compositions. Each composition mixture was then ball milled with yttria stabilized zirconia media in acetone for 24 hours, followed by a 24 hour drying period. The dried powders were sieved through a 75 μm stainless steel mesh, and uniaxially pressed at 45

MPa into discs of 31.75 mm in diameter and ~6 mm in thickness. The discs were then vacuum bagged and cold isostatically pressed at 207 MPa. Sintering was performed under dynamic vacuum of approximately at 1550˚C for 1 hour, with the samples held in a lidded alumina (Al_2O_3) crucible, and supported on a bed of 'bubble' Al_2O_3 within the crucible.

Single-phase TiC and Ti(C,N) ceramics and intermetallic Ni_3Al were also prepared individually using SPS, in the form of disks 40 mm in diameter and ~8 mm in thickness. Pre-alloyed Ni_3Al powder (lot no. NAD71; $D_{50} \leq 150$ μm) was used in this instance (Homogenous Metals, Inc., Clayville, NY, USA); the relatively coarse nature of this powder makes it unsuitable for cermet synthesis. The Ti(C,N) ceramic powders were sintered at 1800˚C for 10 minutes, under a 50 MPa applied load, while TiC powder was sintered at 1650˚C for 5 minutes, under a similar load. The pre-alloyed Ni_3Al powder was SPS processed at 1200˚C for 5 minutes, again at 50 MPa applied load.

In order to compare the performance of the present cermets with a more conventional composite system, WC-based hardmetal samples, with 18wt% Co binder (equivalent to ~30 vol.%) were also obtained (Part no. ZM6; Ultra-met Inc., Urbana, OH, US). These samples were provided in the form of rectangular specimens (~10 x 10 x 7mm), and exhibited a mean grain size of ~5 μm. The WC-Co hardmetals were manufactured through dynamic vacuum sintering to ensure minimal residual porosity.

The densities of the various sintered samples were calculated using Archimedes' principle, in distilled water, and compared to the estimated theoretical density, determined by a simple rule of mixtures for the individual constituents. Surface preparation for microscopy and electrochemical characterization was performed by sequential grinding and polishing, using successively finer diamond particles, starting with 160 μm diamond

grit impregnated resin pads, and finishing with 0.25 μm diamond paste. Microstructural characterization was performed using scanning electron microscopy (SEM; Model S-4700, Hitachi High Technologies, Toyko, Japan), with associated compositional analysis conducted using energy dispersive X-ray spectroscopy (EDS; Inca X-maxN, Oxford Instruments, Concord, MA, USA).

4.2.2. Electrochemical Characterization

Electrochemical measurements were performed at room temperature (21 ± 2ºC), using potentiostat/galvanostat (EG & G Model 273A, Princeton Applied Research, TN, USA) and frequency response analyzer (Solartron Model 1250, Schlumberger, TX, USA). The corrosion tests were performed in a three-electrode flat cell, with the samples placed as the working electrode, a platinum mesh (Pt) as the counter electrode, and a saturated calomel electrode (SCE; -0.241 V vs. a standard hydrogen electrode) as the reference. Consequently, all of the potentials are subsequently reported vs. SCE. The electrolyte was prepared using 3.5 wt.% NaCl in distilled water at room temperature (21 ± 2ºC). The test surface area of the working electrode was 1 cm^2 for the cermets and ceramics, and approximately 0.25 cm^2 for the single-phase Ni_3Al. Prior to each polarization measurement, a minimum of 2 hours of sample immersion in the electrolyte was allowed to ensure nominally steady-state conditions and to determine the open circuit potential (OCP). A potential scan rate of 0.1667 mV/s was used for all potentiodynamic tests, in both the forward (anodic direction) and reverse scans (where appropriate, for cyclic testing). The applied potential was controlled during testing using the CorrWare software package (CorrWare for Windows, Version 2.8, Scribner Associates, Inc., Southern Pines, SC, USA).

Potentiodynamic polarization measurements were conducted by scanning from -1.0 to +1.0 V (vs. SCE) for all studied compositions. The corrosion current density (i_{corr}) and potential (E_{corr}) were estimated using an instantaneous Tafel-type fit corrosion analysis software (CorrView Version 2.8, Scribner Associates, Inc., Southern Pines, SC, USA). This software applies the Levenberg-Marquardt method[105], following an iterative, non-linear least squares fit algorithm for the potentiodynamic polarization data within ±250 mV of the OCP. The Tafel curve is simulated by fitting four parameters of the Tafel equation (namely, i_{corr}, E_{corr} and the anodic and cathodic Tafel slopes, β_a and β_c, respectively). Subsequent refinements of those parameters are then used to minimise the sum of the differences in the current values for the real and simulated curves. To further confirm the accuracy of this approach, manual fits of the anodic and cathodic Tafel slopes were also performed for selected tests within the CorrView software.

Based on the measured i_{corr} values, the extrapolated corrosion rates (in mm/year) were determined following the ASTM standard procedure[37]. Corrosion rates were determined assuming both a full corrosion area (i.e. 1 cm^2), and also a 'modified area', using adjusted values of i_{corr} (i.e. i_{corrMA}), based on the area of exposed metallic binder, following the approach of Hochstrasser-Kurz[13];the modified area is applicable when galvanic corrosion occurs, and only the metallic binder is 'active' in the corrosion process. In these two cases the material composition for corrosion rate calculations was based on the mean cermet composition and the binder composition, respectively.

For cyclic polarization tests, the potential scans were conducted in the anodic direction until a user-programmed value was reached, and then scanned in the cathodic direction back to the initial voltage. For the current study, this cycled range was between -1.0 and +1.0 V (vs. SCE). Cyclic polarization tests were performed to determine both the pitting

potential, E_{pit}, defined as the potential where the rate of change of the current density increases rapidly, and the protection potential, E_{prot}, where the reversed segment of the polarization curve crosses back over the initial segment. A minimum of 3 samples was tested for each composition and test procedure in order to ensure the reproducibility of the results.

4.2.3. Post-Corrosion Evaluation

After corrosion testing the cermet samples were examined using SEM, for comparison with the as-prepared material. Post-corrosion surface compositional modifications were assessed using EDS analysis in the SEM. The electrolyte pH was measured using a portable pH meter (model E488, Metrohm Canada Inc., Mississauga, ON, Canada), both before and after electrochemical tests. The pH meter was initially calibrated using a variety of buffer solutions, for pH 4, 7 and 10 (Fisher Scientific Co., Ottawa, ON, Canada). The post corrosion electrolyte was collected for analysis using inductively coupled plasma atomic emission spectroscopy (ICP-OES; model Varian Vista Pro, CA, USA), with an internal calibration standard (scandium). The electrolyte was filtered through a 1.5μm pore size (ProWeigh®, Environmental Express, Charleston, SC, USA), and the recovered solids and filtered solution were separated. The solids on the filters were then oven dried (model Isotemp™, Fisher Scientific Co., Ottawa, ON, Canada) at a temperature of 105°C. After the solids were dried and cooled, they were then weighed in order to obtain the amount of solids in each samples. The obtained solids were then digested by a near total acid leach digest procedure, which consisted of 4 different acids

(HF, HNO_3, $HClO_4$, and HCl). The resulting solution obtained from both the recovered solids and the filtrate were then analysed by ICP-OES.

4.3. Results and Discussion

4.3.1. Cermet Characterization

The vacuum sintered cermet compositions all achieved a minimum of 98% of their theoretical density, regardless of ceramic composition (i.e. the N:C ratio). The cermets exhibited a generally uniform microstructure, while the size and shape of the ceramic grains were dependent upon the C:N ratio of the ceramic phase. The general microstructural evolution of these materials is discussed in greater detail in a prior paper[74]. For the present batches of materials, microstructural analysis has shown that an average grain size of ~5.5 μm was observed for the TiC-based cermets, which is reduced to ~2.6 μm for those based on $TiC_{0.5}N_{0.5}$. This observation confirms that the presence of N in the Ti(C,N) based systems results in refinement of the overall microstructure by decreasing the relative associated surface energy[91]. Conversely, from prior studies the changes in the ceramic grain size relative to the volume fraction of the Ni_3Al binder have been found to be negligible, while the binder mean free path increases with increasing Ni_3Al content[92]. With this in mind, it has been demonstrated that the oxidation properties of Ni based alloys can be improved by decreasing the grain size, which allows formation of continuous α-Al_2O_3 protective scales on Ni_3Al[93–95].

Some studies have suggested that the amount of N in the Ti(C,N) phase also effects the size and formation of any core-rim structure that might occur[91]. In the current study, a core-rim structure was only observed in TiC-Ni_3Al cermet composition (Figure 17), while homogenous carbide grains were seen in Ti(C,N)-Ni_3Al compositions, with no core-rim

formation apparent. The composition of the core region was found to be primarily (undissolved) TiC, while Ti, C and small amount of W in solid solution was present in the composition of the rim. It is concluded that the formation of a core-rim structure in the TiC-based materials is related to presence of impurities, primarily W, which are introduced into the composition during commercial production of the TiC powder (i.e. size refinement with WC milling media); W contamination of the present, 'as-received' TiC powder was confirmed through prior ICP-OES evaluation[92].

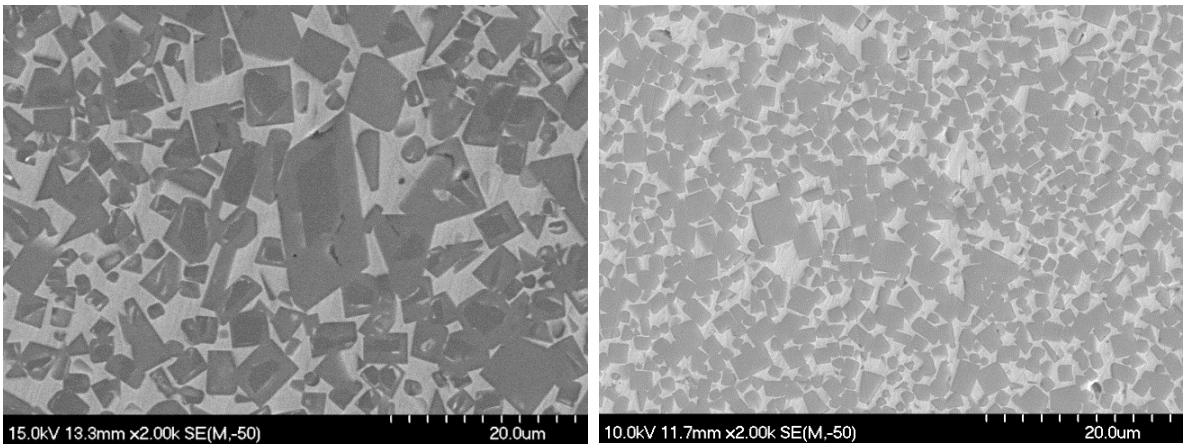

Figure 17. Representative SEM images of: (a) the core-rim structure in the TiC-Ni_3Al cermets, and (b) the absence of a core-rim structure in $TiC_{0.7}N_{0.3}$-Ni_3Al .

In terms of the SPS processed, single-phase TiC and Ti(C,N) samples, densities of 98 % of theoretical were achieved, with the exception of $TiC_{0.7}N_{0.3}$ which reached ~94 % of theoretical. SEM and EDS analyses have shown that the SPS processed TiC samples formed W rich zones at the grain boundaries of the TiC grains (the light contrast regions in Figure 18), rather than a core-rim structure, as noted in the TiC-based cermets.

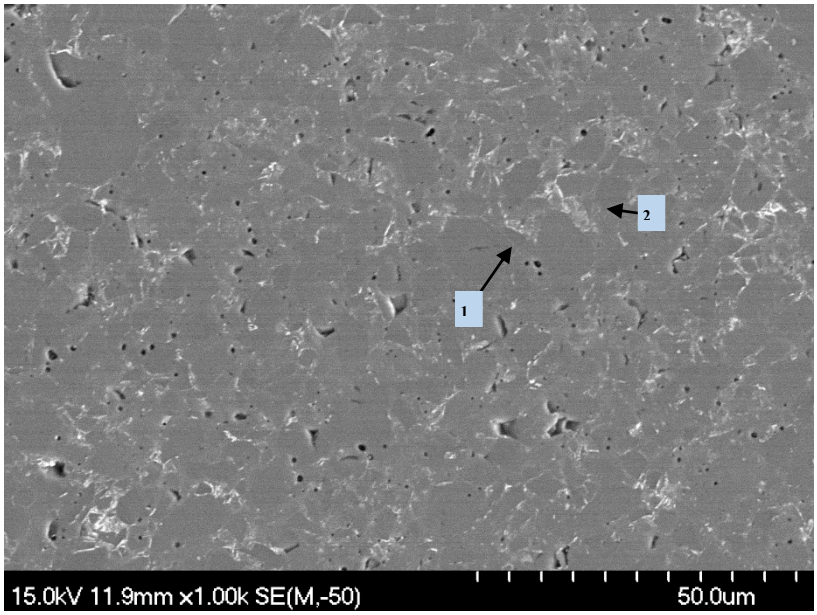

Figure 18. Representative SEM image of a single phase TiC sample: 1. W rich zones, and 2. TiC grain.

The single-phase Ni_3Al intermetallic binder phase only achieved ~77.2% of theoretical density; this low density may be subsequently improved through application of a revised SPS cycle, which was beyond the scope of the present study. Higher densities have been achieved for SPS processing of intermetallic Ni_3Al by increasing the sintering time to 10 minutes, at 950˚C and pressure of 65 MPa, when using a nanocrystalline Ni_3Al powder[93]. While the densities were low for the Ni_3Al samples, they were still found to be suitable for the corrosion assessment; in this instance a degree of caution must obviously be taken when considering the exposed surface area during testing.

For the commercial WC-Co materials (with a nominal 30 vol.% binder content), the density calculation indicated values in excess of 98% of theoretical. An average mean WC grain size of ~5 μm was observed, which did not show any internal grain features (e.g. core-rim), while maintaining a consistent faceted shape.

4.3.2. Electrochemical Analysis

4.3.2.1. Open Circuit Potential (OCP)

The results of OCP analysis following a 2 hour stabilization period for each of the cermet compositions, with 30 vol% metallic Ni_3Al, as well as the single-phase SPS processed ceramics, are presented in Figure 19. Higher OCP relates to materials that are more noble in the electrochemical characteristics, and which can be anticipated to have better corrosion responses in the specific environment they are tested in. The comparison of OCP for the cermets with various C:N ratios in their ceramic phase composition, shows that an increase of N in the ceramic phase corresponds with an increasing value of the OCP toward more noble potentials. In comparison to the cermets and single phase ceramics, the single phase Ni_3Al showed an OCP value of approximately -0.361 ± 0.019 V (vs. SCE) after 2 hours stabilization.

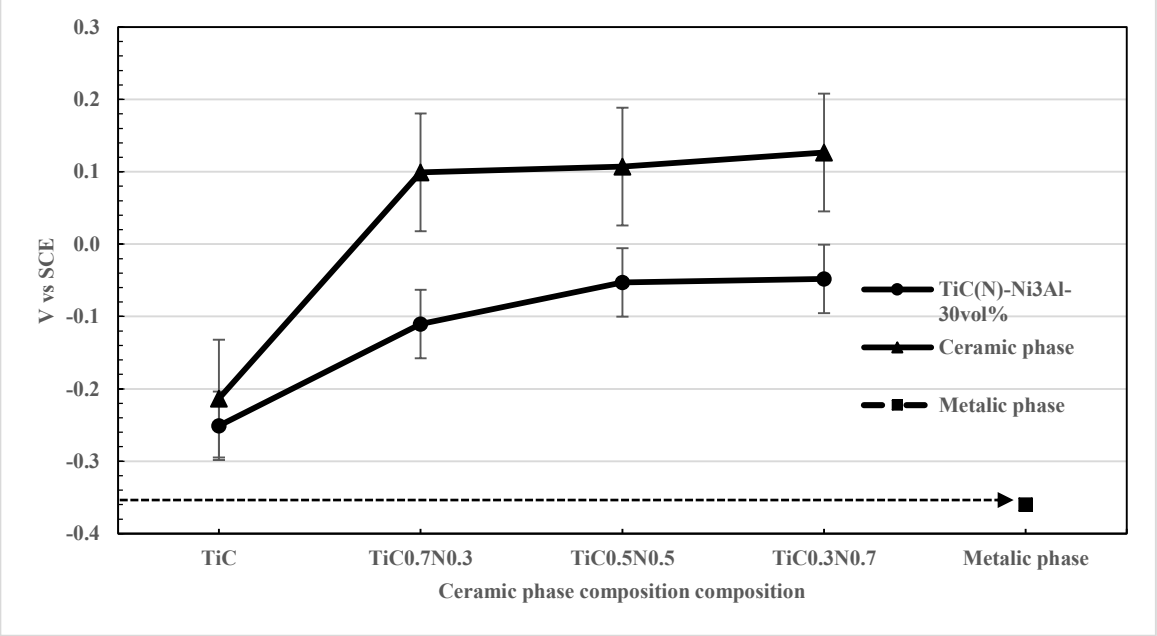

Figure 19. Average OCP values, measured after 2 hours stabilization, for the TiC and Ti(C,N) cermets and single phase ceramics.

In the presence of ceramic and metallic phases with differing corrosion potentials, a galvanic corrosion effect may be expected to be present. The severity of this depends on the relative difference between the corrosion potentials, and the polarization characteristics, of the two phases in contact. The result of OCP analysis on the single-phase ceramic and Ni_3Al intermetallic components suggests that the ceramic phases are cathodic to Ni_3Al (Figure 19)[20]. In addition, for the present composite systems, the OCP difference between the anode and cathode increases with incorporation of N within the ceramic phase (Figure 19). An increase in the difference in oxidization potential is effectively proportional to an increase in corrosion rates, due to the effect of galvanic coupling. Furthermore, it is apparent that the average OCP values for the cermet materials are higher when compared to the single-phase Ni_3Al, which is a result of the passivation characteristics of the ceramic phase and the associated formation of a protective oxide layer. Similar conclusions have been made relating to the zero potential galvanic effect, when using a zero resistance ammeter and calculating the galvanic current density[23,106]. In comparison to the present Ti(C,N) cermets, the average OCP value for the commercial WC-Co hardmetal was determined to be -0.445 ± 0.25 V (vs. SCE), which is significantly more negative than either the Ti(C,N) cermets or the single phase metallic and ceramic compositions[11].

4.3.2.2. Potentiodynamic Polarization

Representative potentiodynamic polarization curves for the SPS processed single-phase ceramics and the Ni_3Al intermetallic specimen are presented in Figure 20. Evaluation of the polarization curves allows determination of the corrosion potential (E_{corr}), and current

densities (i_{corr}), which were obtained from subsequent Tafel extrapolation, and are presented in Table 2.

Table 2. Average corrosion parameters for the single phase TiC and Ti(C,N) ceramics, and the Ni_3Al intermetallic binder.

Type	OCP (V vs. SCE)	E_{corr} (V vs. SCE)	i_{corr} (A/cm^2)	i_{pass} (A/cm^2)
TiC	-0.209±0.035	-0.173±0.094	$1.28 \times 10^{-6} \pm 1.01 \times 10^{-6}$	$1.25 \times 10^{-4} \pm 4.92 \times 10^{-5}$
$TiC_{0.7}N_{0.3}$	0.100±0.039	-0.096±0.105	$1.00 \times 10^{-6} \pm 1.15 \times 10^{-6}$	$5.02 \times 10^{-6} \pm 2.98 \times 10^{-6}$
$TiC_{0.5}N_{0.5}$	0.105±0.018	-0.141±0.092	$7.37 \times 10^{-7} \pm 3.73 \times 10^{-7}$	NA
$TiC_{0.3}N_{0.7}$	0.127±0.052	0.087±0.158	$5.12 \times 10^{-8} \pm 7.36 \times 10^{-8}$	$8.54 \times 10^{-7} \pm 4.2 \times 10^{-7}$
Ni_3Al	-0.363±0.19	-0.428±0.003	$5.09 \times 10^{-7} \pm 1.90 \times 10^{-7}$	$3.93 \times 10^{-2} \pm 2.23 \times 10^{-2}$

In a previous study performed on the electrochemical corrosion of Ti(C,N) composites, it was observed that the dissolution of TiC and TiN takes place in various stages, with respect to the change of potential at the exposed sample surface[107]. It was noted that an oxycarbide (TiC_xO_y) layer forms on the surface of TiC at a potential close to -0.144 V, which is not stable enough to prevent the dissolution TiC through the subsequent voltage range up to a potential of 0.156 V. In the case of Ti(C,N) compositions, the protective oxide film that was formed was demonstrated to exhibit a more complex and stable structure, comprising of a thin $TiC_xN_yO_z$ inner layer, then TiO and finally a layer of TiO_2[100]. In this instance, TiO and TiO_2 form at a potential around 0.3 V, but the dissolution rate is significantly lower than TiC (Equation 24).

$$TiCN + H_2O \rightarrow TiC_xN_yO_z + H^+ + e^- \qquad \textbf{Equation 24}$$

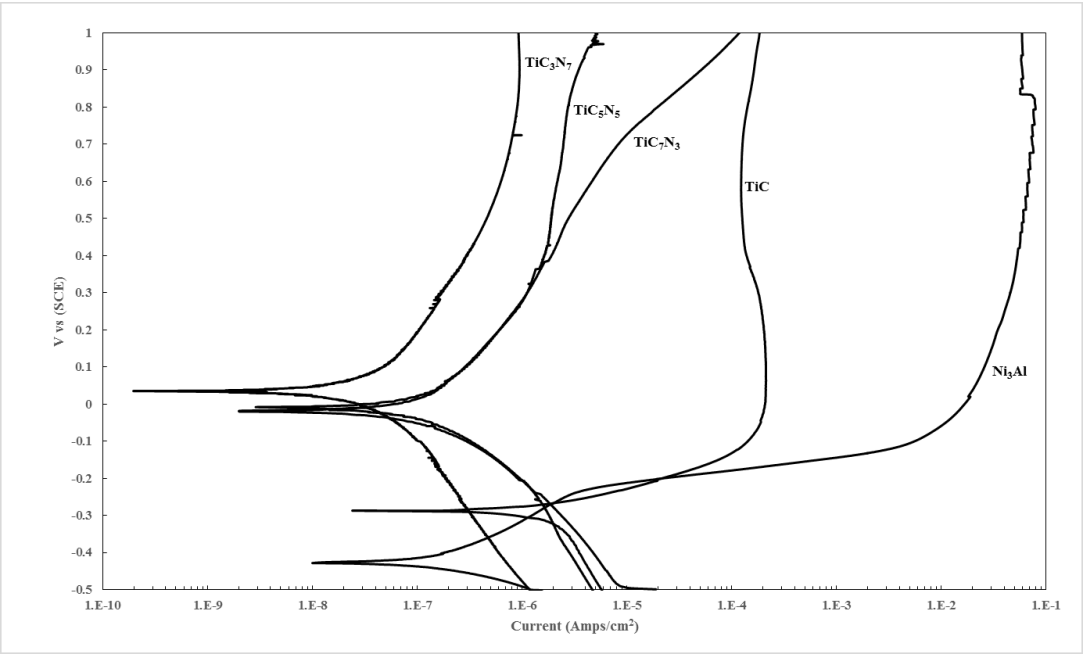

Figure 20. Potentiodynamic polarization curves for the single-phase ceramic and intermetallic phases.

Examination of potentiodynamic data (Figure 20), has shown there exists a difference of approximately 0.33 V between the least and most noble corrosion potentials for the ceramic phases. The highest current density is 2.58 x 10^{-6} (± 1.4 x 10^{-6}) A/cm^2, associated with a corrosion potential of approximately -0.29 V, for the TiC (i.e. no N in its composition). More positive E_{corr} values and a less active surface (i.e. lower i_{corr}) was observed with increased incorporation of N into the ceramic phase; the highest E_{corr} and lowest i_{corr} were noted for the samples with a 30:70 C:N ratio (i.e. the highest N content). Furthermore, the passivation behavior of Ti(C,N) compositions changes, as the rapid rate of current density increase is reduced, thereby lowering the probability of formation of metastable pits prior to passivation of the surface[108]. However, it is important to note that by introducing, and then increasing the N content in the ceramic phase, the potential difference between the ceramic and metallic phase is also increasing, which can then be expected to increase the effect of galvanic coupling in the composite systems. According

to the mixed potential theory, the potentials related to the galvanic coupling between ceramic and binder phase are obtained by extrapolation of the anodic and cathodic slopes of the related materials[109]. Table 3 is constructed by applying mixed potential theory on the single-phase ceramics and Ni_3Al intermetallic. To identify galvanic couples using the mixed-electrode theory, collections of cathodic polarization diagrams obtained from ceramic phases with a 30:70 C:N ratio were plotted with anodic polarization diagrams of Ni_3Al. The value of current and its corresponding potential at the point of intersection between the cathodic and anodic curves is then recorded as galvanic corrosion current I_{couple} and galvanic potential E_{couple} for couples consisting equal areas exposed to 3.5wt% NaCl[110,111].

Table 3. Calculated corrosion parameters related to ceramic and metallic galvanic couples.

Galvanic couples	E_{couple}	i_{couple}
TiC-Ni_3Al	-0.326±0.012	4.31 x 10^{-6}
$TiC_{0.7}N_{0.3}$-Ni_3Al	-0.329±0.024	2.97 x 10^{-6}
$TiC_{0.5}N_{0.5}$-Ni_3Al	-0.339±0.008	2.24 x 10^{-6}
$TiC_{0.3}N_{0.7}$-Ni_3Al	-0.397±0.017	8.56 x 10^{-7}

A small decrease in the value of E_{couple} was observed when the Ni_3Al intermetallic phase was coupled to the ceramic phases with increasing N in their composition. This indicates that the TiC-based cermets will exhibit the least amount of galvanic coupling, compared to the ceramic phases containing N. However, the very low value of i_{couple} that relates to Ni_3Al in combination with $TiC_{0.3}N_{0.7}$ reduces the chances of galvanic coupling for the specific test environment used, which helps to explain the better corrosion (oxidation) properties of the cermets with higher amount of N in their composition.

Figure 21, shows a comparison of the potentiodynamic polarization curves obtained for the TiC-Ni_3Al cermet, together with single-phase TiC and Ni_3Al, all in the 3.5% NaCl aqueous electrolyte. The corrosion potential (E_{corr}) of the Ni_3Al sample is about -0.42 V (vs. SCE), and it exhibits an anodic polarization curve with a slope (b_a) of ~94.9 mV/decade. For the single-phase TiC ceramic specimen, $E_{corr} = -0.288$ V (vs. SCE), and this material shows an anodic behavior with low slope and spontaneous current increase (with a passivation current density, i_{pass}, up to $i_{pass} = 2.1 \times 10^{-4}$ A/cm^2), immediately above corrosion potential. However, passivation occurs at a significantly lower current density for the ceramic phase when compared to the metallic phase. The corrosion potential of TiC-Ni_3Al cermets was found to be more noble than both the ceramic and the Ni_3Al intermetallic phases for this composition ($E_{corr} = -0.184 \pm 0.032$ V (vs. SCE)), suggesting that the dissolution rate for Ni_3Al within the cermet composition is slower than in the bulk state. The slope of anodic curve and the value of the passivation current for TiC-Ni_3Al are both low, and close to that exhibited by Ni_3Al, which may arise as a result of dissolution of Ni_3Al regions in the surface. Furthermore formation of metastable pits, prior to the active pitting potential (evidenced by a sudden shift in current density), was observed for the TiC-based cermets.

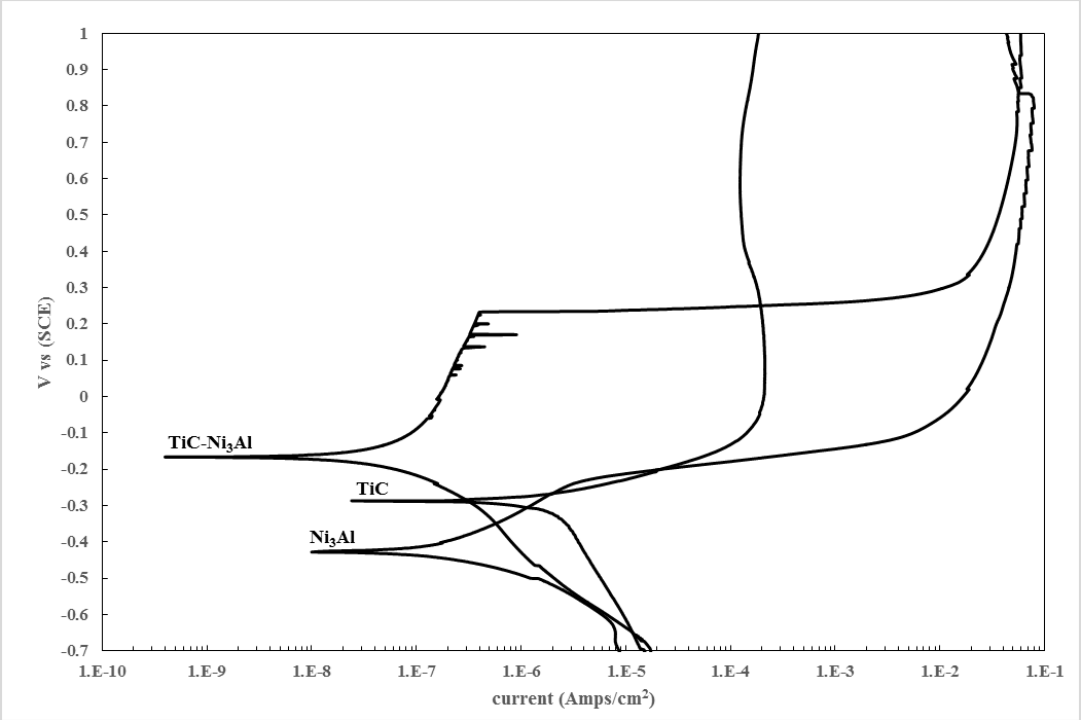

Figure 21. Typical polarization curves observed for the TiC-Ni_3Al cermet, single-phase TiC, and single phase Ni_3Al, in a 3.5 wt.% NaCl aqueous solution.

Figure 22 (a) demonstrates typical potentiodynamic polarization curves obtained for the various cermet compositions. These examples show a similar anodic and cathodic behavior for all of the compositions, regardless of the N content in ceramic phase for Ti(C,N). $TiC_{0.7}N_{0.3}$-Ni_3Al was observed to have the most positive E_{corr}, although the slope of the anodic polarization segment remained lower than the rest of the compositions, leading to this composition having the highest current density at its passivation potential. For comparative purposes, a typical potentiodynamic polarization curve for the commercial WC-Co material is shown in Figure 22(b). The mean values of the corrosion parameters, including E_{corr}, E_{pit}, E_{rp}, i_{corr} and i_{pass}, were obtained using both cyclic and potentiodynamic polarization analysis for each TiC and Ti(C,N) cermet composition, and these are presented in Table 4. During upward scanning in a cyclic polarization, formation of stable pits can be determined at E_{pit} where the current increases sharply from

the passive current values, upon reversal of the scan direction, repassivates at E_{rp} where the current decreases again[40,112]. For comparison purposes, the same parameters for the WC-Co hardmetal are presented in Table 5.

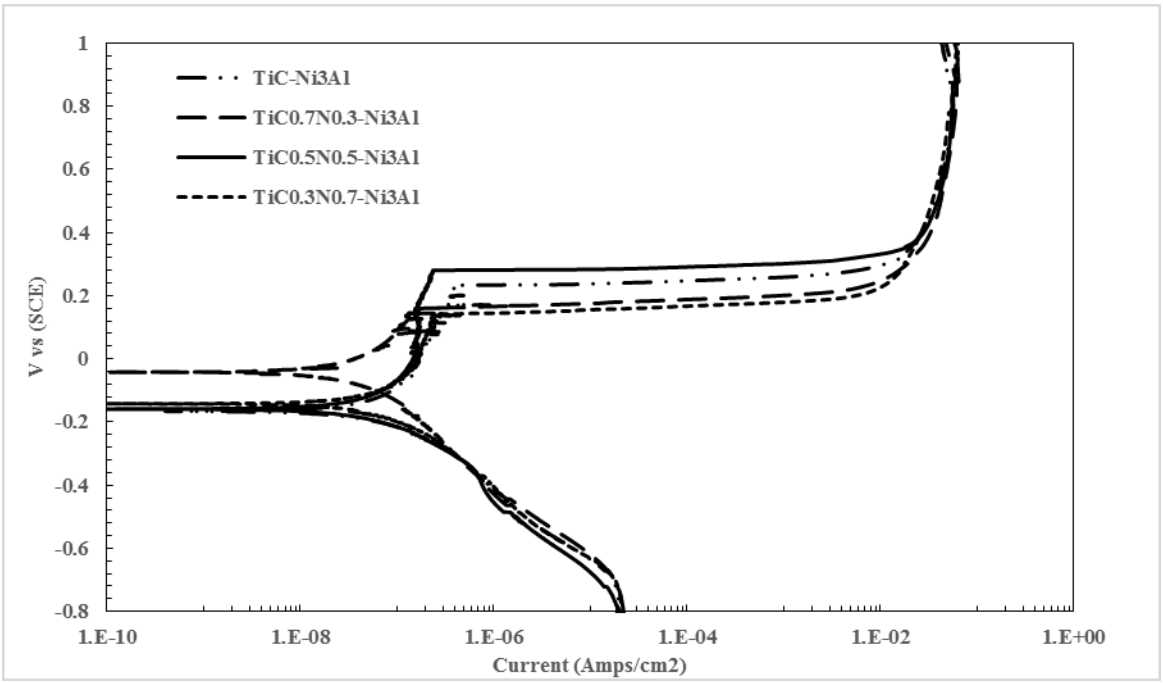

(a)

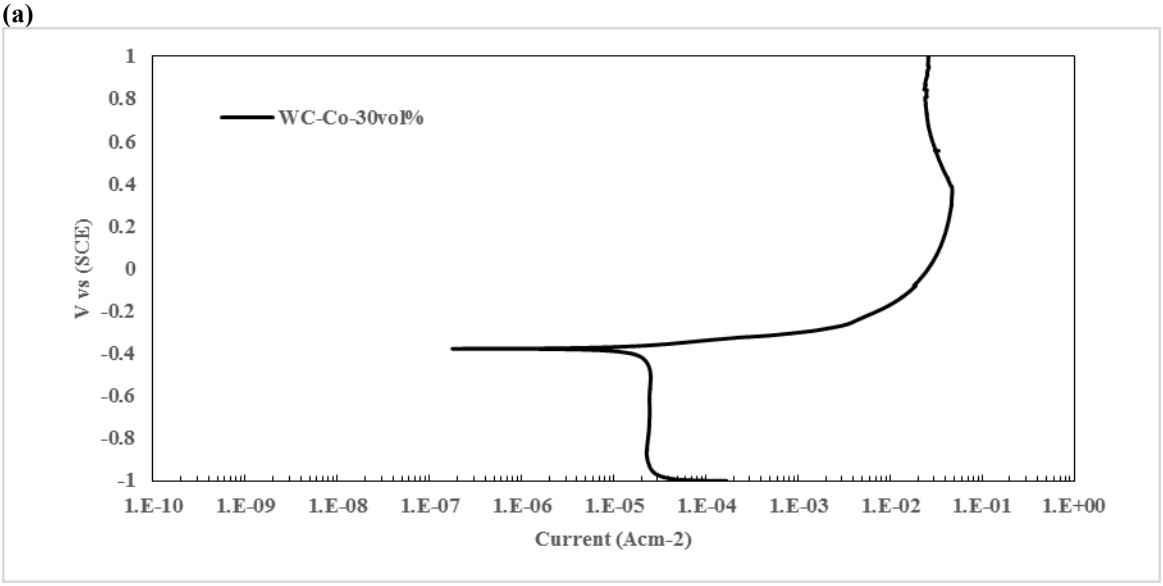

(b)

Figure 22. Representative potentiodynamic polarization curves for (a), Ti(C,N)-Ni_3Al cermet compositions with, in a 3.5% NaCl aqueous solution and (b), A representative potentiodynamic polarization curve for the commercial WC-Co hardmetal in an identical electrolyte.

Table 4. Mean corrosion parameters of the TiC and Ti(C,N)-Ni_3Al cermets. All experiments were performed in an aqueous electrolyte with 3.5 wt.% NaCl.

Type	OCP (V vs. SCE)	E_{corr}±0.04 (V vs. SCE)	E_{pit} (V vs. SCE)	E_{rp} (V vs. SCE)	i_{corr}±1.5x10^{-7} (A/cm^2)	I_{prot}±1.5x10^{-7} (A/cm^2)	i_{pass}±1.5x10^{-7} (A/cm^2)
TiC	-0.25±0.28	-0.18±0.03	0.22±0.02	0.23±0.02	9.75 x 10^{-8} ±4.85 x 10^{-8}	1.85 x 10^{-2}±0.02	3.25 x 10^{-1} ±0.032
$TiC_{0.7}N_{0.3}$	-0.11±0.11	-0.11±0.08	0.15±0.02	0.32±0.02	9.36 x 10^{-8} ±1.18 x 10^{-7}	2.44 x 10^{-2}±0.02	1.78 x 10^{-1} ±0.16
$TiC_{0.5}N_{0.5}$	-0.053±0.13	-0.19±0.03	0.28±0.02	0.32±0.02	1.54 x 10^{-7} ±1.34 x 10^{-7}	1.72 x 10^{-2}±0.02	7.68 x 10^{-2} ±0.11
$TiC_{0.3}N_{0.7}$	-0.01±0.02	-0.17±0.04	0.14±0.02	0.28±0.02	5.36 x 10^{-8} ±2.75 x 10^{-8}	3.61 x 10^{-2}±0.02	7.59 x 10^{-2} ±0.08

Taking into account a typical standard deviation of ±0.02 to 0.09 V (vs. SCE) for the measured potentials, it is apparent that the amount of N in the ceramic phase does not have a significant effect on corrosion potential in the Ti(C,N)-Ni_3Al cermets. The cermets follow a similar trend to that observed for the single-phase ceramics, in terms of E_{corr}, OCP and E_{rp}. The passivation current, i_{pass}, significantly decreases through the increasing addition of N to the ceramic phase of the cermet composition. Conversely, both the corrosion and protection currents remain largely unchanged for all of the compositions, indicating the significance of the dissolution of the binder (the only unchanged component in terms of composition, for all of the cermet samples) during the corrosion measurements. The average passivation current for the Ti(C,N) single-phase ceramics, with C:N ratios from 30:70 to 70:30, and the single-phase Ni_3Al intermetallic binder, were determined to be ~4.36×10^{-5} and 3.9×10^{-2} A/cm^2, respectively. In terms of the Ti(C,N)-Ni_3Al cermets, the average of passivation current density was found to be ~1.6×10^{-1} A/cm^2, which is approximately one order of magnitude higher than the single-phase Ni_3Al. This infers that the corrosion properties of the composite cermet materials are strongly dependent on the oxidation properties of the Ni_3Al binder phase.

The average rates of corrosion, derived from the Tafel slopes that relate to the potentiodynamic polarization curves of the cermets, were calculated for both a 0.3cm^2 and 1cm^2 surface area, following the ASTM standard procedure[37,88]. In this instance the second area relates to the total exposed surface of the cermet, while the first area relates specifically to the area of exposed intermetallic binder (i.e. 30 vol.%). The relationship between the composition of the exposed surface area and the calculation of corrosion rate has been studied previously[113]. It was suggested that for composite materials the rate of corrosion should be calculated for the 'active' region of the surface during the corrosion reaction. Figure 23 presents the average corrosion rates determined for 0.3cm^2 of exposed surface for the cermets prepared with 30 vol.% binder; for this calculation the compositional information needed for the ASTM standard[37] was based solely on the 'active' material, namely the Ni_3Al binder. The calculated rates of corrosion in these cermet materials are seen to decrease with an increasing amount of N in the ceramic phase.

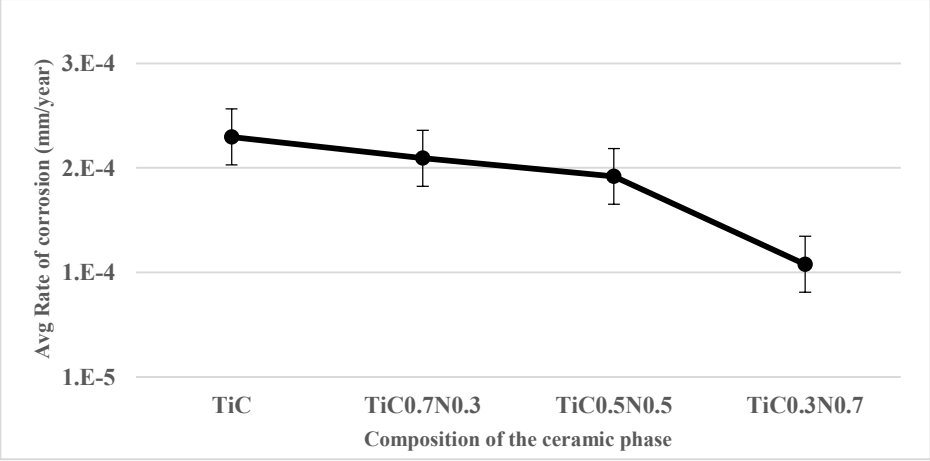

Figure 23. Average rates of corrosion, calculated from the Tafel slopes, relating to the potentiodynamic polarization curves the TiC and Ti(C,N) cermets with 30 vol.% Ni_3Al. All experiments were performed in an aqueous electrolyte with 3.5 wt.% NaCl.

Following a similar procedure as used for the TiC and Ti(C,N) cermets, the average values for the corrosion parameters E_{corr}, $i_{corr,}$ E_{pit} and i_{pass} were also obtained for the commercial WC-Co hardmetal (Table 5). From examination of the potentiodynamic polarization curves obtained for the WC-Co hardmetals, the relatively poor corrosion resistance of the Co binder alone has been effectively reduced within the hardmetal composite, resulting in clear passivation behavior for this composition. However, the WC-Co samples demonstrate significantly higher corrosion current densities and corrosion rates. This is combined with more negative (less noble) values of E_{corr} and OCP, when compared to the TiC and Ti(C,N) based cermets under similar test conditions. For the TiC and Ti(C,N) cermets prepared with a Ni_3Al binder, the highest rate of corrosion was calculated to be 1.98×10^{-4} mm per year, for the TiC-Ni_3Al cermet composition. In comparison, for the commercial WC-Co composition with a nominally similar binder volume and test environment, the corrosion rate was determined to be approximately three orders of magnitude higher, at 3.266×10^{-2} mm per year for 30vol% Co metallic phase. For comparative purposes, published corrosion rates for WC-Co and WC-CoCr based coatings, determined using a similar Tafel extrapolation method were reported by Toma and colleagues to be 7.6×10^{-1} and 3.2×10^{-1} mm per year, respectively[114]. These values are relatively close to the bulk WC-Co assessed in the present work, with the slightly higher corrosion rates likely resulting from coating defects and morphology changes, along with the potential for further galvanic interaction between the coating and substrate. In contrast, Cr_3C_2-NiCr coatings have been reported to exhibit much lower corrosion rates at 8.0×10^{-3} mm per year, which are more in line with the present materials, although still somewhat higher[115]. These studies highlight the

potential of the present materials in terms of providing significantly lowered corrosion rates in comparison to WC-Co (by several orders of magnitude), while recent work has also confirmed that the wear rates for the present cermets are comparable to commercial WC-Co[116,92].

Table 5. Average corrosion parameters for WC-Co 30 vol.% Co binder. All experiments were performed in an aqueous electrolyte with 3.5 wt.% NaCl.

Type	OCP (V vs. SCE)	E_{corr} (V vs. SCE)	i_{corr} (A/cm^2)	E_{pit} (V vs. SCE)	i_{pass} (A/cm^2)	Rate of corrosion (mm/yr)
WC-Co (30vol%)	-0.445±0.025	-0.437±0.002	1.43 x 10^{-5} ±8.7x10^{-8}	-0.437±0.02	0.1	3.266 x 10^{-2} ±1.39x10^{-17}

4.3.2.3. Cyclic Polarization

Cyclic polarization curves obtained from the single-phase TiC and Ti(C,N) ceramics and the Ni_3Al intermetallic phase can provide information that indicates the tendency of both phases toward pitting. Figure 24 demonstrates the typical cyclic polarization curves that are obtained for each of these single-phase materials. Pitting occurs when there is a localized breakdown in the passive film that normally protects the surface from accelerated corrosion attack. The hysteresis loop formed by the cyclic polarization scan is a suggestion of the susceptibility towards pitting corrosion. In materials that exhibit a likelihood of pitting corrosion, the size of the hysteresis loop is an indication of the extent of susceptibility; a larger loop, in a comparison of two materials subjected to pitting analysis, indicates a higher risk of pitting occuring[38,60].

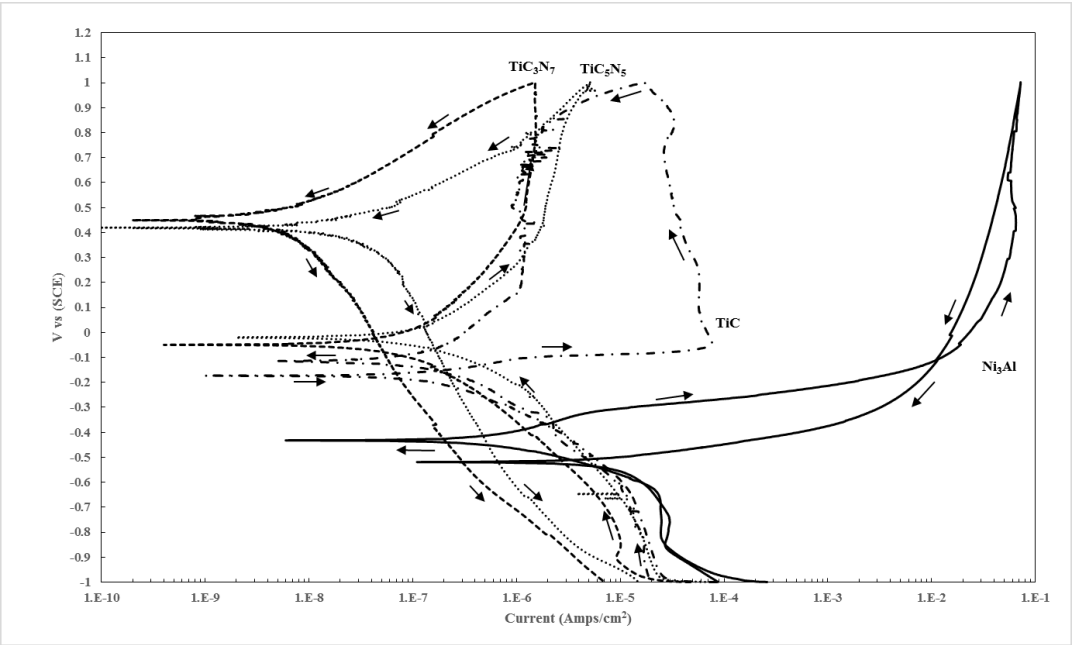

Figure 24. Cyclic polarization analysis on the single-phase TiC and Ti(C,N) ceramics and the Ni_3Al intermetallic. All experiments were performed in an aqueous electrolyte with 3.5 wt.% NaCl.

As shown in Figure 24, the individual ceramic and metallic phases exhibited cyclic polarization curves, with counter clockwise hysteresis loops occurring in each case. Such behavior has also been seen with Ni-Ti-Cr alloys[117]. Several studies have demonstrated that this response is due to the formation of passivating oxide elements found in the exposed surface, which resist localized corrosion[118,119]. The results obtained by these studies also suggest that dissolution of the elements from the surface during polarization is not necessarily a result of the elemental composition of the specimen, but is primarily related to the density, thickness, and re-passivation potential of the oxide film that is formed. Examining the cyclic curves more closely, a short pitting period appears to occur in the case of TiC. When N is present in the ceramic phase, no pitting period arises unless the applied potential exceeds ~1.3 V (vs. SCE), with passivation occurring at moderately low current densities (i.e. $i_{pass} = 5.4 \times 10^{-6}$ A/cm^2). In comparison, the intermetallic Ni_3Al phase passivates at significantly higher current density values (i.e. $i_{pass} = 3.9 \times 10^{-2}$

A/cm^2). In terms of the cyclic response, the Ni_3Al intermetallic formed a small, counter clockwise loop, showing a re-passivation potential (E_{rp} = -0.107 V (vs SCE)) that is noble with respect to its pitting and corrosion potentials. This means a short period of 'metastable' pitting will be followed by formation of an oxide layer, which has been confirmed through EDS analysis. Typical cyclic polarization curves obtained for the current cermet compositions are shown in Figure 25(a). It was apparent that there are no significant differences relating to the addition of N to the ceramic component of the cermet. All of the compositions exhibited a counter clockwise hysteresis loop, with average E_{rp} values ranging from 0.2 to 0.3 V (vs. SCE). The smallest hysteresis loop was measured for the composition $TiC_{0.5}N_{0.5}$-Ni_3Al, and also the shortest rest period (indicated by a constant potential while current rapidly increases during pitting), among the other cermet compositions. In comparing the cyclic polarization curves for the single-phase constituents and the cermets, it was noted that the pitting tendencies of the cermets are very similar to that noted for the Ni_3Al intermetallic; specifically in terms of characteristics such as the slope of the stable pitting period and the current density at the re-passivation potential. This confirms that the dissolution of the material component that relates to pitting corrosion is primarily associated with the corrosion properties of the Ni_3Al binder phase. However, higher values of E_{corr} and E_{rp} were determined for the cermet compositions, compared to the Ni_3Al binder phase, which is the active corroding material within the cermet composition. For comparison purposes, cyclic curves obtained for the commercial WC-Co hardmetal are presented in Figure 25(b).

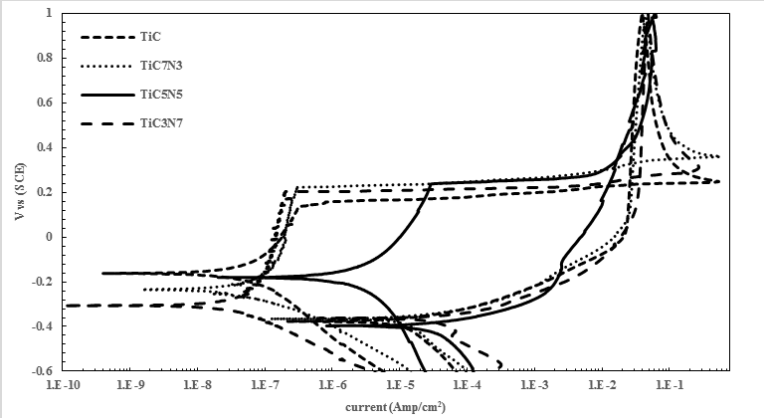

(a)

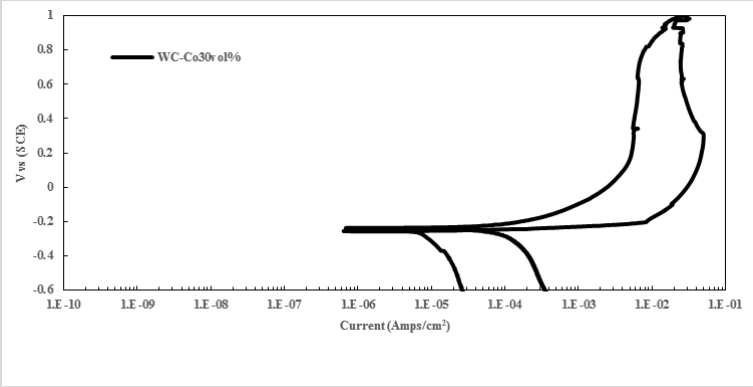

(b)

Figure 25. Typical cyclic polarization curves obtained for (a), TiC- and Ti(C,N)-based cermet compositions and (b) Typical cyclic polarization curve obtained for the commercial WC-Co composition. All experiments were performed in an aqueous electrolyte with 3.5 wt.% NaCl.

As it can be seen in Figure 25(b), larger hysteresis loop has been formed by WC-Co hard metals compared to Ti(CN)-Ni_3Al cermets. Furthermore E_{rp} is almost same as Ecorr in WC-Co hard metals while E_{rp} obtained from the result of cyclic analysis from Ti(CN)-Ni_3Al cermets is noble to E_{corr} which conclude better pitting properties of produced cermet compositions once compared to WC-Co hard metal.

4.3.3. Post Corrosion Analysis

4.3.2.4. Microstructural Analysis

Figure 26 shows representative SEM images of the post polarization surfaces of the single-phase TiC and Ti(C,N) ceramics. The post corrosion surfaces exhibit the formation of pits and destruction of the oxide layer formed on the surface of the TiC. As N is increasingly introduced to the cermet compositions, the surfaces exhibit a more uniform attack, with an apparently more stable passive layer formed on the surface. In this instance the single-phase $TiC_{0.3}N_{0.7}$ ceramic appears to show the least corrosive damage. It is believed that the finer microstructure formed in the Ti(C,N) compositions forms a strong oxide layer, with modified dissolution of the surface at the grain boundaries[120].

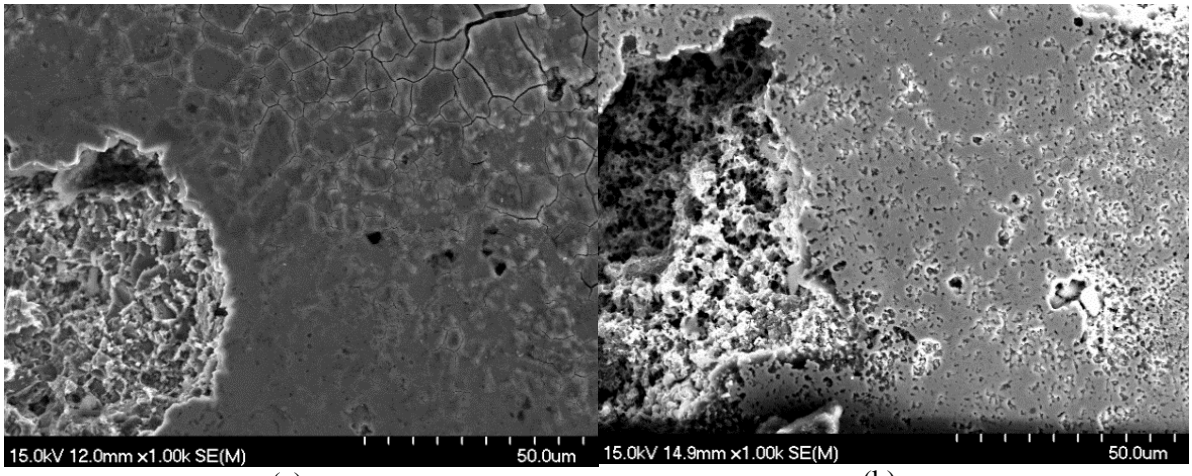

(a) (b)

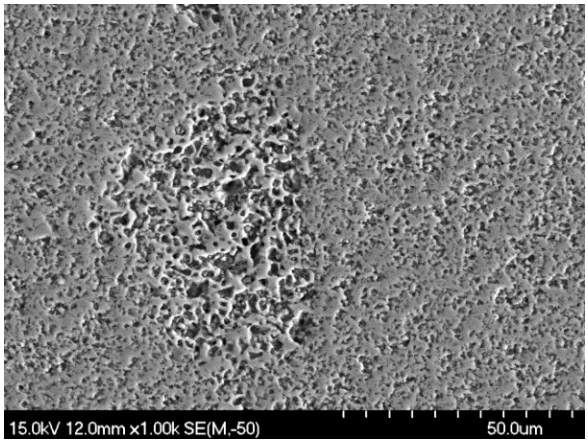

(c)

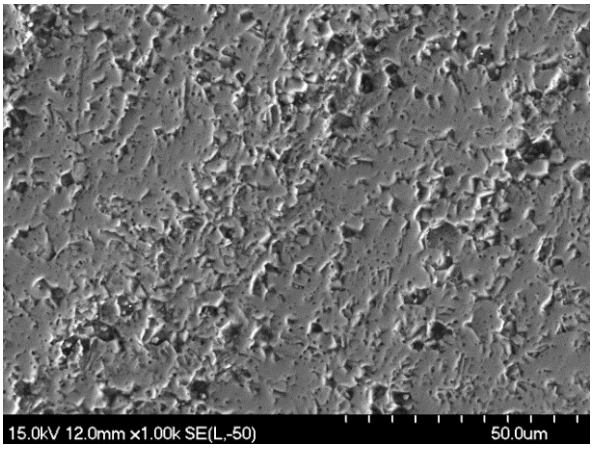

(d)

Figure 26. SEM images obtained from the post polarization surfaces of the single-phase ceramics: (a)TiC, (b)$TiC_{0.7}N_{0.3}$, (c)$TiC_{0.5}N_{0.5}$, and (d)$TiC_{0.3}N_{0.7}$. Samples were polarized from -1 to +1 V (vs. SCE) in an aqueous electrolyte containing 3.5 wt.% NaCl.

Broadly similar results were obtained for the TiC and Ti(C,N) cermet compositions, as shown in Figure 27. The TiC-based cermets have formed random pits on the surface of both the ceramic and intermetallic phases. The cermets that contained N in their ceramic phases exhibited a more uniform attack, which only initiated at the grain boundaries, while the ceramic phase was cathodically protected due to the galvanic coupling of two phases with differing values of E_{corr}. As was demonstrated in the earlier electrochemical analyses, the difference in E_{corr}/OCP between the ceramic and Ni_3Al intermetallic phases increases with the amount of N in the ceramic phase. This shifts the resultant corrosion mechanism from one of localized crevice corrosion to a more uniform, galvanic attack. Consequently, from the electrochemical analyses and the associated calculations of the cermet corrosion rates, this confirms that the uniform galvanic attack has a less destructive effect on the long-term performance of the cermets with N present in their ceramic phase.

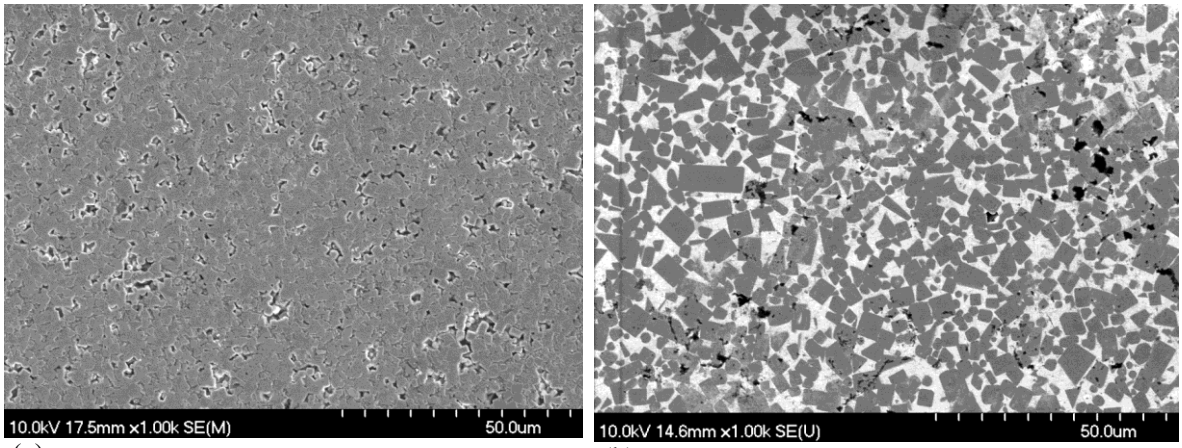

(a) (b)

Figure 27. SEM images obtained from post polarization surfaces of selected cermet compositions: (a) $TiC_{0.3}N_{0.7}$, and (b) TiC. Samples were polarized from -0.5 to +0.5 V (vs. SCE) in an aqueous electrolyte containing 3.5 wt.% NaCl.

Post corrosion SEM images relating to the samples polarized from -1 to +1 V (vs. SCE) have shown that the effective corrosion mechanism is a uniform galvanic attack, resulting in dissolution of the binder in the electrolyte, and leaving a skeleton of the hard ceramic phase behind (Figure 28); similar observations were made for all of the cermet compositions under these polarization conditions. Vladimir *et al* have confirmed the formation of a porous TiO_x oxide layer on the surface of TiC based cermets. For the cermet compositions with addition of N to their ceramic composition, a mixed TiO_x and $TiO(C_x,N_y)$ surface composition was detected[120].

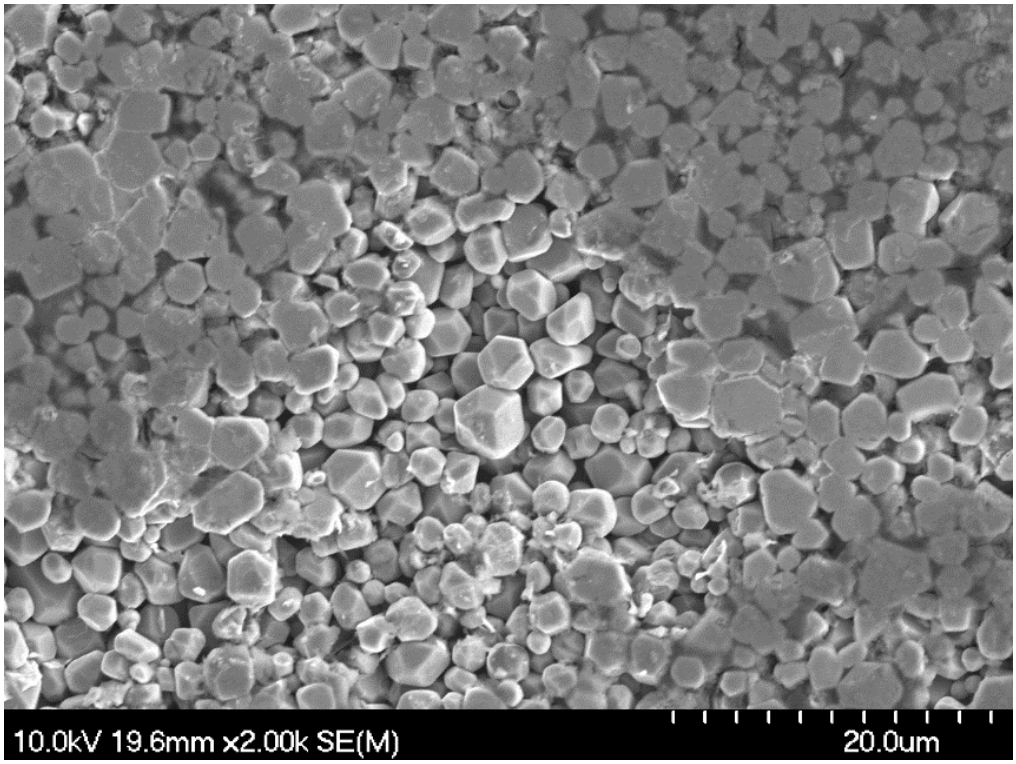

Figure 28. Post polarization surface of the $TiC_{0.7}N_{0.3}$-Ni_3Al cermet. The sample was polarized from -1 to +1 V (vs. SCE) in an aqueous electrolyte containing 3.5 wt.% NaCl.

4.3.2.5. Inductively Coupled Plasma/Optical Emission Spectroscopy (ICP-OES)

The results of ICP-OES analyses on the post-corrosion electrolytes for the TiC and Ti(C,N) cermets are shown in Table 6 and Table 7. The post corrosion electrolyte was filtered and both the filtrate and solid were analysed independently. It is apparent for these data that the amount of N in the ceramic phase of the cermet did not have a significant effect on the surface material that was dissolved during the potentiodynamic polarization treatment (Figure 6); in this instance this relates to ions liberated into the filtrate solution. However, a slight increase in the measured pH values, from 6.4 to 6.7 of the filtrate solution was recorded with increasing N content. Conversely, an increase in the amount of Ti in the recovered particulate material was observed with an increase in

the N content of the ceramic phase, with the amount of Ni and Al remaining largely unchanged for all of the cermets examined.

Table 6. ICP-OES analysis on post corrosion electrolyte solution for the TiC and Ti(C,N) cermets with 30 vol.% Ni_3Al. All experiments were performed in an aqueous electrolyte with 3.5 wt.% NaCl.

Solution	Composition (mg/L)			
sample ID	Al	Ni	Ti	pH
PD TiC-Ni_3Al	0	0.77	0	6.4
PD $TiC_{0.7}N_{0.3}$-Ni_3Al	0.07	0.07	0	6.3
PD $TiC_{0.5}N_{0.5}$-Ni_3Al	0.02	0.12	0	6.5
PD $TiC_{0.3}N_{0.7}$-Ni_3Al	0.06	0.06	0	6.7

Table 7. ICP-OES analysis on the particulates filtered from the post-corrosion electrolyte for the TiC and Ti(C,N) cermets with 30 vol.% Ni_3Al. The particulate material was acid dissolved prior to analysis. All experiments were performed in an aqueous electrolyte with 3.5 wt.% NaCl.

Particulate	Composition (mg/kg)		
Sample ID	Al	Ni	Ti
PD TiC-Ni_3Al	53175.40	307145.00	4540.00
PD $TiC_{0.7}N_{0.3}$-Ni_3Al	48308.70	285174.00	8291.86
PD $TiC_{0.5}N_{0.5}$-Ni_3Al	55633.40	308165.00	12999.70
PD $TiC_{0.3}N_{0.7}$-Ni_3Al	50140.80	292399.00	16730.70

ICP-OES analysis on single-phase ceramic compositions only confirmed a small amount of Ti dissolved in the post corrosion electrolyte recovered from the potentiodynamic polarization analyses. The recorded pH values relating to these solutions are shown in (Table 8). In contrast to the cermet compositions, a small decrease in the pH value was observed when increasing the amount of N in the ceramic phase. The post-test pH value for the single-phase Ni_3Al was found to be similar to those recorded for the cermet compositions, with the pH being increased, again suggesting that the dissolution of the surface during corrosion is primarily related to active dissolution of metallic binder phase, resulting in similar pH values.

Table 8. Measured pH values for the post-corrosion electrolyte solutions after potentiodynamic polarization testing of the single phase TiC and Ti(C,N) ceramics and the Ni_3Al intermetallic.

Composition	pH
TiC	6.3
$TiC_{0.7}N_{0.3}$	6.0
$TiC_{0.5}N_{0.5}$	6.0
$TiC_{0.3}N_{0.7}$	5.9
Ni_3Al	6.8

4.4. Conclusions

The aqueous corrosion behavior of TiC and Ti(C,N) based cermets, with a stoichiometric Ni_3Al intermetallic binder phase, has been investigated in a 3.5 wt.% NaCl solution. Measurement of the OCP was used to determine the equilibrium electrochemical potential. It was concluded that addition of nitrogen in the ceramic phase results in an increase of corrosion resistance (increase in OCP) by refining the microstructure of the composition. Moreover studies on microstructural and mechanical behavior of TiN and TiCN have shown that TiC shares some characteristics of TiN, but brittleness of TiC results in higher loss of material in aggressive environment[121–123]. The potentiodynamic and cyclic polarization responses of the cermet and single-phase materials (both the ceramic and intermetallic constituents) have also been determined, through measurement of E_{corr} and i_{corr}, the extrapolated rate of corrosion, and the tendency towards pitting. It was found that an increase in the N content of the ceramic component (i.e. a reduction of the C:N ratio) within the cermet changes the corrosion mechanism from localized pitting/galvanized corrosion for TiC ceramic phase to uniform galvanized corrosion for the Ti(C,N) ceramic compositions. Based on the calculated rates of corrosion, localized attack was more destructive toward the microstructure of the specimen. It was

demonstrated that selective attack of the binder occurs, and the extent of corrosion and primary mechanism depends on the amount of nitrogen in the Ti(C,N) alloy composition. Unlike Ti(C,N) based cermets, for the WC-Co hardmetals the corrosion characteristics of the Co-based metallic phase have been assumed as the rate determining phase in terms of calculations of the rate of the corrosion. It has been confirmed that micro-galvanic and/or crevice corrosion takes place at the interface of ceramic and metallic phase followed by accelerated dissolution of the binder phase at a pitting potential.

It was demonstrated that the TiC-Ni_3Al and Ti(C,N)-Ni_3Al compositions exhibit extrapolated rates of corrosion approximately three orders of magnitude lower than a comparable commercially obtained WC-Co hardmetal. Consequently, given the essentially identical specific wear rates for the present TiC- and Ti(C,N)-based cermets and the WC-Co hardmetal, these new light weight cermet systems offer considerable promise for the replacement of WC-Co in a variety of applications.

Chapter 5. The Effect of Binder Content on the Aqueous Corrosion Response of WC-Co Cermets

Zhila Memarrashidi and Kevin P. Plucknett

Materials Engineering Program, Department of Process Engineering and Applied Science, Dalhousie University, 1360 Barrington Street, Halifax, Nova Scotia, CANADA

Abstract

WC-Co 'hard metals' are widely used in a variety of industrial applications due to their resistance to abrasive wear, in addition to their high hardness and toughness. However, in contrast to their mechanical properties, the corrosion response of these materials is relatively poor. In the current work the corrosion mechanisms of two WC-Co cermets are analysed, with 10 and 30 vol. % of the Co metal binder, in a 3.5 wt.% NaCl aqueous solution. The assessment of corrosion involved a variety of electrochemical measurements, including open circuit potential, potentiodynamic polarization and cyclic polarization, together with systematic analysis of the post-corrosion solution chemistries using inductively coupled plasma optical emission spectroscopy. The corrosion potential and current density were determined, following Tafel extrapolation, allowing the calculation of the corrosion rates. It is demonstrated that continuous dissolution of the cobalt phase occurs during corrosion, which is a result of poor cermet passivation behavior, and this response increases with the amount of binder in the cermet.

Keywords: Corrosion, Potentiodynamic, Cyclic polarization, ICP-OES, SEM, hardmetals

5.1. Introduction

WC based 'hardmetals' which are often called cemented carbides, are composites comprised of hard grains of tungsten carbide (WC) bonded together in a tough metal matrix. These materials are consequently often referred to as 'cermets'. The most common composition of WC based hardmetals is formed via liquid sintering with Co as the binder phase. Moderately high corrosion and erosion resistance of hardmetals based on WC-Co has extended the use of this type of cermet in many areas such as thermal spray coatings. The increased demand has been followed by many studies on methods of manufacturing and improvement of WC-Co cermet properties. Newer grades contain additional alloying elements for various purposes. For example, extremely fine grains can be produced by addition of Cr to the binder, which is an important factor in controlling the mechanical and electrochemical behavior of the component[27,87].

The crystalline structure of WC is known to be hexagonal (α-WC) or cubic (β-WC), which forms at higher temperatures[81]. In the hexagonal lattice, metal atoms are layered over one another with carbon atoms filling the interstitial gaps between the layers, providing both tungsten and carbon atoms a regular trigonal prismatic arrangement[81]. WC has an approximate Young's modulus of 550GPa and a Vickers hardness value in the range of 1700-2400[82,83]. In acidic solutions, depending on the method of preparation, WC produces WO_3, WO_2, W, and/or W carboxide[3,124]. Co possesses a crystalline structure of HCP at low temperatures, or FCC above a transition temperature of 400°C[125,126]. Co has a Young's modulus of 209GPa and a Vickers hardness value of 1043MPa[127].

Chemical analysis of the surface of WC-Co composites during the different stages of corrosion reactions has shown that in acidic solutions, the dissolution of Co takes place at low potentials[108]. As the pH value of the surface increases, the composition of the oxide

layer changes from CoH and CoH_3 to CoO and Co_3O_4, resulting in a decrease of the oxidation rate[128]. Analyzing the corrosion response of Co individually, and then within the cermet composition as the binder, has shown that the passivity characteristics of Co were improved when used as a binder phase within the cermet composition[109]. This occurs by reducing the anodic current density of the alloy[129]. Another argument has proposed that the corrosion rate of the Co binder is higher than pure Co due to the effect of galvanic coupling between the ceramic and metallic phases[130,131]. Surface observation during the reaction has shown that WC decomposes through a mechanism that cannot be manipulated electrochemically. The galvanic coupling in an aqueous environment results in a rather complex reaction by reducing H and increasing the local pH, which itself will then promote further oxidation of the ceramic phase[131]. This is why the oxidation rate for WC dramatically decreases while coupled with Co at pH values below 10[132].

Previous studies have demonstrated that the mechanical and electrochemical properties of this composition are affected by the amount and composition of the binder phase, the carbide grain size, and the method of manufacture[33,133]. Furthermore, it has been suggested that the electrochemical behavior of this composite system is strongly affected by the potential of the surface in specific environments[134]. In an aqueous solution the continuous oxidation of the composite takes place by preferential corrosion attack of the binder at the open circuit potential (OCP), while dissolution of the WC takes place at higher potentials and under alkaline pH values[135].

Many of these studies have been performed on WC-Co coated surfaces created by different methods. However additional examination of corrosion responses on bulk materials can simplify the understanding of the complex corrosion mechanisms of WC-Co cermets. In particular, this removes any possible reaction between the coating and the

substrate material, which can arise in the event that the coating is either porous or contains cracks.

The present study investigates the corrosion mechanisms of bulk WC-Co cermets with various volume fractions of metallic Co binder phase. Testing has been conducted in an aqueous solutions with 3.5wt% NaCl. The oxidation behavior of WC-Co was assessed by means of electrochemical analysis in this aqueous medium. A variety of electrochemical characterization approaches were followed, including OCP, potentiodynamic polarization (PD), and cyclic polarization (CP) analysis. In addition, microstructural and chemical analyses of the oxidized surfaces and corrosion medium were performed to study the effects of binder content on the electrochemical performance of the manufactured cermets.

5.2. Materials and methods

For propose of present study, WC-6Co (6wt% Co; product no. ZM18; mean grain size ~3.5μm) and WC-18Co (18wt% Co; product no. ZM6; mean grain size ~5.0μm) samples were provided by Ultra-met (Urbana, OH, US) in the form of cuboid specimens (10 x 10 x 7mm); these cermets were manufactured through hot isostactic pressing to achieve full density. Sample surface preparation for corrosion testing was performed using sequential grinding and polishing. Diamond impregnated resin pads were used initially, starting with 160μm, with a finishing step using 0.25μm diamond paste. Microstructural characterization was performed using scanning electron microscopy (SEM; model S-4700, Hitachi High Technologies, Toyko, Japan), with associated compositional analysis performed in the SEM using energy dispersive X-ray spectroscopy (EDS; model Inca X-maxN, Oxford Instruments, Concord, MA, USA).

Electrochemical measurements were performed at room temperature (21 ± 2ºC), with a relative humidity of 40-55%, using a potentiostat/galvanostat (EG&G model 273A, Princeton Applied Research, TN, USA) and frequency response analyzer (model 1250, Solartron Schlumberger, TX, USA). The corrosion tests were performed in a three-electrode flat cell. In this arrangement the samples acted as the working electrode, with platinum mesh as a counter electrode, and a saturated calomel electrode (SCE = -241mV SHE, (standard hydrogen electrode)) as the reference. The electrolyte was prepared using 3.5 wt% NaCl dissolved in distilled water. Testing was conducted at room temperature (21 ± 2ºC). The exposed surface area of the working electrode was 1cm^2. This is corrected to either 0.1 or 0.3 cm^2 for, WC-6Co and WC-18Co, respectively (based on a nominal Co binder volume of 10 and 30 vol%, respectively); in this instance dissolution of binder is assumed to be the rate-determining factor.

Samples were stabilized for 2 hours in the electrolyte solution, and the open circuit potential (OCP) was continuously recorded. Potentiodynamic tests were performed to polarise the surface of the specimen over the potential range from -1V to +1V, with respect to SCE, at the rate of 0.1667mV/s. Tafel extrapolation was then used to determine the corrosion potential, E_{corr}, and the corrosion current, $i_{corr.}$ Calculation of the corrosion rate was subsequently performed using the i_{corr} value, following the procedure outlined in the associated ASTM standard[37]. Cyclic polarization electrochemical analysis was performed for each WC-based composition, by polarising the surfaces with an initial voltage of -1 V, increased to +1 V, and then cycled back to -1 V as the final potential, all with respect to SCE. The reproducibility of the obtained data was determined by testing an average of 3-4 samples for each composition and analysis method.

Post corrosion surfaces were examined for microstructural and compositional changes using SEM and EDS. The evolution of electrolyte pH was determined using a portable pH meter (model E488, Metrohm AG, Ionenstrasse, CH-9100 Herisau, Switzerland). The pH meter was initially calibrated using buffer solutions, at pH 4, 7 and 10 (Fisher Scientific, Ottawa, ON, Canada). The post-corrosion electrolyte was then evaluated using inductively coupled plasma atomic emission spectroscopy (ICP-OES; model Varian Vista Pro, CA, USA), with an internal calibration standard (scandium). The post-corrosion electrolyte solutions were filtered using a Millipore Apparatus on a ProWeigh® binderless filter (Environmental Express, Charleston, SC, USA), with a pore size 1.5 μm, and the solids separated. The solids on the filters were then oven dried (model Isotemp, Fisher Scientific, Ottawa, ON, Canada) at 105°C for 5 h. After the solids were dried and cooled, they were then weighed in order to obtain the amount of residual solids in the electrolyte of each sample. They were then digested by a 'near total acid leach digest' procedure, which consisted of four different acids (HF, HNO_3, $HClO_4$, and HCl). The resulting solutions prepared from the solids and filtrate were then analysed by ICP-OES.

5.3. Results and discussion

5.3.1. Cermet Characterization

Based on a simple rule of mixtures, the density calculation for the WC-Co 10 and 30 vol.% Co cermets indicated values in excess of 98 and 95 % of theoretical density, respectively. Based on the W-C-Co phase diagram, it is expected that some alloying of the Co binder occurs, resulting in the apparently lower than theoretical measured densities. Typical micrographs highlighting the polished surfaces of both compositions are shown in Figure 29. These images highlight that there is negligible residual porosity

in either material, in contrast to the apparent density measurements. The WC grains did not show any internal features (e.g. core-rim) and exhibited a consistent faceted shape.

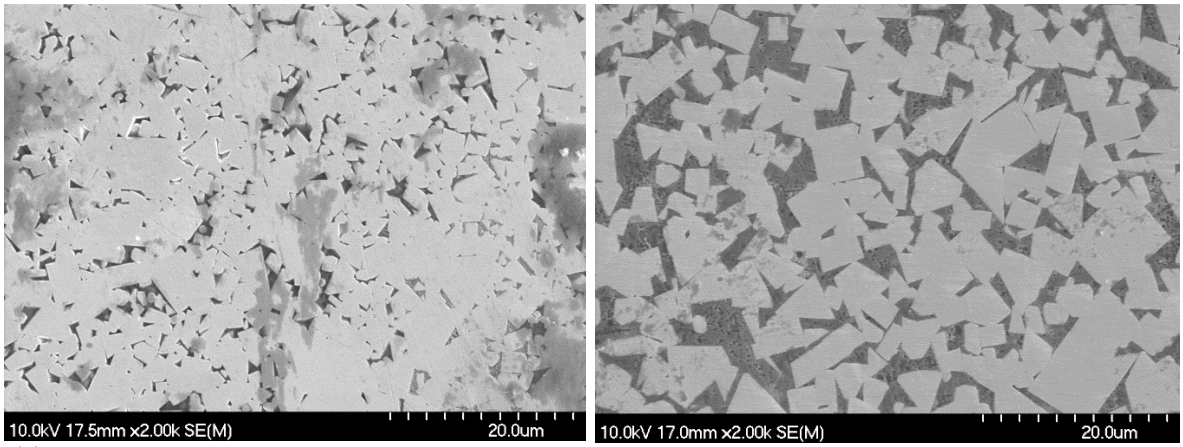

(a) (b)

Figure 29. SEM micrographs obtained from the polished surfaces of the as-received cermets: (a) WC-Co 10vol.% and (b) WC-Co 30 vol.%.

5.3.2. Electrochemical Analysis

5.3.2.1. Open Circuit Potential (OCP)

The results of OCP analysis, after a 2 hour stabilisation period for the WC-Co cermets are shown in Figure 30. The WC cermets with 10 and 30 vol.% Co *both* exhibited an essentially stable OCP, with only a slight decrease in potential immediately after exposure to the 3.5wt% NaCl containing aqueous electrolyte (Figure 30(a)). However, at 200 sec the potential increased, for the lower Co content material suggesting the start of formation of an oxide layer on the exposed surface (Figure 30b). WC prepared with 30 vol.% Co exhibited a more negative OCP value when compared to the composition with the lower Co content. Broadly speaking, materials with a higher OCP value tend to have better corrosion resistance in a specific environment. The more noble OCP observed for

the exposed surface with a lower amount of Co binder indicates the influence of the binder content on the oxidation characteristics of the overall material.

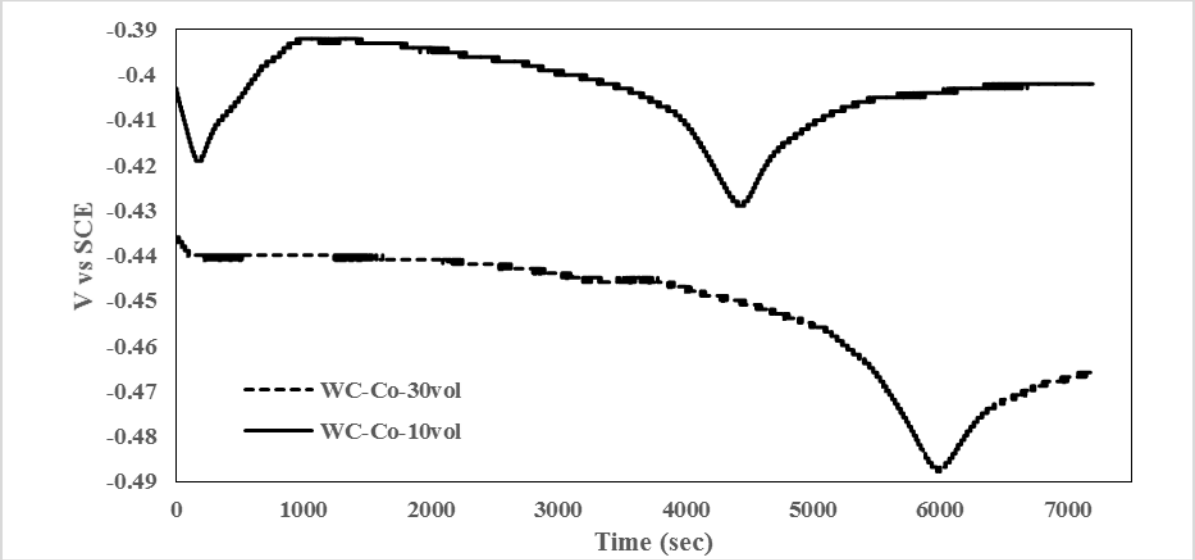

(a)

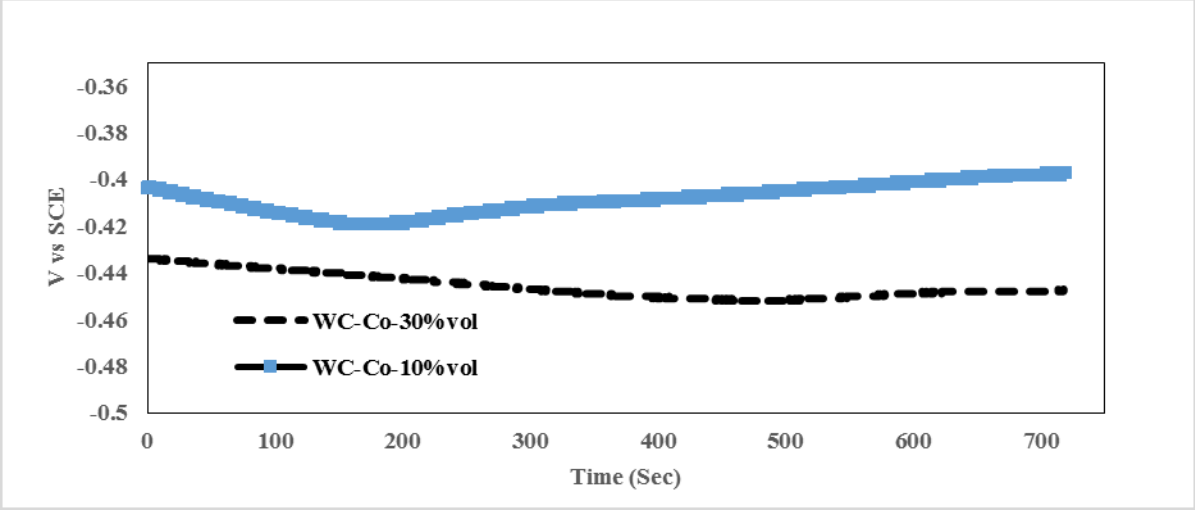

(b)

Figure 30. The evolution of OCP values for WC-Co, prepared with 10 and 30 vol.% binder content: (a) through 2 hours of immersion, and (b) immediately after immersion.

An effective difference in the corrosion potentials, relating to the individual ceramic and metallic phases, can introduce galvanic coupling at the interface of the two materials. The severity of the galvanic effect depends on the difference between the corrosion potentials,

and the polarization characteristics, of the two phases in contact. However the shift of OCP toward more a positive potential with a lower amount of Co binder shows that such galvanic behavior can be manipulated using a specific amount of binder, in order to reduce the coupling effect, while other properties such as hardness and wear resistance are not compromised.

5.3.2.2. Potentiodynamic Polarization

Potentiodynamic polarization measurements were performed on the WC–Co cermets, for both 10 and 30 vol.% binder, in fresh 3.5wt% NaCl aqueous solutions, with typical resultant curves shown in Figure 31. In a study related to characterization of the corrosion mechanism of single phase Co and WC, as well as a WC-Co composite, it has been found that the corrosion potential of WC is shifted towards more anodic potentials when compared to single phase Co, for the specific pH domain examined[11]. This implies a more noble WC surface acting as the cathode in the composite[11].

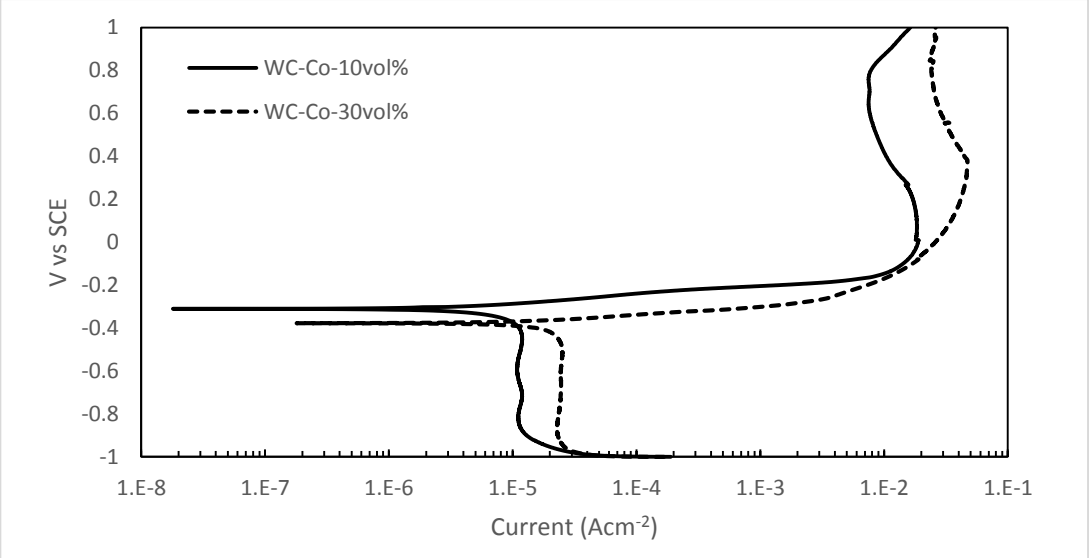

Figure 31. Potentiodynamic polarization curves for WC-Co with 10 and 30 vol.% Co binder.

After the potentiodynamic polarization evaluation the resultant curves were examined, and the average corrosion parameters were determined. These included the corrosion potential, E_{corr}, the current density at corrosion potential, $i_{corr,}$ the pitting potential, E_{pit}, and the current density at passivation, i_{pass}. Mean values were calculated from repeating the experiments for multiple samples to ensure reproducibility (Table 9 and Table 10). Previous potentiodynamic polarization/passivation curves obtained from WC–Co samples are very similar to those that were previously obtained for pure Co, but no passivation has been recorded for pure Co[11,12]. From examination of the potentiodynamic polarization curves obtained for the current WC-Co hardmetals, the poor corrosion resistance of the Co binder has been effectively eliminated within the cermet composition, resulting in clear passivation behavior for both the 10 and 30 vol.% binder content. However samples with 10 vol.% Co binder exhibited a lower passivation current when compared to those with 30 vol.% Co. It is believed that a stable passive film forms on the exposed surface of the WC-Co cermet composition, due to the presence of WO_x within the oxide layer that is formed during polarization[111]. Based on the potentiodynamic polarization curves obtained in the present work, and further information reported in previous studies, corrosion in WC-Co hard metals is directly related to dissolution of binder and its associated corrosion mechanism, while passivation is aided by the amount of W/WC dissolved in the binder phase.

Table 9. Average corrosion parameters for the WC-Co cermets with 10 vol.% Co binder.

Sample ID	OCP±2x10^{-3} (V vs. SCE)	E_{corr}±5x10^{-3} (V vs. SCE)	i_{corr}±2.3x10^{-6} (A/cm^2)	E_{pit}±5x10^{-3} (V vs. SCE)	i_{pass} (A/cm^2)	Rate of corrosion± 1.4x10^{-2} (mm/yr)	Rate of corrosion (active phase)± 1.5x10^{-3} (mm/yr)
Zm6-1	-0.398	-0.42	6.62E x 10^{-6}	-0.42	0.01	4.15 x 10^{-3}	4.27 x10^{-3}
Zm6-2	-0.4	-0.42	1.54 x 10^{-6}	-0.42	0.01	9.66 x 10^{-3}	9.93 x10^{-4}
Zm6-3	-0.403	-0.41	6.38 x 10^{-6}	-0.41	0.01	4.00 x 10^{-2}	4.11 x10^{-3}
Average	-0.400	-0.416	4.84 x 10^{-6}	-0.416	0.01	3.04 x 10^{-2}	3.13E x 10^{-3}

Table 10. Average corrosion parameters for the WC-Co cermets with 30 vol.% Co binder.

Sample ID	OCP±2.5x10^{-2} (V vs. SCE)	E_{corr}±2.2x10^{-3} (V vs. SCE)	i_{corr}±8.7x10^{-6} (A/cm^2)	E_{pit}±5x10^{-3} (V vs. SCE)	i_{pass} (A/cm^2)	Rate of corrosion± 6.6x10^{-2} (mm/yr)	Rate of corrosion (active phase)± 1.8x10^{-2} (mm/yr)
Zm18-1	-0.442	-0.439	1.1x10^{-5}	-0.439	0.1	8.3 x10^{-2}	2.3 x10^{-2}
Zm18-2	-0.466	-0.434	2.6 x10^{-5}	-0.434	0.1	2 x10^{-1}	5.5 x10^{-2}
Zm18-3	-0.463	-0.438	5.7 x10^{-6}	-0.438	0.1	4.3 x10^{-2}	1.19 x10^{-2}
Average	-0.445	-0.437	1.34 x10^{-5}	-0.437	0.1	1.1 x10^{-1}	3 x10^{-2}

In principle, the Co phase (the active metal during oxidation attack) comprises only approximately 10 and 30 area % of the composite surface, and consequently the current density used for calculation of the active corrosion rate should be multiplied accordingly by the factors 0.1 and 0.3, to adjust for this.

5.3.2.3. Cyclic Polarization

Typical cyclic polarization curves, obtained following the polarization evaluation of the two WC-Co cermets, were used to observe the tendency of the test samples toward pitting or localised corrosion (Figure 32). Pitting occurs when there is a localised breakdown in the passive film that normally protects the surface from accelerated corrosion attack. The shape and size of the hysteresis loop formed during a cyclic polarization scan is a suggestion of the susceptibility towards pitting corrosion. In materials that exhibit such

behavior, the size of the hysteresis loop is an indication of the degree of susceptibility. A larger loop, in a comparison of two materials subjected to the pitting analysis, indicates a higher risk of pitting occurring[38,60].

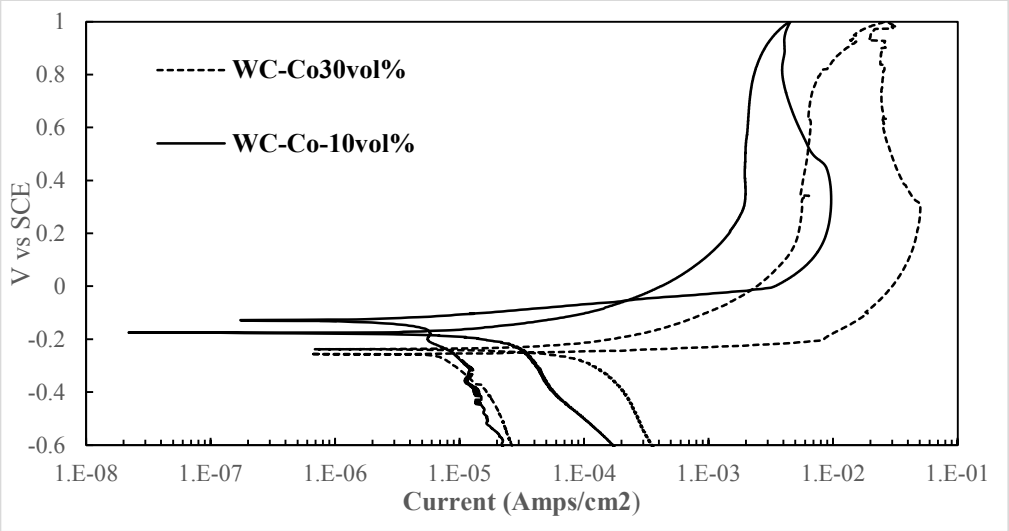

Figure 32. Cyclic polarization electrochemical analysis of WC-Co with 10 and 30 vol.% Co binder.

As shown in Figure 32, the WC-Co cermets exhibited a cyclic polarization curve with an anti-clockwise hysteresis loop, independent of the amount of binder in their composition. Studies on the cyclic polarization behavior of various materials have demonstrated that the anti-clockwise hysteresis loop relates to the formation of passivating oxide elements found at the exposed surface, which resist localised corrosion[118,119]. The results obtained by these studies also suggest that the dissolution of elemental species from the surface during polarization is not necessarily a result of the elemental composition of the specimen, but is primarily related to the density, thickness, and re-passivation potential of the oxide film. A dramatic increase in current density at E_{corr} shows that active localised oxidation takes place spontaneously at the corrosion potential for the media of 3.5% NaCl at a pH value of 6.1. The hysteresis loop closes *above* the corrosion potential, which is

otherwise known as repassivation potential, (E_{rp} = -0.048 V vs SCE) for specimens with 10 vol% Co binder, suggesting a lower tendency towards the formation of pits when compared to samples prepared with the higher amount of binder (E_{rp} = -0.251 V vs SCE). Furthermore, the larger hysteresis loop formed for the cermet composition with a higher amount of binder is an indication of the higher tendency toward pitting with increasing amounts of binder.

5.3.3. Post Corrosion Analysis

5.3.3.1. Microstructural Aanalysis

Figure 33 illustrates SEM images taken from the post potentiodynamic polarization surfaces of the WC-Co cermets with 10 and WC-C 30 vol% binder. The post corrosion surfaces demonstrate the formation of pits on the surface for both grades of cermet, regardless of the amount of binder in their composition. However the apparent severity of the attack increases with the binder content. The exposed surface of the cermet composition with 10 vol% Co binder shows a nominally uniform dissolution of the binder after polarization above the corrosion potential.

The post corrosion surface for this composition illustrates a skeleton of carbide grains, which is completely bonded to the binder phase. Conversely, with 30 vol% Co, initial pit generation was followed by formation of crevices at the ceramic/metallic interface, and resulted in destruction of the oxide layer on the post corrosion surface. Sufficient surface area between two materials with different corrosion potentials and electrochemical characteristics can introduce galvanic attack between the phases, and results in more severe corrosive attack in materials with higher metallic contents in their composition.

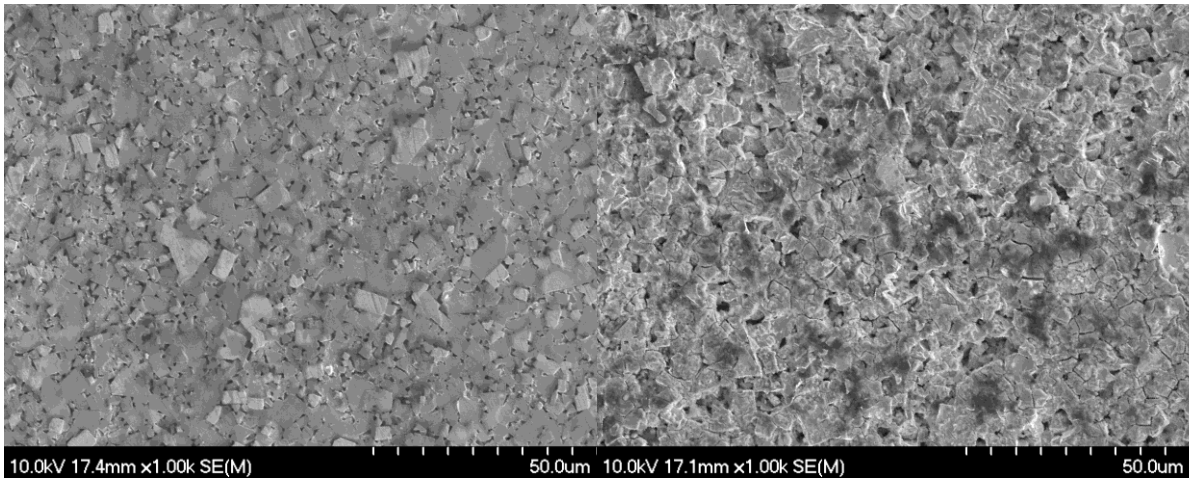

(a) (b)

Figure 33. SEM images obtained from post polarization testing surfaces of WC-Co, with (a) 10 vol% Co and (b) 30vol% Co binder.

The chemical analyses on the oxidised surfaces of both compositions have confirmed the formation of oxide layers. The cermet composition with a lower amount of binder maintained its initial nominal composition while the composition with higher amount of binder exhibited significant loss of the binder elemental species on the surface.

EDS analyses on the post polarization surfaces have shown that a higher amount of the metallic binder constituents is lost during corrosion attack from the surfaces of samples with a higher amount of binder, when evaluated under similar electrochemical testing periods/conditions (Figure 34). Loss of binder constituents ultimately results in loss of the carbide grains, either through further polarization or small mechanical forces such as the ones that exist in erosive environments[133].

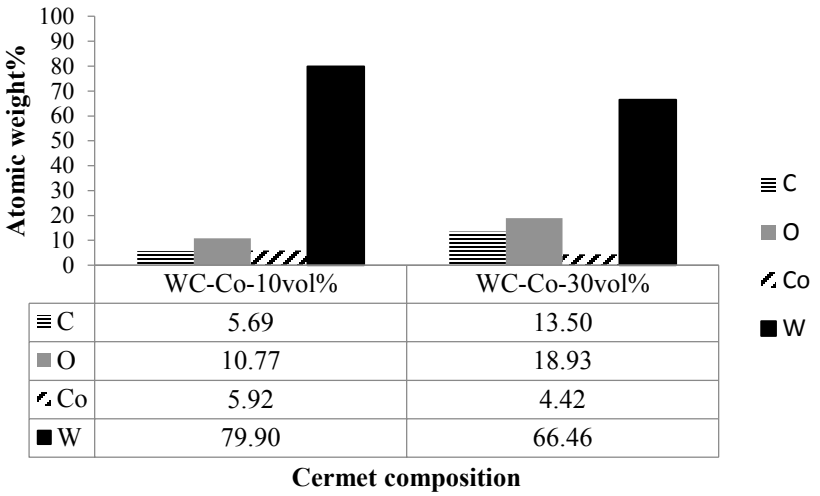

	WC-Co-10vol%	WC-Co-30vol%
C	5.69	13.50
O	10.77	18.93
Co	5.92	4.42
W	79.90	66.46

Figure 34. Post-corrosion EDS analysis of the WC-Co cermets.

5.3.3.2. Inductively Coupled Plasma/Optical Emission Spectroscopy (ICP-OES)

The results of ICP-OES analysis on the recovered, and filtered, post corrosion electrolyte for the WC-Co cermets are shown in Figure 35. Both the filtered solution and removed solids were analysed independently using this approach. Based on these results, it is apparent that the amount of Co binder initially in the WC-Co composition has a significant effect on the extent of material that was lost during potentiodynamic polarization of the surface. The results of impedance analyses on WC-Co cermet compositions, with media of various acidic and alkaline pH, have shown that Co binder acts as a non-polarisable electrode and is dissolving preferentially upon coupling, while the dissolution of the WC phase remains cathodically protected[11]. In terms of the filtered solids retrieved from post oxidation media, the amount of *both* Co and WC that was lost to the electrolyte during the corrosion experiments, under identical time and applied potential, was essentially doubled by increasing the volume of binder from 10 to 30%

(Figure 35(a)). However, it is observed that compositions with a lower amount of binder tend to contain a higher amount of dissolved Co within the solution in the form of ions (Figure 35(b)).

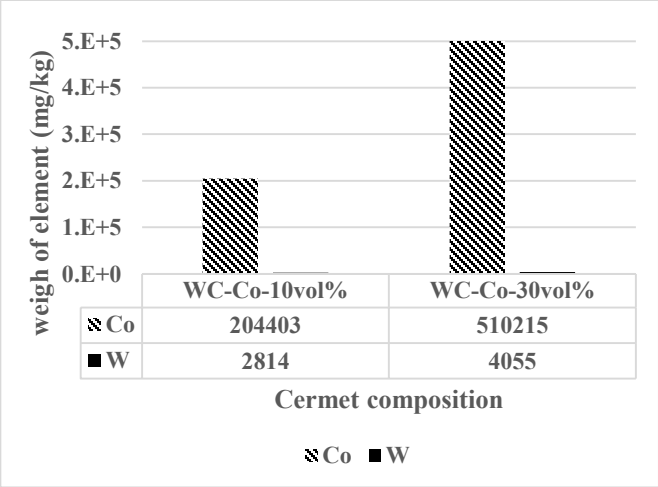

(a)

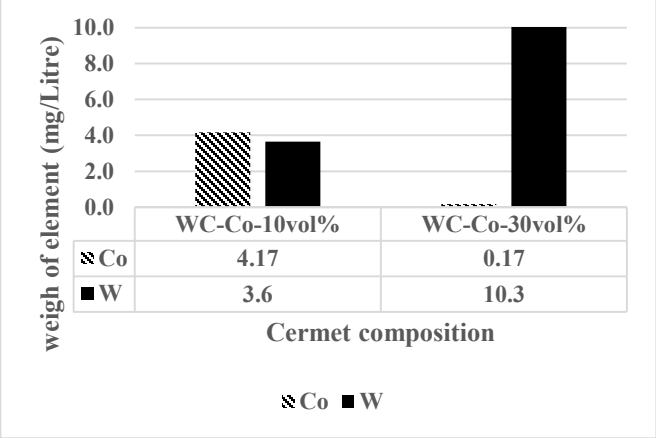

(b)

Figure 35. ICP-OES analysis on the recovered post-corrosion electrolyte for the WC-Co cermets: (a) filtered particulate residue and (b) filtered solution.

To further assess changes to the electrolyte during corrosion tests, the electrolyte pH was monitored before and after the polarization treatments. Post corrosion analysis of the electrolyte solutions shows an increase in pH value for both the 10 and 30 vol% Co

binder samples. The initial pH value (before potentiodynamic polarization) was found to be ~6.1 for both compositions. For the samples with 10vol% binder, the pH increased to ~6.6 after testing, while the post corrosion pH for samples with 30vol% binder increased significantly to ~9.5. The corrosion characteristics are directly related to the effect of specific ions on the exposed surface(s), which can be easily dominated by pH of the solution[12]. The corrosion process of WC–Co in neutral and acidic electrolyte mainly consists of Co dissolution from the surface, but in alkaline pH the degradation of WC becomes more significant[135]. The poor passivation ability of Co in acidic pH, and degradation of WC at alkaline pH, results in selective corrosion over the surface. Synergistic effects result from galvanic coupling between the metallic/ceramic phases, promoting the speed of the oxidation reaction for the metallic phase under constantly changing pH, while the carbide phase is catholically protected. According to the results of ICP-OES analysis, the amount of the carbide phase that has been lost to the electrolyte increases significantly when the volume fraction of the metallic binder Co is increased, in this instance corresponding to where the pH becomes increasingly more basic in character.

5.4. Conclusions

The mechanisms of corrosion occurring on the surface of bulk WC-Co cermets, in an aqueous solution containing 3.5% NaCl, were determined at room temperature (21±2°C). The effect of the volume of binder phase was closely studied using a series of electrochemical analyses.

Visual examination of the samples after corrosion tests has shown that, regardless of the amount of binder in composition, the attack on the surface initiates in the form of

localised ‘etching’ around the carbide/metal interfaces in discrete regions of the sample. Due to the excellent corrosion characteristics of the WC hard phase[136], the Co-based metallic phase has been assumed to be the rate determining phase in terms of calculations of the rate of the corrosion. The interface between the WC phase and the Co matrix provides a site for micro-galvanic and/or crevice corrosion. Accelerated dissolution of the binder phase at a pitting potential similar to pure Co was detected at lower potentials for both binder contents. However, the specimen with the higher volume of Co binder exhibited less noble values for E_{corr}, E_{pit} and E_{rp}, when compared to the composition with a lower amount of the active Co phase.

An increase in the pH value was also detected following the electrochemical analyses, for both of the WC-Co compositions tested. In acidic solutions, the cobalt binder dissolves preferentially but passivates at higher pH values. It has been found that an increase in the amount of metallic Co binder, results in an increase of the pH of the environment after polarization, due to the presence of higher amount of metallic phase in the electrolyte. In alkaline pH, degradation of WC is promoted and as a result, the rate of corrosion for the exposed surface was increased.

Chapter 6. Conclusions and Suggestions for Future Work

The physical and electrochemical properties of TiC- and Ti(C,N)-based cermets, manufactured through a simple reaction sintering process with Ni_3Al-based binders, were examined in the presented study. The corrosion behavior of the manufactured materials was assessed, in order to determine the ideal compositions of the bulk materials to be later used as a corrosion resistant thermal spray coating. Cermets were prepared with the ceramic phases of TiC, $TiC_{0.7}N_{0.3}$, $TiC_{0.5}N_{0.5}$ and $TiC_{0.3}N_{0.7}$, and were sintered at 1550°C for one hour with 30 vol% using a range of Ni_3Al-based intermetallic binders. Typically the cermets achieved densities in excess of 99% of theoretical. Single-phase TiC, Ti(C,N), and Ni_3Al materials have also been prepared using spark plasma sintering (SPS), to analyze the electrochemical characteristics of the parent components.

Measurement of the OCP, potentiodynamic, cyclic and potentiostatic polarization responses of the cermet and single-phase materials were generally determined, providing information regarding E_{corr} and i_{corr}, the rate of corrosion, and the tendency towards pitting. It was found that an increase of N content in the ceramic phase of the cermet changes the corrosion mechanism from localised pitting/galvanic corrosion for TiC ceramic phase to a uniform galvanic corrosion for the Ti(C,N) ceramic compositions. According to the calculated rates of corrosion, localised attack was more destructive toward the microstructure of the specimen. It was demonstrated that selective attack of the binder occurs, and both the extent of corrosion and the primary mechanism depends on the amount of nitrogen in the alloyed Ti(C,N) ceramic composition.

WC-Co ‘hardmetals’, which are widely used in a variety of industrial applications (some similar to those for TiC and TiCN based cermets), were also analysed for comparison purposes. In particular, this was undertaken to provide a more complete understanding of

the corrosion responses of these materials, and to provide a baseline for comparison of the respective corrosion mechanisms and rates. Accelerated dissolution of the Co-based binder phase, at pitting potential similar to pure Co, was detected for both types of WC-Co sample (with either 10 or 30 vol% Co binder). The composition with the higher volume content of Co binder exhibited less noble values for E_{corr}, E_{pit} and E_{rp}, compared to the composition with a reduced amount of the active phase (i.e. the Co-based binder).

Increases in the solution pH value were also detected following the electrochemical analysis for both WC-Co compositions, due to dissolution of the Co binder into the solution. In acidic solutions the Co-based binder dissolves preferentially, but it passivates at higher pH values. It has been found that an increase in the amount of metallic binder Co results in a more significant increase of the pH of the corrosion environment, due to the presence of a higher amount of the metallic phase in the electrolyte. In alkaline pH, degradation of WC is also promoted and, as a result, the rate of corrosion for the exposed surface was increased.

Following this study it was concluded that TiC and Ti(C,N) based cermets, prepared with Ni_3Al-based binders, exhibit corrosion rates as much as three orders of magnitude lower than WC-Co with nominally identical binder volume contents.

The current studies have provided a complete set of electrochemical examinations on a variety of Ti(C,N)-Ni_3Al cermet compositions, together with their single phase metallic and ceramic components. However, in order to fully understand the complex corrosion mechanisms of cermet materials with chemically altered compositions, such as those prepared with IC50 and IC221 metallic binders, a complete set of electrochemical analysis needs to be done on all of the single-phase parent metallic phases. Single-phase materials need to be manufactured with special attention paid to their final density and

surface quality. Similar test methods are suggested for the WC and Co ceramic/metallic phases, to achieve a clear conclusion of the oxidation mechanisms for this family of hard metals.

A detailed, real-time physical and chemical observation of the tested surfaces during electrochemical analysis, using a technique such as scanning electrochemical cell microscopy (SECM) is strongly suggested. This will provide continuous, real-time data generation relating to alterations taking place on the surface, at specific ranges of potentials and pH values, instead of analysing only the final surface and post corrosion products.

Furthermore, more extensive study and comparison of the post-test surfaces, paying attention to potential phase and compositional changes using XRD and XPS, would provide further information regarding the operative corrosion mechanisms.

References

1. Guilemany JM, Sanchiz I, Mellor BG, Llorca N, Miguel JR. Mechanical-property relationships of Co/WC and Co□Ni□Fe/WC hard metal alloys. *Int J Refract Met Hard Mater*. 1993;12(4):199-206. doi:10.1016/0263-4368(93)90049-L.

2. El Rayes MM, Abdo HS, Khalil KA. Erosion-Corrosion of Cermet Coating. *IntJElectrochemSci*. 2013;8:1117-1137.

3. Human AM, Roebuck B, Exner HE. Electrochemical polarisation and corrosion behaviour of cobalt and Co (W, C) alloys in 1 N sulphuric acid. *Mater Sci Eng A*. 1998;241(1):202-210.

4. Human A. Electrochemical behaviour of tungsten-carbide hardmetals. *Mater Sci Eng Struct Mater Prop Microstruct Process*. 1996;209(1–2):180. doi:10.1016/0921-5093(95)10137-3.

5. Wentzel Et erosion-corrosion resistance of tungsten-carbide hard metals. The erosion-corrosion resistance of tungsten-carbide hard metals. *Int J Refract hard Met*. 1997;15(1–3):81. doi:10.1016/S0263-4368(96)00016-9.

6. Hawthorne HM. Comparison of slurry and dry erosion behaviour of some HVOF thermal sprayed coatings. *Wear*. 1999;225:825. doi:10.1016/S0043-1648(99)00034-4.

7. De Souza VA, Neville A. Corrosion and erosion damage mechanisms during erosion–corrosion of WC–Co–Cr cermet coatings. *14th Int Conf Wear Mater*. 2003;255(1–6):146-156. doi:http://dx.doi.org/10.1016/S0043-1648(03)00210-2.

8. Souza VAD, Neville A. Aspects of microstructure on the synergy and overall material loss of thermal spray coatings in erosion–corrosion environments. *Wear*. 2007;263(1):339-346.

9. McMillan GK, Considine DM, Bristol EH, et al. *Process/industrial Instruments and Controls Handbook*. McGraw Hill; 1999.

10. Sutthiruangwong S, Mori G. Corrosion properties of Co-based cemented carbides in acidic solutions. *Int J Refract Met Hard Mater*. 2003;21(3):135-145.

11. Mueller Y, Latkoczy C, Virtanen S, Schmutz P, Hochstrasser(-Kurz) S. Analytical characterization of the corrosion mechanisms of WC–Co by electrochemical methods and inductively coupled plasma mass spectroscopy. *Corros Sci*. 2007;49(4):2002-2020. doi:http://dx.doi.org/10.1016/j.corsci.2006.08.022.

12. Tomlinson WJ, Ayerst NJ. Anodic polarization and corrosion of WC-Co hardmetals containing small amounts of Cr3C2 and/or VC. *J Mater Sci*. 1989;24(7):2348-2352. doi:10.1007/BF01174495.

13. Hochstrasser-Kurz S, Reiss D, Suter T, et al. ICP-MS, SKPFM, XPS, and Microcapillary Investigation of the Local Corrosion Mechanisms of WC–Co Hardmetal. *J Electrochem Soc*. 2008;155(8):C415. doi:10.1149/1.2929822.

14. Human AM, Exner HE, Human Exner, H.E., AM. The relationship between electrochemical behaviour and in-service corrosion of WC based cemented carbides. *RMHM Int J Refract Met Hard Mater*. 1997;15(1–3):65-71. doi:10.1016/S0263-4368(96)00014-5.

15. Potgieter JH, Thanjekwayo N, Olubambi P, Maledi N, Potgieter-Vermaak SS. Influence of Ru additions on the corrosion behaviour of WC–Co cemented carbide alloys in sulphuric acid. *Int J Refract Met Hard Mater*. 2011;29(4):478-487.

16. Kreymer GS. Strength of Hard Alloys,. 1974. http://oai.dtic.mil/oai/oai?verb=getRecord&metadataPrefix=html&identifier=ADA002635. Accessed December 1, 2014.

17. Becher PF, Plucknett KP. Properties of Ni3Al-bonded Titanium Carbide Ceramics. *J Eur Ceram Soc*. 1998;18(4):395-400. doi:10.1016/S0955-2219(97)00124-6.

18. Jones M, Horlock A., Shipway P., McCartney D., Wood J. A comparison of the abrasive wear behaviour of HVOF sprayed titanium carbide- and titanium boride-based cermet coatings. *Wear*. 2001;251(1-12):1009-1016. doi:10.1016/S0043-1648(01)00702-5.

19. Emamian A, Corbin SF, Khajepour A. Effect of laser cladding process parameters on clad quality and in-situ formed microstructure of Fe–TiC composite coatings. *Surf Coatings Technol*. 2010;205(7):2007-2015. doi:10.1016/j.surfcoat.2010.08.087.

20. Cho JEE, Hwang SYY, Kim KYY. Corrosion behavior of thermal sprayed WC cermet coatings having various metallic binders in strong acidic environment. *Surf coatings Technol*. 2006;200(8):2653-2662. doi:10.1016/j.surfcoat.2004.10.142.

21. Lekatou A, Zois D, Karantzalis AE, Grimanelis D. Electrochemical behaviour of cermet coatings with a bond coat on Al7075: Pseudopassivity, localized corrosion and galvanic effect considerations in a saline environment. *Corros Sci*. 2010;52(8):2616-2635. doi:10.1016/j.corsci.2010.04.010.

22. Wan W, Xiong J, Yang M, Guo Z, Dong G, Yi C. Effects of Cr3C2 addition on the corrosion behavior of Ti(C, N)-based cermets. *Int J Refract Met Hard Mater*. 2012;31:179-186. doi:10.1016/j.ijrmhm.2011.10.013.

23. Cheng FT, Lo KH, Man HC. NiTi cladding on stainless steel by TIG surfacing process Part II. Corrosion behavior. *Surf Coatings Technol*. 2003;172(2-3):316-321. doi:10.1016/S0257-8972(03)00346-3.

24. Zhang SC, Hilmas GE, Fahrenholtz WG. Zirconium Carbide–Tungsten Cermets Prepared by In Situ Reaction Sintering. *J Am Ceram Soc*. 2007;90(6):1930-1933. doi:10.1111/j.1551-2916.2007.01642.x.

25. Jones DA. *Principles and Prevention of Corrosion (2nd ed'96)*. 2nd ed. Upper Saddle River, NJ : Prentice Hall, ©1996.; 1996.

26. Liu Y, Feng Z, Walton J, Thompson GE, Skeldon P, Zhou X. Comparison of the behaviours of chromate and sol–gel coatings on aluminium. *Surf Interface Anal*. 2012.

27. Souza VADAD, Neville A. Corrosion and synergy in a WCCoCr HVOF thermal spray coating—understanding their role in erosion–corrosion degradation. *Wear*. 2005;259(1-6):171-180. doi:10.1016/j.wear.2004.12.003.

28. Malayoglu U, Neville A, Souza VAD. Assessing the Corrosion Characteristics of Metal/Ceramic Composites in Saline Environments-Aspects of the Interactions Between Phases. *Corros 2003*. 2003.

29. Berndt CC. *Thermal Spray 2001: New Surfaces for a New Millenium; Proceedings of the 2nd International Thermal Spray Conference, 28-30 May, 2001, Singapore*. 2nd ed. ASM International (OH); 2001. http://books.google.com/books?id=hz2m8wzXTT0C&pgis=1. Accessed November 10, 2014.

30. Ward LP, Hinton B, Gerrard D, Short K, others. Corrosion Behaviour of Modified HVOF Sprayed WC Based Cermet Coatings on Stainless Steel. *J Miner Mater Charact Eng*. 2011;10(11):989.

31. Liu Z, Cabrero J, Niang S, Al-Taha ZY. Improving corrosion and wear performance of HVOF-sprayed Inconel 625 and WC-Inconel 625 coatings by high power diode laser treatments. *Surf Coatings Technol*. 2007;201(16-17):7149-7158. doi:10.1016/j.surfcoat.2007.01.032.

32. Ettmayer P. Hardmetals and Cermets. *Annu Rev Mater Sci*. 1989;19(1):145-164. doi:10.1146/annurev.ms.19.080189.001045.

33. Kellner FJJJJ, Hildebrand H, Virtanen S. Effect of WC grain size on the corrosion behavior of WC-Co based hardmetals in alkaline solutions. *Int J Refract Met Hard Mater*. 2009;27(4):806-812. doi:10.1016/j.ijrmhm.2009.02.004.

34. Ahmad Z. Principles of Corrosion Engineering and Corrosion Control. In: *Principles of Corrosion Engineering and Corrosion Control*. Elsevier; 2006:576-608. doi:10.1016/B978-075065924-6/50012-X.

35. Fontana MG. *Corrosion Engineering*. 2nd ed. New York: Tata McGraw-Hill Education; 2005. http://books.google.ca/books/about/Corrosion_Engineering.html?id=YILALB8g3c0C&pgis=1. Accessed November 10, 2014.

36. Ehl RG, Ihde AJ. Faraday's electrochemical laws and the determination of equivalent weights. *J Chem Educ*. 1954;31(5):226-232. http://pubs.acs.org/doi/abs/10.1021/ed031p226.

37. ASTM, ASTM International. ASTM G102 - 89(2010) Standard Practice for Calculation of Corrosion Rates and Related Information from Electrochemical Measurements. In: *Annual Book of ASTM Standards*.Vol 89.; 2010:1-7. http://www.astm.org/Standards/G102.htm.

38. Frankel GS. Pitting Corrosion of Metals. *J Electrochem Soc*. 1998;145(6):2186. doi:10.1149/1.1838615.

39. Frankel GS, Sridhar N. Understanding localized corrosion. *Mater Today*. 2008;11(10):38-44. doi:10.1016/S1369-7021(08)70206-2.

40. Frankel GS. The growth of 2-D pits in thin film aluminum. *Corros Sci*. 1990;30(12):1203-1218. doi:10.1016/0010-938X(90)90199-F.

41. Kennell GF, Evitts RW, Heppner KL. A critical crevice solution and IR drop crevice corrosion model. *Corros Sci*. 2008;50(6):1716-1725. doi:10.1016/j.corsci.2008.02.020.

42. Park M. ASM Handbook Corrosion : Materials. 2005;13. http://www.asminternational.org/documents/10192/1849770/ACFAB43.pdf.

43. Celik E, Ozdemir I, Avci E, Tsunekawa Y. Corrosion behaviour of plasma sprayed coatings. *Surf Coatings Technol*. 2005;193(1-3):297-302. doi:10.1016/j.surfcoat.2004.08.143.

44. Inman IA, Datta PS. Studies of high temperature sliding wear of metallic dissimilar interfaces IV: Nimonic 80A versus Incoloy 800HT. *Tribol Int*. 2011;44(12):1902-1919. doi:10.1016/j.triboint.2011.08.004.

45. Durlu N. Titanium carbide based composites for high temperature applications. *J Eur Ceram Soc*. 1999;19(13–14):2415-2419. doi:10.1016/S0955-2219(99)00101-6.

46. Barik RCC, Wharton JAA, Wood RJKJK, Stokes KRR. Electro-mechanical interactions during erosion–corrosion. *Wear*. 2009;267(11):1900-1908. doi:10.1016/j.wear.2009.03.011.

47. Rajahram SSS, Harvey TJJ, Wood RJKJK. Erosion–corrosion resistance of engineering materials in various test conditions. *Wear*. 2009;267(1):244-254. doi:10.1016/j.wear.2009.01.052.

48. Wood RJKK. Erosion–corrosion interactions and their effect on marine and offshore materials. *Wear*. 2006;261(9):1012-1023. doi:10.1016/j.wear.2006.03.033.

49. Barik RC, Wharton JA, Wood RJK, Tan KS, Stokes KR. Erosion and erosion–corrosion performance of cast and thermally sprayed nickel–aluminium bronze. *Wear*. 2005;259(1-6):230-242. doi:10.1016/j.wear.2005.02.033.

50. HIROSHI SHIMOTAKE, JAMES C. HESSON. *Regenerative EMF Cells*. (Crouthamel CE, Recht HL, eds.). WASHINGTON, D.C.: AMERICAN CHEMICAL SOCIETY; 1967. doi:10.1021/ba-1967-0064.

51. *Corrosion and Corrosion Prevention of Low Density Metals and Alloys: Proceedings of the International Symposium*. The Electrochemical Society; 2001. http://books.google.com/books?id=GkqiJ1Ih8CcC&pgis=1. Accessed November 9, 2014.

52. *Handbook of Electrochemistry*. Elsevier; 2007. http://books.google.com/books?id=2g5GJtBFwo0C&pgis=1. Accessed November 9, 2014.

53. *Techniques for Corrosion Monitoring*. Elsevier; 2008. http://books.google.com/books?id=zLWjAgAAQBAJ&pgis=1. Accessed November 9, 2014.

54. Principles E, Polarization P. Application Note CORR-1 Subject : Basics of Corrosion Measurements. (865).

55. ASTM. ASTM G59 - 97(2009) Standard Test Method for Conducting Potentiodynamic Polarization Resistance Measurements. In: *Annual Book of ASTM Standards*.Vol 97.; 2005:1-4. http://www.astm.org/Standards/G59.htm.

56. Oberg KE, Friedman LM, Boorstein WM, Rapp RA. The diffusivity and solubility of oxygen in liquid copper and liquid silver from electrochemical measurements. *Metall Mater Trans B*. 1973;4(1):61-67. doi:10.1007/BF02649605.

57. Bard AJ, Faulkner LR. *Electrochemical Methods: Fundamentals and Applications*. New York: Wiley; 1980.

58. Skoog D. *Principles of Instrumental Analysis*. New York: Holt Rinehart and Winston; 1971.

59. Souza VAD, Neville A. Linking electrochemical corrosion behaviour and corrosion mechanisms of thermal spray cermet coatings (WC–CrNi and WC/CrC–CoCr). *Mater Sci Eng A*. 2003;352(1–2):202-211. doi:10.1016/S0921-5093(02)00888-2.

60. Measurements AP. Standard Test Method for Conducting Cyclic Potentiodynamic Polarization Measurements for Localized Corrosion Susceptibility of. 2014;86(Reapproved):1-5. doi:10.1520/G0061-86R14.2.

61. Watson SWW, Friedersdorf FJJ, Madsen BWW, Cramer SDD. Methods of measuring wear-corrosion synergism. *Wear*. 1995;181:476-484. doi:10.1016/0043-1648(95)90161-2.

62. Thompson NG, Syrett BC. Relationship between conventional pitting and protection potentials and a new, unique pitting potential. *Corrosion*. 1992;48(8):649-659. doi:10.5006/1.3315985.

63. So HS, Millard SG. On-Site Measurements on Corrosion Rate of Steel in Reinforced Concrete - ProQuest. *ACI Mater J*. 2007;104(6):638-642. http://search.proquest.com.ezproxy.library.dal.ca/docview/198087508/fulltextPDF/8B56A26C940B4772PQ/2?accountid=10406. Accessed November 9, 2014.

64. Stern M, Geary AL. Electrochemical Polarization: I . A Theoretical Analysis of the Shape of Polarization Curves. *J Electrochem Soc*. 1957;104(1):56-63. http://jes.ecsdl.org/content/104/1/56.abstract\nhttp://jes.ecsdl.org/content/104/1/56.full.pdf .

65. H. Tian, S. G. Corcoran, C. E. Reece and MJK. An Introduction to Electrochemical Impedance Measurement. *J Electrochem Soc*. 2008;155(9):D563-D568. http://www.korozja.pl/html/eis/technote06.pdf.

66. Kelly RG, Scully JR, Shoesmith DW, Buchheit RG. Electrochemical Techniques in Corrosion Science and Engineering. *World Wide Web Internet Web Inf Syst*. 2003;18:426. http://books.google.com/books?id=HQqXJuJXeVMC.

67. ASTM. ASTM G106 - 89(2010) Standard Practice for Verification of Algorithm and Equipment for Electrochemical Impedance Measurements. In: *Annual Book of ASTM Standards*.Vol 89.; 2010:1-11. http://www.astm.org/Standards/G106.htm.

68. Lasia A. Electrochemical impedance spectroscopy and its applications. In: *Modern Aspects of Electrochemistry*. Springer; 2002:143-248.

69. Novocontrol Spectrometers for Dielectric Spectroscopy, Impedance Spectroscopy, and Electrochemical Impedance Spectroscopy. http://www.novocontrol.de/. Accessed November 10, 2014.

70. Application Notes l Princeton Applied Research. http://www.princetonappliedresearch.com/Literature/index.aspx. Accessed November 10, 2014.

71. Espallargas N, Berget J, Guilemany JMM, Benedetti AV V, Suegama PHH. Cr< sub> 3</sub> C< sub> 2</sub>–NiCr and WC–Ni thermal spray coatings as alternatives to hard chromium for erosion–corrosion resistance. *Surf Coatings Technol*. 2008;202(8):1405-1417. doi:10.1016/j.surfcoat.2007.06.048.

72. Xu J, Zhuo C, Han D, Tao J, Liu L, Jiang S. Erosion–corrosion behavior of nano-particle-reinforced Ni matrix composite alloying layer by duplex surface treatment in aqueous slurry environment. *Corros Sci Corros Sci*. 2009;51(5):1055-1068. doi:10.1016/j.corsci.2009.02.029.

73. Stefánsson A, Gunnarsson I, Giroud N. New methods for the direct determination of dissolved inorganic, organic and total carbon in natural waters by Reagent-Free™ Ion Chromatography and inductively coupled plasma atomic emission spectrometry. *Anal Chim Acta*. 2007;582(1):69-74. doi:10.1016/j.aca.2006.09.001.

74. Chukwuma C Onuoha KP. The Effects of Grain Size on the Corrosion Behaviour of TiC-316L Stainless Steel Cermets in a Synthetic Seawater Solution. 2013:12-13.

75. Davis JR. *Corrosion: Understanding the Basics*.; 2000.

76. Sikka VK. No Title. *Corros 99*. 1999;1(1). https://www.onepetro.org/conference-paper/NACE-99266.

77. ASM International. *Special-Purpose Nickel Alloys*.; 2000. http://www.asminternational.org/documents/10192/1849770/ACFA9D7.pdf.

78. Chang R. Low-Temperature Elastic Properties of ZrC and TiC. *J Appl Phys*. 1966;37(10):3778. doi:10.1063/1.1707923.

79. Hornyak GL, Moore JJ, Tibbals HF, Dutta J. *Fundamentals of Nanotechnology*. CRC Press; 2011. https://books.google.com/books?id=mf7KBQAAQBAJ&pgis=1. Accessed January 7, 2015.

80. Kurlov AS, Gusev AI. *Tungsten Carbides: Structure, Properties and Application in Hardmetals*. Springer Science & Business Media; 2013. http://books.google.com/books?id=vcLBAAAAQBAJ&pgis=1. Accessed January 7, 2015.

81. Kleinhenz S, Pfennig V, Seppelt K. Preparation and Structures of [W(CH3)6], [Re(CH3)6], [Nb(CH3)6], and [Ta(CH3)6]. *CHEM Chem - A Eur J*. 1998;4(9):1687-1691. doi:10.1002/(SICI)1521-3765(19980904)4:9<1687::AID-CHEM1687>3.0.CO;2-R.

82. Modulus of Elasticity - Young Modulus for some common Materials. http://www.engineeringtoolbox.com/young-modulus-d_417.html. Accessed November 12, 2014.

83. Shackelford JF, Alexander W. *CRC Materials Science and Engineering Handbook*. Boca Raton, FL: CRC Press; 2001.

84. Lee B, Alsenz R, Ignatiev A, Van Hove M. Surface structures of the two allotropic phases of cobalt. *Phys Rev B*. 1978;17(4):1510-1520. doi:10.1103/PhysRevB.17.1510.

85. Watt S. *Cobalt*. Marshall Cavendish; 2006. https://books.google.com/books?id=m97yDP3Kw3gC&pgis=1. Accessed January 7, 2015.

86. *Cobalt, Issues 30-37*. Centre d'information du cobalt.; 1966. http://books.google.com/books?id=H8XVAAAAMAAJ&pgis=1. Accessed January 7, 2015.

87. Kaplan B, Norgren S, Schwind M, Selleby M. Thermodynamic calculations and experimental verification in the WC–Co–Cr cemented carbide system. *Int J Refract Met Hard Mater*. 2015;48:257-262. doi:10.1016/j.ijrmhm.2014.09.016.

88. ASTM. Standard Practice for Calculation of Corrosion Rates and Related Information. *ASTM G 102*. 1999;89(Reapproved).

89. Mendelson MI. Average Grain Size in Polycrystalline Ceramics. *J Am Ceram Soc*. 1969;52(8):443-446. http://doi.wiley.com/10.1111/j.1151-2916.1969.tb11975.x.

90. Stewart T. The Characterization of TiC and Ti(C,N) Based Cermets with and without Mo2C. 2014;(February). http://hdl.handle.net/10222/45246.

91. Qi F, Kang S. A study on microstructural changes in Ti (CN)–NbC–Ni cermets. *Mater Sci Eng A*. 1998;251(December 1997):276-285. doi:10.1016/S0921-5093(98)00609-1.

92. Stewart TL, Plucknett KP. The sliding wear of TiC and Ti(C,N) cermets prepared with a stoichiometric Ni3Al binder. *Wear*. 2014;318(1-2):153-167. doi:10.1016/j.wear.2014.06.025.

93. Cao G, Geng L, Zheng Z, Naka M. The oxidation of nanocrystalline Ni3Al fabricated by mechanical alloying and spark plasma sintering. *Intermetallics*. 2007;15(12):1672-1677. doi:10.1016/j.intermet.2007.07.003.

94. Chen G, Lou H. The effect nanocrystallization on the oxide formation on Ni-11Cr-8Al alloy. *Scr Mater*. 2000;43(2):119-122. doi:10.1016/S1359-6462(00)00379-1.

95. Zhou Y, Peng X, Wang F. Oxidation of a novel electrodeposited Ni–Al nanocomposite film at 1050 °C. *Scr Mater*. 2004;50(12):1429-1433. doi:10.1016/j.scriptamat.2004.03.014.

96. Zhang S. Titanium carbonitride-based cermets: processes and properties. *Mater Sci Eng A*. 1993;163(1):141-148.

97. Bozzini B, Pietro De Gaudenzi G, Fanigliulo A, Mele C. Electrochemical oxidation of WC in acidic sulphate solution. *Corros Sci*. 2004;46(2):453-469. doi:10.1016/S0010-938X(03)00146-X.

98. Bozzini B, Busson B, De Gaudenzi G Pietro, D'Urzo L, Mele C, Tadjeddine A. An SFG and ERS investigation of the corrosion of CoW0.013C0.001 alloys and WC–Co cermets in CN−-containing aqueous solutions. *Corros Sci*. 2007;49(5):2392-2405. doi:10.1016/j.corsci.2006.10.038.

99. Konadu DS, Merwe J van der, Potgieter JH, Potgieter-Vermaak S, Machio CN. The corrosion behaviour of WC-VC-Co hardmetals in acidic media. *Corros Sci*. 2010;52(9):3118-3125. doi:10.1016/j.corsci.2010.05.033.

100. Tomlinson WJ, Linzell CR. Anodic polarization and corrosion of cemented carbides with cobalt and nickel binders. *J Mater Sci*. 1988;23(3):914-918. doi:10.1007/BF01153988.

101. Human AM, Northrop IT, Luyckx SB, James MN. A Comparison Between Cemented Carbides Containing Cobalt- and Nickel-Based Binders. *J Hard Mater*. 1991;2(3):245-256.

102. Bolelli G, Giovanardi R, Lusvarghi L, Manfredini T. Corrosion resistance of HVOF-sprayed coatings for hard chrome replacement. *Corros Sci*. 2006;48(11):3375-3397.

103. Lekatou A, Regoutas E, Karantzalis AE. Corrosion behaviour of cermet-based coatings with a bond coat in 0.5 MH 2 SO 4. *Corros Sci*. 2008;50(12):3389-3400.

104. Buchholz S. RECIPROCATING WEAR RESPONSE OF Ti(C,N)-Ni3Al CERMETS. 2011. http://dalspace.library.dal.ca//handle/10222/14409. Accessed January 13, 2015.

105. Marquardt DW. An algorithm for least-squares estimation of nonlinear parameters. *J Soc Ind Appl Math*. 1963;11(2):431-441.

106. Blasco-Tamarit E, Igual-Muñoz A, Antón JG, García-García D. Comparison between open circuit and imposed potential measurements to evaluate the effect of temperature on galvanic corrosion of the pair alloy 31–welded alloy 31 in LiBr solutions. *Corros Sci*. 2008;50(12):3590-3598. doi:10.1016/j.corsci.2008.09.011.

107. Lavrenko V, Shvets V, Talash V. Electrolytic Corrosion of Titanium Carbonitride Composites. *Powder Metall Met Ceram*. 2004;43(1-2):62-66. doi:10.1023/B:PMMC.0000028273.86448.54.

108. Noh JS, Laycock NJ, Gao W, Wells DB. Effects of nitric acid passivation on the pitting resistance of 316 stainless steel. *Corros Sci*. 2000;42(12):2069-2084. doi:10.1016/S0010-938X(00)00052-4.

109. Songür M, Çelikkan H, Gökmeşe F, Şimşek SA, Altun NŞ, Aksu ML. Electrochemical corrosion properties of metal alloys used in orthopaedic implants. *J Appl Electrochem*. 2009;39(8):1259-1265. doi:10.1007/s10800-009-9793-6.

110. Hihara LH, Latanision RM. Galvanic Corrosion of Aluminum-Matrix Composites. *Corrosion*. 1992;48(7):546-552. doi:10.5006/1.3315972.

111. Pourbaix M. *Atlas of Electrochemical Equilibria in Aqueous Solutions*. National Association of Corrosion Engineers; 1974. http://books.google.ca/books/about/Atlas_of_electrochemical_equilibria_in_a.html?id=QjxRAAAAMAAJ&pgis=1. Accessed January 5, 2015.

112. Basame SB, White HS. Pitting Corrosion of Titanium The Relationship Between Pitting Potential and Competitive Anion Adsorption at the Oxide Film/Electrolyte Interface. *J Electrochem Soc*. 2000;147(4):1376. doi:10.1149/1.1393364.

113. Stern M, Union Carbide Corp. N.Y. NF. SURFACE AREA RELATIONSHIPS IN POLARIZATION AND CORROSION. 1958.

114. Toma D, Brandl W, Marginean G. Wear and corrosion behaviour of thermally sprayed cermet coatings. *Surf Coatings Technol*. 2001;138(2):149-158.

115. Rendón-Belmonte M, Pérez-Quiroz JT, Terán-Guillén J, Porcayo-Calderón J, Torres-Acosta A, Orozco-Gamboa G. Evaluation of a Cr3C2 (NiCr) Coating Deposited on s4400 by Means of an HVOF Process and Used for Flow Plates of PEM Fuel. *Int J Electrochem Sci*. 2012;7:1079-1092.

116. Stewart TL, Plucknett KP. The effects of Mo 2 C additions on the microstructure and sliding wear of TiC 0.3 N 0.7–Ni 3 Al cermets. *Int J Refract Met Hard Mater*. 2015;50:227-239.

117. ASTM F2129-08, Standard Test Method for Conducting Cyclic Potentiodynamic Polarization Measurements to Determine the Corrosion Susceptibility of Small Implant Devices. In: *ASTM International*. West Conshohocken, PA; 2008. doi:10.1520/F2129-08.

118. Zhou YL, Niinomi M, Akahori T, Fukui H, Toda H. Corrosion resistance and biocompatibility of Ti–Ta alloys for biomedical applications. *Mater Sci Eng A*. 2005;398(1-2):28-36. doi:10.1016/j.msea.2005.03.032.

119. Khan MA, Williams RL, Williams DF. The corrosion behaviour of Ti–6Al–4V, Ti–6Al–7Nb and Ti–13Nb–13Zr in protein solutions. *Biomaterials*. 1999;20(7):631-637. doi:10.1016/S0142-9612(98)00217-8.

120. Lavrenko VA, Panasyuk AD, Desmaison-Brut M, Shvets VA, Desmaison J. Kinetics and mechanism of electrolytic corrosion of titanium-based ceramics in 3% NaCl solution. *J Eur Ceram Soc*. 2005;25(10):1813-1818. doi:10.1016/j.jeurceramsoc.2004.12.014.

121. Toth L. *Transition Metal Carbides and Nitrides*. Elsevier; 2014.

122. Karlsson L, Hultman L, Johansson MP, Sundgren J-E, Ljungcrantz H. Growth, microstructure, and mechanical properties of arc evaporated TiCxN1−x (0≤x≤1) films. *Surf Coatings Technol*. 2000;126(1):1-14. doi:10.1016/S0257-8972(00)00518-1.

123. Yang Y, Zhang D, Yan W, Zheng Y. Microstructure and wear properties of TiCN/Ti coatings on titanium alloy by laser cladding. *Opt Lasers Eng*. 2010;48(1):119-124. doi:10.1016/j.optlaseng.2009.08.003.

124. Brillo J, Kuhlenbeck H, Freund H-J. Interaction of O< sub> 2</sub> with WC (0001). *Surf Sci*. 1998;409(2):199-206.

125. Nishizawa T, Ishida K. The Co (Cobalt) system. *Bull Alloy Phase Diagrams*. 1983;4(4):387-390. doi:10.1007/BF02868089.

126. Wu X, Tao N, Hong Y, et al. Strain-induced grain refinement of cobalt during surface mechanical attrition treatment. *Acta Mater*. 2005;53(3):681-691. doi:10.1016/j.actamat.2004.10.021.

127. Betteridge W. The properties of metallic cobalt. *Prog Mater Sci*. 1980;24:51-142. doi:10.1016/0079-6425(79)90004-5.

128. Scholl H, Hofman B, Rauscher A. Anodic polarization of cemented carbides of the type [(WC,M): M = Fe, Ni or Co] in sulphuric acid solution. *Electrochim Acta*. 1992;37(3):447-452. doi:10.1016/0013-4686(92)87034-W.

129. Williams CC, Hough WP, Rishton SA. Scanning capacitance microscopy on a 25 nm scale. *Appl Phys Lett*. 1989;55(2):203. doi:10.1063/1.102096.

130. Yasutake M, Aoki D, Fujihira M. Surface potential measurements using the Kelvin probe force microscope. *Thin Solid Films*. 1996;273(1-2):279-283. doi:10.1016/0040-6090(95)06772-8.

131. Stratmann M, Streckel H. The Investigation of the Corrosion of Metal Surfaces, Covered with Thin Electrolyte Layers–A New Experimental Technique. *Berichte der Bunsengesellschaft für Phys Chemie*. 1988;92(11):1244-1250.

132. Hansen W. Electrode resistance and the emersed double layer. *Surf Sci*. 1980. http://www.sciencedirect.com.ezproxy.library.dal.ca/science/article/pii/0039602880906020. Accessed November 28, 2014.

133. Shipway PH, Howell L. Microscale abrasion–corrosion behaviour of WC–Co hardmetals and HVOF sprayed coatings. *Second Int Conf Erosive Abras Wear*. 2005;258(1–4):303-312. doi:10.1016/j.wear.2004.04.003.

134. Stack MM, Abd El-Badia TM. Some comments on mapping the combined effects of slurry concentration, impact velocity and electrochemical potential on the erosion–corrosion of WC/Co–Cr coatings. *Wear*. 2008;264(9-10):826-837. doi:10.1016/j.wear.2007.02.025.

135. Tomlinson WJ, Molyneux ID. Corrosion, erosion-corrosion, and the flexural strength of WC-Co hardmetals. *J Mater Sci J Mater Sci*. 1991;26(6):1605-1608.

136. Voorhies JD. Electrochemical and Chemical Corrosion of Tungsten Carbide (WC). *J Electrochem Soc*. 1972;119(2):219. doi:10.1149/1.2404164.